SmartMat

WILEY

SmartMat Open Access

REVIEW OPEN ACCESS

MXenes for Various Applications: Recent Trends and Future Aspects

Iftikhar Hussain[1] | Riffat Amna[2] | B. Kalidasan[3] | Gokana Mohana Rani[4] | Hari Bandi[5] | Sada Venkateswarlu[6] | Shahid Ali Khan[1] | Debananda Mohapatra[7] | Kaili Zhang[1]

[1]Department of Mechanical Engineering, City University of Hong Kong, Hong Kong, China | [2]Department of Civil and Environmental Engineering, Khalifa University of Science and Technology, Abu Dhabi, United Arab Emirates | [3]Research Centre for Nanomaterials and Energy Technology (RCNMET), Faculty of Engineering and Technology, Sunway University, Darul Ehsan, Selangor, Malaysia | [4]Department of Biological Sciences and Bioengineering, NanoBio High-Tech Materials Research Center, Inha University, Incheon, Republic of Korea | [5]Department of Electronics and Information Convergence Engineering, Institute for Wearable Convergence Electronics, Kyung Hee University, Yongin, Republic of Korea | [6]Nanotechnology Centre, Centre for Energy and Environmental Technologies (CEET), VSB–Technical University of Ostrava, Ostrava-Poruba, Czech Republic | [7]Graduate School of Semiconductor Materials and Devices Engineering, Ulsan National Institute of Science and Technology (UNIST), Ulsan, Republic of Korea

Correspondence: Iftikhar Hussain (ihussaintoori1@gmail.com) | Shahid Ali Khan (alikhan@cityu.edu.hk) | Debananda Mohapatra (debanandam@unist.ac.kr) | Kaili Zhang (kaizhang@cityu.edu.hk)

Received: 11 November 2024 | **Revised:** 11 February 2025 | **Accepted:** 14 February 2025

Funding: This work was supported by the Hong Kong Innovation and Technology Commission (GHP/247/22GD).

Keywords: electrochemical sensing | energy harvesting | environmental remediation | MXene: phase change materials | removal of heavy metal ions | solar thermal desalination

ABSTRACT

Two-dimensional (2D) MXene structure, versatile surface reactivity, flexibility, wearability, and outstanding thermal attributes make them highly suitable for numerous applications. This comprehensive review based on MXenes delves into the potential uses of fewer assessed applications, such as materials, solar thermal desalination, energy harvesting, electrochemical sensing, environmental remediation, and removal of heavy metal ions. Several industries associated with the summarized applications include hybrid photovoltaic thermal systems, energy storage, energy conversion, soft electronics, and other industries. Further, the review underscores the importance and future guidance of continued research in the MXene field to harness the potential benefits of not only summarized applications but also diverse applications.

1 | Introduction

Graphene discovery in 2004 stimulated a wide range of discoveries of other two-dimensional (2D) nanomaterials in materials science, materials engineering, and technology [1, 2]. For instance, these 2D nanomaterials possess unique characteristics such as atomically thin materials with high aspect ratio, significant active surface area, and adjustable optoelectronic properties [2, 3]. Among all studied 2D transition metal oxides/hydroxides/sulfides/phosphides, transition metal dichalcogenides, layered double hydroxides (LDHs), metal-organic frameworks (MOFs), covalent organic frameworks (COFs), black phosphorus, hexagonal boron nitrides (h-BNs), and so forth, 2D carbides/nitrides/carbonitrides, that is, MXene draws tremendous attentions from both academia and industry since its discovery 2011 [4, 5]. They are now the largest, diverse family of 2D nanomaterials going through rapid expansions from extensive compositional to structural diversity [6–8]. The versatile class of 2D MXene materials delivered notable applications in energy conversion, storage, sensing, catalysis, and electromagnetic shielding quickly over the years to demonstrate its potentiality [9–11]. It is primarily due to their unusual coupling of metal-like conductivity, hydrophilicity, optoelectronic, and tuneable electrochemical properties with ease of processability.

The 2D metallic character of MXene nanomaterials distinguishes them from other known 2D nanomaterials, hence their targeted applications.

MXene wet chemical processability brings inherent 2D material challenges like self-aggregation stacking problems along with their thermal and oxidative phase stability issues. MXenes are generally derived from their parent MAX phases, which are reasonably stable ceramic materials [9–11]. However, in a particular case, the thermal and chemical stability of Ti-MXenes exhibits a lower level of stability when exposed to higher oxidative environments, resulting in a transformation into TiO_2 oxide. An illustration of this phenomenon can be seen through annealing at a temperature of 1150°C in an air environment for 30 s, leading to its conversion into TiO_2 oxide along with carbon sheets [12]. Simultaneously, the electronic characteristics of Ti-MXene display a significant reliance on the specific methodology employed during the synthesis process, highlighting the crucial roles played by surface termination groups and interlayer engineering components in determining its properties. Thus, understanding and manipulating these factors are essential in tailoring the properties and performance of MXenes for various applications. At the same time, considering the mechanical stability and high flexibility, the Ti-MXene monolayer's Young's modulus was reported to be in the range of 330 GPa as that of a graphene monolayer, which is around 1 TPa that significantly promises to be mechanically flexible [13, 14]. For instance, graphene resists atomic movement under external pressure or stimuli due to its inner atomic structure and structural rigidity. In contrast, MXene has comparatively wide interlayer spacing and accordion-like open internal microstructure with hydrophilicity. Particularly for CNTs and graphene, the exceptionally high compressive modules, ≈1 TPa, strongly resist the associated atomic movements under applied external pressure. Also, the high thermal conductivity and low thermal hysteresis of MXene embrace the significant promise of MXene as a phase change material (PCM) [15, 16].

One promising solution to effectively store the substantial amount of heat generated by solar radiation is the appropriate management of PCM. Nevertheless, only a limited number of these materials exhibit the capability to efficiently convert solar energy into heat due to a lack of shape stability and energy conversion ability. Developing high-performance shape-stabilized PCMs suitable for solar thermal energy storage (TES) and environmental remediation perspectives is crucial. Xu et al. [17] demonstrated MXene-containing diatomite as a supporting material and polyethylene glycol as the novel shape-stabilized PCMs, where MXene acts as an enhancer of the thermal conductivity approximately by 111%. In another work, Akhiani et al. [18] established a careful examination of the properties of the melamine sponge (MS) to create a unified structure incorporating MXene and reduced graphene oxide (rGO) components. The efficiency of photothermal storage achieved an impressive 93.0%, demonstrating remarkable capabilities when the MXene content was optimized to approximately 1%, thus highlighting the promising outlook for achieving superior energy conversion efficiency within the MXene/rGO composites [18]. Some of the PCMs exhibit the capability to transform solar energy into heat effectively; moreover, it is essential to encase PCMs within porous substrates to improve their resistance to leaking and performance in converting light to heat [19]. MXene/polyethylene glycol composite exhibits strong solar light absorption, efficiently converting solar energy into heat, with a photo-thermal storage efficiency of 93% [19].

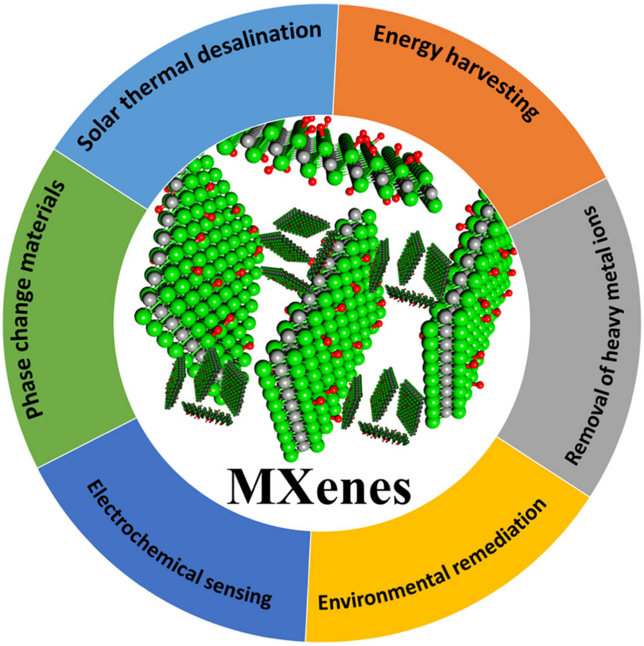

SCHEME 1 | Overview of the MXene for various applications.

Several review articles have been dedicated to the MXene systems, synthesis processes, and energy storage such as batteries and supercapacitors applications [9, 20–25]. Moreover, recently, there has been a growing interest in applying MXenes in various other applications such as PCMs, electromagnetic shielding to solar desalination and environmental remediations. MXene can be a very promising light-to-heat conversion material and thus deserves more research attention toward practical applications. The ever-increasing enthusiasm surrounding MXenes has generated a demand for specialized details providing in-depth instructions for the investigation of MXenes. This study covers a timely review of PCMs, solar thermal desalination, energy harvesting, electrochemical sensing, environmental remediation, and removal of heavy metal ions as summarized in Scheme 1.

2 | Applications

2.1 | MXene for PCMs

PCMs are functional materials that store and release thermal energy via phase transition [26]. It possesses a tremendous latent heat absorption capability during phase shift and stable temperature conversion, making it a valuable resource for energy management. Over the past decades, PCMs have been actively used in battery thermal management [27], building heating and cooling [28], solar thermal systems [29], waste heat recovery [30], and off-peak energy storage systems. Depending on phase transition, PCMs are categorized as solid-to-solid, solid-to-liquid, solid-to-gas, and liquid-to-gas vice versa. PCMs, with high energy density, are preferred for thermal regulation applications as they can store and discharge a significant amount of energy. Nevertheless, low thermal conductivity, poor optical absorbance of electromagnetic rays, volumetric changes, and the possibility of leakage during phase transfer of PCMs limit their full potential usage in thermal regulation units as it slows down the charging and discharging rate [31]. Since no individual material can facilitate all the essential qualities for an ideal thermal storage media, one must employ the materials that are available and attempt to compensate for the inadequate physical attributes through a suitable system design. Due to graphene's narrow band gap and poor current on/off ratio, despite being the most widely used 2D material, many researchers have concentrated their efforts on a variety of 2D layered materials, including h-BN, metal oxides, metal halides, MXene [32], nano clay, polymer nanosheets, and metal organic-framework [33]. Because of its remarkable properties, the cutting-edge 2D material MXene has become widely used in TES applications. It makes it possible to store waste heat for later use, convert solar energy into electrical or thermal energy, and efficiently capture thermal energy. Notable developments have also been made in advanced energy storage materials, such as high-performance composite PCM.

As far as performance enhancement of PCM is concerned, MXenes offer a range of beneficial features in their core aspects, covering structural, optical, electrical, and sometimes strong TES properties [34]. MXenes are distinguished by their greater surface area, the presence of hydrophilic functional groups, their high atomic numbers, and their diamagnetic behaviors [35]. The functional groups of MXenes on the surface play a key role in enhancing its rigidity and flexibility, which is particularly important in producing thinner films as part of bioelectronic systems. Specifically, the hydrophilic functional groups, larger specific surface area, and the ability to easily absorb light make MXenes well-suited for dispersion with PCM for solar TES systems [36]. Nevertheless, the nonuniform size and arrangement of MXene nanosheets post-etching could create obstacles in the formation of an effective heat conduction network on being used as a nanomaterial with PCM. To effectively address the issues mentioned above, Ma et al. [37] conducted a research investigation that involved integrating silver (Ag) nanowires and MXenes into the design of PCM (PEG). The outstanding structure and remarkable thermal conductivity of Ag nanowires and MXenes make it possible to establish a three-dimensional thermal conductivity network. To prevent MXene nanosheets from stacking in composite PCM and to improve heat conductivity, Ag nanowires act as a bridge between the individual nanosheets.

Subsequently, MXene, being comprised of transition metal components and exhibiting a larger surface area to volume ratio facilitates the enhancement of the heat transfer of MXene-dispersed composite. Henceforth, with the interest to explore the potential of MXene as a thermal conductivity enhancer, numerous research works have been conducted. For instance, Gowthami et al. [38] synthesized MXene from the Ti_3AlC_2 (MAX Phase) precursor at the size of 218 nm via a chemical etching process to disperse with binary eutectic of polyethylene glycol mixture (PEG 6000:PEG 10,000 at 15:85). MXene was dispersed at a concentration ranging between 0.2% and 1.0%, to explore the thermal heat transfer rate, optical absorbance as well as stability of the composite PCM at long term operation (repeated phase transition cycles).

In general, most research explores PCM's charging and discharging rate via its thermal conductivity. In contrast, in this research work, the charging and discharging were presented in terms of time (minutes). Results ensured the charging of composite PCM with 1% concentration of MXene to occur in 17 min, whereas the charging of composite PCM with 0.2% concentration was 21 min. Furthermore, it is observed that the dispersion of MXene with organic binary eutectic PCM reflected in a minor drop in melting enthalpy of the composite PCM. MXenes, in addition to being intrinsically hydrophilic, showcase remarkable thermal and electrical conductivity and exhibit greater resistance to oxidation, thermal, and chemical shocks when compared to graphene [36]. The thermal performance of paraffin was experimentally investigated by Aslfattahi et al. [39], focusing on thermal conductivity, specific heat capacity, and thermal stability. The study involved dispersing 0.1%, 0.2%, and 0.3% concentrations of laboratory-synthesized MXene. The results indicated a 16% increase in the thermal conductivity of paraffin, rising from 0.197 to 0.228 W/m·K at the 0.3% MXene concentration. This enhancement was attributed to the high surface area-to-volume ratio of MXene compared to paraffin wax.

Additionally, the specific heat capacity of paraffin rose from 2.1 to 2.8 J/(g K) at a temperature of 25°C. This phenomenon might result from the high surface energy atoms of organic paraffin (C─H bonds) creating interface interactions between atoms on the surface area of 2D materials. Though the developed composite PCM exhibits a slight increase in thermal conductivity, the improvement is not convincing; however, the optical absorbance of the developed composite is significant. Similarly, Khan et al. [40] conducted an experimental study to assess the thermal performance of a hybrid nanomaterial consisting of titania and MXene dispersed in paraffin with a melting temperature of 82°C. The hybrid nanomaterial was comprised of equal amounts of Titania and MXene, with concentrations of 0.1%, 0.2%, and 0.3% dispersed in PCM. The PCM composites synthesized exhibited a high latent heat capacity of 182.6 J/g and improved thermal conductivity of 0.355 W/m·K compared to traditional PCMs. This new material shows potential for efficient TES in sustainable technologies such as solar energy systems, with enhanced heat transfer capabilities.

MXene, a 2D nano-flakes material characterized by its metal-like conductivity, excellent water solubility, and impressive photo-thermal conversion efficiency, is finding growing applications in the areas of TES [41] and electromagnetic interference (EMI) shielding [42]. Furthermore, environmental electromagnetic radiation can be harmful to people's health as well as the effective functioning of electronic equipment. Composite materials with high TES and EMI shielding effectiveness (SE) qualities must be combined to preserve human health safety and the accuracy and dependability of equipment. Researchers have investigated the role of MXene with PCM in addressing the challenges of thermal management and EMI. For example, Yue et al. [43] have developed a form-stable composite PCM (n-octadecane) by incorporating delignified wood (DW) and MXene at various concentrations (0, 2, 4, 8, and 16 mg/mL). This composite PMPCM has been utilized for solar energy harvesting and EMI shielding, as depicted in Figure 1A. The dispersion of MXene has significantly enhanced both the solar-to-thermal conversion efficiency of the composite PMPCM and the SE against EMI. Figure 1B illustrates the mechanism through which MXene/PCM shields against EMI. When electromagnetic waves (EMWs) interact with the surfaces of MXene/PCMs, the presence of numerous charge carriers leads to an impedance mismatch with the surrounding environment. Consequently, a small portion of the EMWs is promptly reflected. The maximum concentration of MXene has resulted in a solar thermal conversion efficiency of 88.4%, thanks to MXene's ability to trap incident photons and the resonant effects of localized surface plasmon. The combined performance of MXene/PCM in terms of solar thermal energy conversion and EMI shielding makes it highly desirable for integration with building walls, as depicted in Figure 1C.

As well, the developed composite exhibited flame-retardant behavior, thereby ensuring safety in practical applications, as n-octadecane is an organic PCM and has a flammable nature. Subsequently, Liu et al. [44], in their research investigation, further enhanced the EMI-SE of PCM via the dispersion of MXene 10 wt%, 20 wt%, and 30 wt%) by confining the 2D materials into the matrix of PCM. In this research work PEG is opted as PCM with epoxy resin. Attributed by its strong electrical conductivity, the MXene filler improves the PCM's thermal conductivity in addition to improving the EMI-SE. Additionally, there is a significant latent heat of phase transition in PCM, and the enhanced thermal conductivity of MXene/PCM composites speeds up heat absorption and dissipation. Furthermore, by supplying surface tension and capillary forces, the distinct 2D layered structure of MXene improves the PCM's capacity to encapsulate, greatly lowering leakage during the solid-liquid transition. Figure 1D presents the intermolecular interaction occurring with the MXene-confined PCM matrix to facilitate thermal management and EMI shielding. As a result, MXene/PCM composite displayed a high EMI-E of 64.7 dB in the X-band, with a thermal conductance of 0.74 W/m·K. Figure 1E reflects the EMI SE of 30% concentration of MXene confined PCM on being tested at different thickness levels; consequently, Figure 1F displays the SE in terms of reflectance, transmittance, and the total EMW. Additionally, as can be deduced from Figure 1G, MXene's interlayer capillary action prevents liquid PCM from leaking during the solid-liquid phase transition, maintaining the PCM form stability. This MXene/PCM composite displayed effective shielding against EMI and largely improved thermal conductance, which attracts its implications in high-frequency electronic devices. PCM applied to the surface of electronic components enables their operation at temperatures near the phase change temperature. This is made possible by the phase shift mechanism of PCM, which absorbs, and stores released heat. In addition to an effective temperature control mechanism, the ability to shield against EMI is equally important for the long-term efficiency of electronic components [45]. Recognizing the urgent need for efficient thermal management and EMI shielding in electronic devices, Cheng et al. [46] have developed an encapsulated composite PCM known as MX/Ni@MS/RCG/PEG PCMs. Figure 1H showcases the PCM composite, which is enriched with the desired properties to facilitate thermal management and EMI shielding. The MX/Ni@MS/RCG/PEG composite PCMs exhibit remarkable thermal conductivity and effective EMI shielding performance, thanks to the combined influence of conductive Ni@MS/RCG networks and a well-bonded MXene film. With a phase change enthalpy of 154.3 J/g, thermal conductance of 0.47 W/m·K (74% higher than PEG), and an EMI SE of 32.7 dB, the developed composite PCM achieves the desired outcomes through the synergistic effect of MXene with the PCM composite. With a specific focus on thermal management application, Jiang et al. [47] prepared a PCM/MXene/cellulose nanocrystalline (CNC) aerogel composite PCM, specifically intended for solar TES. Tetradecylamine was opted as PCM (constant mass of 10,000 mg), whereas CNC derived from biomass was used as a supporting material (constant mass of 200 mg); where MXene the nanomaterial (mass varied as 40, 66, 200, 600, and 1000 mg). Figure 1I presents the digital image of the composite aerogel pellet; subsequently, Figure 1J displays the increase in thermal conductance of the developed composite aerogel with an increase in concentration of MXene. At higher concentration of MXene nanomaterial a thermal conductivity of 0.491 W/(m·K) (increased by 86.7%) is observed. The aerogel's 3D network structure, which provides efficient heat transfer channels for PCM and speeds up the process of heat conduction, is responsible for the increase in thermal conductance. Furthermore, the research work also evaluated the shape stability ability of the developed composite with an increase in temperature, as well an extended analysis on solar-thermal energy conversion evaluation is conducted via a solar simulator, which displays a 94.1% conversion efficiency (with 600 mg MXene) at light intensity of 100 mW/cm^2. However, at higher concentrations of MXene (1000 mg), the composite aerogel exhibits a lower value of latent heat, which considerably reduces the heat release velocity, resulting in a conversion efficiency of 68.0%.

The applications of PCM composites in thermal therapy devices and flexible wearable heaters are severely limited due to their lack of flexibility, which also causes problems with installation and inadequate contact with target device surfaces [48]. It is envisaged that flexible MXene scaffolds will be produced to overcome this problem. Because of their high elasticity and enormous porosity, carbon cloth and commercial polymer foams like melamine and polyurethane foam (PUF) have become popular substrates for building 3D continuous filler networks [49]. The filler scaffold has exceptional flexibility because of the special elasticity of polymer sponge, which enables direct stretching, bending, and twisting [50]. Shao et al. [51] reported on preparing melamine foam-supported MXene (MF@MXene) based PEG composite PCM. The developed composite of MF@MXene offered a lightweight and highly porous spongy texture that absorbed a great mass fraction of PEG, thereby enabling security against leakage issues without a significant drop in energy storage ability. Significantly, the PCM composites exhibited remarkable shape memory function by merging the phase transition of PEG with the elasticity of MF@MXene sponge. Figure 2A illustrates the preparation technique of MF@MXene/PEG flexible composite PCM; subsequently, Figure 2B demonstrates their microstructure that supports the large fraction of PEG PCM during phase transition. Compression recovery ability of the developed MF@MXene/PEG composite PCM is demonstrated in Figure 2C. Under

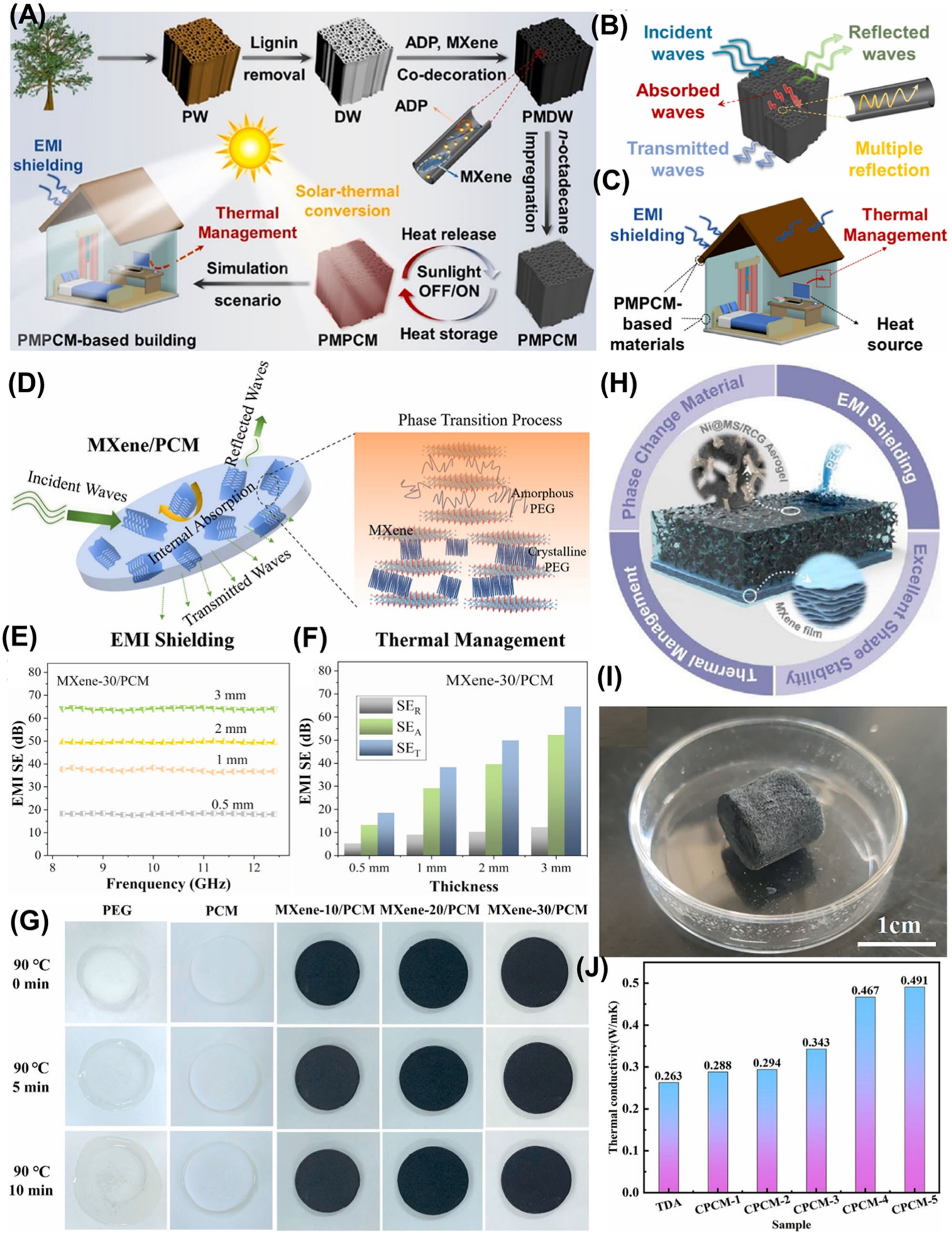

FIGURE 1 | Legend on next page.

external load, MF@MXene/PEG composite displayed quick recovery of the original height on the immediate release of applied force. Due to PCMs' strong stiffness and easily fractured brittleness, their practical usage in some industries requiring complicated shapes is frequently restricted. Henceforth the highly elastic MF@MXene/PEG were investigated to infer their behavior under near IR rays regarding the shape recovery. Figure 2D displays the shape fixing and recovery behavior of flexible MF@MXene/PEG composite with different concentrations of MXene nanomaterial. The MF@MXene sponge's large porosity and strong flexibility contribute to the exceptional characteristics of the MF@MXene/PEG PCM composites. These composites exhibit a high latent heat retention of 88.95% and an excellent shape recovery ratio of 100%. These values surpass those observed in other flexible PCM composites, highlighting the significant advantages of MF@MXene/PEG PCM composites.

MXene has a notable increase in light absorption over carbon materials because of its local surface plasmon resonance (LSPR) effect [52]. Furthermore, it has been demonstrated that MXene exhibits remarkable photo-absorption properties in the visible and near-infrared wavelength ranges. This helps to improve the solar-to-thermal conversion competence in PCM composites [53]. The brittle nature of MXene aerogels causes these composites to remain rigid, even though adding 3D aerogels to PCMs is important for increasing solar energy utilization and improving form stability. In particular, Zhao et al. [54] proposed a n-octadecane encapsulated by MXene/styrenedivinylbenzene copolymer (SDB/MXene) shell for evaluating the solar photothermal conversion behavior. Figure 2E demonstrates the infrared image of the developed encapsulated PCM with MXene at concentrations of 3%, 5%, and 10% on being exposed to solar radiation for a duration of 120 s. It is evident that the ability of MXene nanomaterials to trap solar rays causes rapid heat conductance and facilitates fast charging. Maintaining optimal heat transfer efficiency lowers temperature increases and thermal energy loss by converting solar thermal energy absorption into latent heat for storage in a timely manner. However, solar photothermal conversion behavior of MXene dispersed composite PCM varies based on concentration of MXene, type of PCM, class of composite PCM (flexible, form stable, encapsulated PCM, eutectic PCM), and so on. Henceforth, numerous research are conducted in this respect. Kalidasan et al. [41] evaluated the photothermal conversion behavior of 0.5 weight fraction of MXene with binary eutectic inorganic salt hydrate PCM intended for low-temperature thermal regulation. Tang et al. [55] studied the photothermal conversion of PEG impregnated with MXene/bacterial cellulose supporting materials. Huang et al. [56] analyzed the solar photothermal conversion behavior of dodecane (paraffin) mixed with a biomass aerogel of cellulose nanocrystal/konjac glucomannan/silver/MXene to be 97.45%. Xu et al. [17] conducted an experimental investigation to explore the solar thermal conversion efficiency of PEG dispersed with MXene as a property enhancer and raw diatomite as supporting material (form stable PCM).

A hybrid nanomaterial that combines MXene with one-dimensional CNC and ammonium polyphosphate has been developed to provide dual functionality: serving as a TES material and a fire alarm system, thanks to the sensing capabilities inherent in MXene [57]. The MXene/CNC@APP composites are well-positioned to meet the advancing requirements of next-generation MXene-based fire alarm sensors, effectively addressing the typical challenges encountered by these sensors and thereby bolstering the safety of lives and property. Subsequently, traditional shielding materials depend on reflection mechanisms, which can lead to secondary interference. Henceforth, Jang et al. [58] introduced an innovative MXene/MOF/CNT hybrid film that facilitates both EMI shielding and EMV absorption. In this study, ZIF-8 and ZIF-67 nanoparticles, each measuring under 100 nm, were synthesized on individual MXene sheets via an in-situ method. The MXene/MOF sheets were then integrated into a CNT matrix, where the interconnected CNT structure enhanced structural integrity and provided an electrically conductive network to improve EMI shielding. Transition metal carbides and carbonitrides, known as MXenes, possess atomic-layered structures and exhibit excellent electrical conductivity, making them promising candidates for the development of effective electromagnetic functional materials. However, improving their antioxidant properties and overcoming the inefficiencies associated with traditional MXene absorbers present significant challenges. In this regard, Wu et al. [59] synthesized a high-entropy MXene composed of $TiVNbMoC_3T_x$ and its magnetic hybrids. Their findings indicate that the electromagnetic coupling within HE-MXene plays a crucial role in optimizing its EMW absorption capabilities, thereby enhancing its applicability in real-world scenarios. A summary of MXene-energized PCM and its thermophysical properties are provided in Table 1. Based on existing research work, MXene dispersed composite PCM are explored regarding (a) Characterization of thermal performance (thermal conductivity, thermal stability, specific heat capacity, energy storage ability) (b) Electromagnetic shielding for buildings and electronic gadgets, (c) Thermal management, (d) Flexible MXene/PCM and its evaluation of shape recovery and flexible nature, and (e) Optical absorbance of solar radiation and its evaluation with respect to heating and cooling process with increase in temperature of PCM owing to the intensity of solar radiation.

FIGURE 1 | (A) MXene/delignified wood-based foam stable PCM for thermal management and EMI shielding of buildings. (B) Mechanism of EMI shield. (C) Real-time application of MXene-based PCM composite. Reproduced with permission: Copyright 2024, Elsevier [43]. (D) Thermal management and EMI shielding of MXene confined in shape stabilized PCM. (E) Shielding effectiveness of MXene-based composite with different thickness. (F) comparison in shielding effectiveness (total, absorbance, and reflected) of MXene-based composite PCM with different thickness. (G) shape stability evaluation of PEG, PCM, and MXene-based composite at different concentrations of MXene. Reproduced with permission: Copyright 2021, Elsevier [44]. (H) MX/Ni@MS/RCG/PEG nanocomposite PCM for thermal management of electronic devices. Reproduced with permission: Copyright 2023, Elsevier [46]. (I) Pellet of MXene/CNC-2 composite PCM. (J) Thermal conductivity of TDA and its composite with different concentrations of MXene and CNC. Reproduced with permission: Copyright 2024, Elsevier [47].

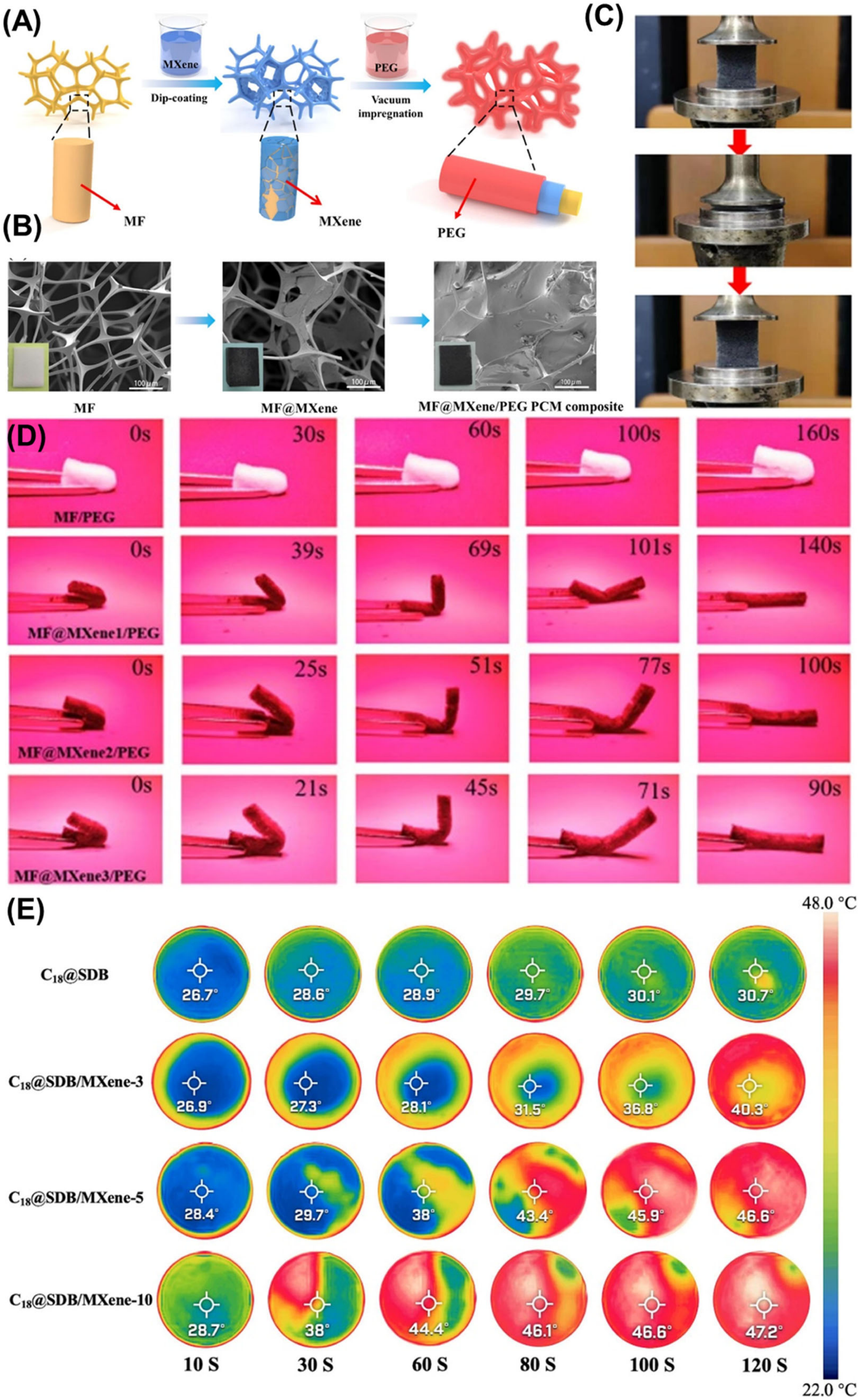

FIGURE 2 | (A) Preparation of MF@MXene-based PEG PCM composite, (B) microstructure visuals of MF, MF@MXene, and MF@MXene-based PEG PCM composite, (C) compressive behavior of MF@MXene sponge. (D) Light-actuated shape regain and recovery evaluation of MF@MXene and MF@MXene. Reproduced with permission: Copyright 2021, Elsevier [51]. (E) Thermal image of MXene dispersed microcapsule PCM on evaluation of leakage with the increase in temperature. Reproduced with permission: Copyright 2023, Elsevier [54].

TABLE 1 | A comparison of MXene-energized PCM with respect to PCM ratio, thermal conductivity, energy storage potential, and operating temperature.

MXene based PCM	PCM	PCM composite synthesis technique	PCM ratio	Thermal conductivity of PCM composite	Energy storage potential of PCM composite (J/g)	Operating temperature (°C)	References
Eutectic PCM/MXene	15% PEG6000 + 85% PEG1000	Magnetic stirring and sonication	99.2%	—	160.2	55.6	[38]
PEG4000/MXene	PEG 4000	Vacuum impregnation	77.5%	2.052	131.3	60	[60]
PEG2000/MXene with melamine foam	PEG 2000	Magnetic stirring	—	0.146	186.8	57.3	[51]
PEG2000/MXene with PVA foam	PEG2000	Vacuum impregnation	92.3%	0.428	138.0	53.2	[61]
Stearyl alcohol/MXene	Stearyl alcohol	Melting and vacuum impregnation	80%	0.486	148.0	73.3	[62]
PEG4000/MXene aerogels	PEG4000	Magnetic stirring	70%–95%	—	112.33	55–60	[63]
PEG10000/MXene	PEG10000	Magnetic stirring			101.21	59–63	[63]
Paraffin wax/MXene	Paraffin wax	Melting and blending	60%	—	120.0	61	[64]
Paraffin wax/MXene-Gelatin (45:55)	Paraffin wax	Vacuum impregnation	96.3%–97.7%	0.919	184.7	60	[65]
Paraffin wax/MXene	Paraffin wax	Melting and blending	99.7%	0.228	99.53	71.7	[39]
N-tetradecane/MXene	N-tetradecane	Melting and blending	10%	0.693	3.2	5	[66]
D-Mannitol/MXene	D-Mannitol	Magnetic stirring	80%	—	202.7	153.3	[67]

2.2 | MXene for Solar Thermal Desalination

The current water treatment processes are hindered by substantial energy and financial barriers. Advanced methods like reverse osmosis, microfiltration, ultrafiltration, and other effective water treatment technologies offer a promising solution to reduce energy costs by improving the selectivity of current membranes towards contaminant ions and molecules [68]. However, the utilization of membrane techniques in water treatment has gained significant traction over the last decade, owing to their impressive adsorption capacities and the minimal amount of energy they consume [69]. State-of-the-art materials have been created to increase separation efficiencies to a greater extent in membrane separation. When it comes to membranes that are designed to separate molecules and ions, specific 2D materials like Graphene [70], Molybdenum disulfide [71], and MOFs can be employed as the underlying foundation. The atomic thinness and lateral dimensions of these materials provide distinct advantages over 3D materials, as they effectively reduce transport resistance and enable the attainment of high permeation flux [72]. Sadly, the goal of achieving highly effective water desalination through the utilization of membranes made from 2D nanomaterials remains elusive. This is largely due to the considerable inter cell distance, which only increases in size as the membranes swell with water [73]. Several efforts have been made to prevent the expansion of swelling features to precisely regulate the interlayer gap at the sub-nano meter level and enhance ion rejection. A novel approach involves the development of 2D-material membranes that exhibit enhanced water stability and separation efficiency.

MXenes 2D nanomaterials have found their footprints over the last few years for water purification processes such as water quality monitoring [74], waste water treatment [75], and desalination of saline water [76]. For example, detecting proteins and minerals, pathogens, heavy metals, and biomolecules in portable water has been extensively explored using Ti_3C_2 MXene [77]. MXene-based adsorbents are capable of efficiently adsorbing a variety of environmental pollutants due to the number of highly active functional sites, their hydrophilic nature, and their large surface area. The exceptional qualities of MXene, including its adsorption, conductivity, hydrophilicity, and antibacterial activity, have created new opportunities for its application in water treatment. These applications include adsorption [78], oxidation processes [79], membrane techniques [70], antifouling microbes [80], and electrochemical treatment. MXene's diverse range of capabilities positions it as a promising material for improving water treatment processes and combating water pollution. $Ti_2C_2T_x$ nanosheets can degrade micro pollutants, such as diclofenac, by means of ultraviolet (UV)-based photocatalytic reactions. Furthermore, MXenes show promise as electrode materials for desalination and capacitive de-ionization processes. Furthermore, comparing MXene-based membranes to traditional membranes used in desalination and drinking water treatment, the former offer better flux performance and reduced susceptibility to biofouling [81]. This highlights the significant role of MXenes in the water treatment and environmental remediation sector.

Solar desalination is a method that utilizes solar power to transform salty water into clean, drinkable water, as well as water suitable for irrigation purposes. The classification of this process depends on the specific solar energy source that is employed. Solar-driven saltwater desalination appears to be an affordable and practical way to address these problems given the wealth of solar energy at our disposal. It achieves a comparatively high evaporation efficiency, which permits the use of solar energy to obtain fresh water [82]. Solar salt rejection is the technique employed to extract salt from water using solar energy. In this process, solar radiation is absorbed by a material and transformed into thermal energy. A saline solution receives the energy transfer, and vaporized water rises through the hydrophilic layer of a salt-rejecting membrane. It is evident that the effectiveness of this process depends on the material's capacity to absorb solar radiation; for this reason, materials such as plasmonics, carbon-based compounds, and metal nanoparticles are being researched. However, these materials are not as effective in converting solar radiation into usable energy, and they have a low light-to-thermal conversion efficiency and weak hydrophilicity for water transport.

Due to their exceptional light-to-heat transmission efficiency, MXenes emerge as excellent candidates for solar-powered desalination [52]. Furthermore, these captivating 2D materials exhibit energy-efficient properties, including their ability to facilitate photo-thermal water evaporation. MXenes exhibit the ability to absorb a broad spectrum of solar energy and achieve close to 100% conversion from light to heat, positioning them as a prime option for harnessing solar power. High hydrophilicity in MXenes enhances water transport efficiency [83]. However, the re-stacking of MXene sheets can hinder capillary water transport necessary for solar thermal desalination. Furthermore, the accumulation of salt on the solar absorber may obstruct water transport pathways. The pursuit of a solar-based steam generation device that can sustainably desalinate water over an extended period continues to be a greater obstacle in achieving optimal thermal management, salt rejection, and mechanical strength. Wang et al. [84] designed a biodegradable interfacial solar steam generation (SSG) device using a 3D Janus MXene/cellulose nanofibers (CNFs)/luffa (JMCL) aerogel, which exhibits outstanding mechanical properties. In the design of JMCL aerogel, Wang et al. [84] have successfully merged the multifunctionality of fast water transport, efficient thermal management, rapid vapor escape, and effective photo-thermal conversion into a single-module configuration. This pioneering design exemplifies their ingenuity and expertise in material engineering. Figure 3A,B displays the schematic of JMCL aerogel designed with ISSG system along with the operational mechanism. The JMCL aerogel, characterized by its porous nature, serves as a pioneering framework for light absorption, thermal regulation, and water conveyance (as represented in Figure 3C). On the other hand, the luffa sponge acts as a secondary framework, reinforcing the mechanical robustness. The incorporation of the Janus structure imparts the JMCL aerogel with contrasting wettability properties. The hydrophobic bottom half of the JMCL aerogel gains its phenomenal ability to float on water by applying a polydimethylsiloxane (PDMS) treatment, which also considerably lowers the water's heat loss. On the other hand, the hydrophilic upper section is engineered to achieve optimal heat localization, uninterrupted water conveyance, and effective salt rejection. JMCL aerogels demonstrate a mechanical strength 437 times greater than MXene/

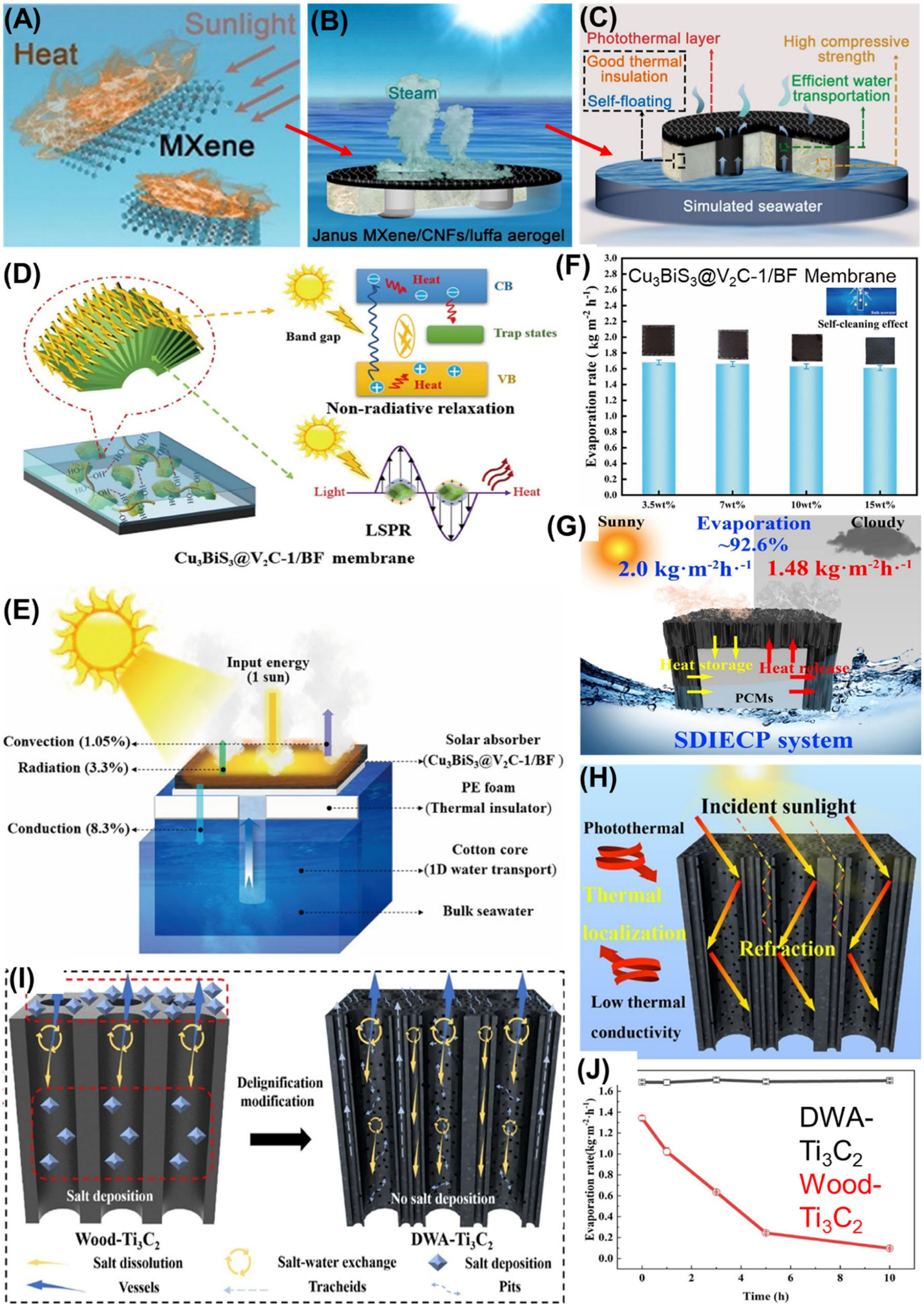

FIGURE 3 | (A) Basic schematic of MXene based membrane used for solar desalination. (B) Solar steam generation using JMCL aerogel. (C) Conceptual representation of SSG system. Reproduced with permission: Copyright 2023, Elsevier [84]. (D) Mechanism of photo thermal conversion occurring in $Cu_3BiS_3@V_2C$/BF membrane. (E) representation of heat loss occurring from the designed evaporated. (F) evaporation rate of different concentration saline water using $Cu_3BiS_3@V_2C$/BF membrane. Reproduced with permission: Copyright 2024, Elsevier [85]. (G) Representation of SDIE system integrated with PCM. (H) Thermal localization mechanism of DWA-Ti_3C_2. (I) Schematic of DWA-Ti_3C_2 and Wood-Ti_3C_2 based SDIE. (J) Evaporation rate comparison between DWA-Ti_3C_2 and Wood-Ti_3C_2 equipped in SDIE. Reproduced with permission: Copyright 2023, Elsevier [86].

CNFs aerogels. When subjected to indoor solar illuminator testing, JMCL aerogels achieved a water evaporation rate of 1.4 kg/(m^2·h) and an efficiency of 91.2%. A new era in solar desalination was ushered in by Zhao et al. [87] with their report on the development of a hydrophobic surface-enabled 2D Ti_3C_2 MXene membrane. The layer of Ti_3C_2 was prepared by eliminating the MAX phase using HCl/LiF followed by vacuum deoxidation and sonication. The hydrophobic membranes were then generated through surface modification. The self-floating device achieves a solar evaporation rate of 1.31 kg/(m^2·h) and a solar steam conversion efficacy of 71% thanks to its design, which includes high light utilization, stability, multiple evaporating channels, efficient water transport on filter membrane, and salt-blocking on MXene membrane. It guarantees long-lasting and efficient photothermal transduction for the purification of water from saltwater and wastewater that contains organic dye and heavy metal contaminants. It also shows resilience in high salinity settings when exposed to sunlight for more than 200 h. By virtue of its hydrophobic surface, the membrane exhibits a remarkable ability to block salt, thereby ensuring the purity of the desalinated water. This innovative solution effectively addresses a critical challenge in the field of desalination, where salt permeation can impede efficiency and contaminate the final product. Furthermore, the membrane's exceptional stability under solar irradiation guarantees consistent performance over time, establishing it as a reliable choice for solar-powered desalination systems. The research conducted by Xu et al. [85] introduced a bilayer structure of MXene-based Cu_3BiS_3@V_2C/Basalt fabric photo thermal membranes, designed for solar steam generation, electricity production, and water purification. Design comprised of top Cu_3BiS_3@V_2C nanocomposite, and at bottom a stable basalt fabric membrane with a porous structure. The top-bottom interface matching is accomplished through the readily cross-linked effect of the carboxylate groups in nanocomposites and the calcium ions in the basalt fabric membrane. This ensures the remarkable stability, durability, and effective photothermal conversion in the complex marine environment. Results depicts increase in optical absorption of electromagnetic radiation under 300–2500 nm to be 95.2%, which through the combined design of multistage photo thermal conversion, displayed significant evaporation rate of 1.68 kg/(m^2·h), alongside a decrease in evaporation enthalpy. Figure 3D presents the mechanism of schematic of photo thermal conversion of the developed membrane along with the evaporation of sea water and its condensation to pure water (Figure 3E); subsequently, the performance of developed membrane in terms of evaporation rate at different concentration of saline water is in Figure 3F.

By employing a layer-by-layer self-assembly method, Zhou et al. [82] constructed a dual-layer functional nano-coating over the surface of flexible polyurethane (FPU) foam. This nano-coating consisted of 2D MXene and 0D polyethyleneimine-modified silica nanoparticles ($mSiO_2$-NP@PEI). The resulting modified FPU (MFPU) is designed to possess flame retardant properties, enhance the materials' photo thermal conversion capacity, and contribute to the field of solar-driven desalination applications. The experimental analysis conducted using an indoor solar simulator confirmed the exceptional light-to-heat conversion and solar water desalination capabilities of MFPU foams. With the application of three coatings, the MFPU foam was able to achieve a temperature of 120°C in just 138 s. Furthermore, the steam conversion efficiency reached an impressive 89.6%, marking a significant 116.0% increase compared to unmodified foam. The implementation of this innovative strategy offers a promising solution to the challenges of fire safety in materials. Moreover, it leverages renewable energy for water desalination, making notable contributions to both environmental sustainability and technological progress. To tackle the rapid heat dissipation problem in oriented cell walls of aerogel utilized for solar thermal desalination, Ding et al. [88] developed an MXene-based porous structured composite aerogel (MCA). This MCA is composed of unidirectional cell walls of polyvinyl alcohol (PVA)/$Ti_3C_2T_x$ and cross-linked CNF within a multiscale 3D porous structure. By filling the aligned pores with cross-linked CNF, the developed MCA exhibits superior hydrophilicity, thermal insulation (56.54 mW/(m·K)), and solar absorption (97.9%), resulting in a high solar-thermal evaporation efficiency. By experiencing the swelling and dehydrating process, the MCA experienced volume variation, leading to tuneable electrical conductivity in MCA. This change in conductivity is straight linked to the water absorption, which in turn can significantly affect the brightness of a LED light bulb when the water is dipped. The sensitivity of this process is notably high. This study presents a wide-ranging opportunity for the progress of multifaceted MXene-based composite aerogels, showcasing their exceptional porous architecture. Though solar driven interfacial evaporation (SDIE) system turns to better option for desalination process, the issue of low energy efficiency owing to the intermittent nature of solar radiation and the issue of salt accumulation during continuous desalination process remains to be major obstacle. Henceforth Gao et al. [86] presented a novel approach to achieve high-efficiency and continuous desalination by utilizing a sandwich-structured MXene/wood aerogel combined with PCM (1-Tetradecanol) in the evaporator. By incorporating a multistage water transport channel in the design and leveraging the enhanced thermal localization effect of MXene and wood aerogel, we have successfully optimized the performance of the evaporator. In this experimental investigation the impact of DW aerogels with MXene (DWA-Ti_3C_2) and Wood-Ti_3C_2-based membrane integrated with SDIE and SDIE + PCM is evaluated. Figure 3G displays the SDIE system integrated with PCM to enhance the evaporation rate during intermittent nature, meanwhile Figure 3H presents the mechanism of thermal localization occurring in DWA-Ti_3C_2. A comparison in terms of scheme (Figure 3I) and the evaporation rate of saline water (Figure 3J) between DWA-Ti_3C_2 and Wood-Ti_3C_2 based SDIE system integrated system is also inferred. Evaporation rate of SDIE system coupled with PCM and DWA-Ti_3C_2 reached 2 kg/(m^2·h) under direct sun at an efficiency of 92.6% was observed, whereas under intermittent solar radiation the evaporation rate was 1.77 kg/(m^2·h). The rapid evaporation rate can be attributed to the combined impact of the strong light absorption, photo thermal conversion of Ti_3C_2, and the anisotropic hierarchical porous structures of DWA, which enable thermal localization and effective water transportation. Furthermore, the high solar efficiency is achieved through the recycling of energy loss in evaporation by PCMs.

Addressing water scarcity can be effectively achieved through the adoption of efficient and eco-friendly SDIE technologies, which can produce clean water. In this regard, the research on photo thermal materials has emerged as a central focus within the realm of SDIE systems. With the evaporation efficiency of solar evaporators approaching 100%, the efficacy of vapor generation in sunshine has been greatly increased in recent years due to scientists' intensive study on photothermal materials and SDIE technology [89]. Even with the successful synthesis of many MXenes in a lab setting, the manufacturing method can still be scaled up for greater efficiency. Addressing the oxidation stability of the isolated MXene dispersion is the primary difficulty [90]. In addition, it is imperative to consider the possibility of commercialization while maintaining the affordability and ecological friendliness of MXenes. Lee et al. [91] have chosen MXene-derived TiO_2/Ti_3C_2 hybrids integrated with plasmonic Ag nanoparticles for the treatment of waterborne pollutants. Their research aimed to synthesize a range of hybrid nanomaterials specifically for the photocatalytic degradation of these pollutants. The resulting TiO_2/Ti_3C_2 hybrids were subsequently enhanced with Ag nanoparticles to leverage the surface plasmonic resonance effect, which is recognized for its ability to enhance photocatalytic performance. Jahangir et al. [92] developed a novel approach utilizing Co_3O_4 nanoparticles/Ti_3C_2-MXene hybrid material as dual-function agents for the simultaneous transport of photogenerated holes and catalysis of the water oxidation reaction. The integration of the Co_3O_4/Ti_3C_2-MXene hybrid significantly decreased the surface recombination rate constant and greatly improved charge transfer efficiency. Furthermore, due to its higher work function compared to $BiVO_4$, the Ti_3C_2-MXene layer forms a Schottky-like junction, creating a built-in electric field that facilitates the movement of photogenerated holes toward the Ti_3C_2-MXene/$BiVO_4$ interface. A summary of recent works on MXene towards enhancing the solar desalination performance is presented in Table 2. MXenes have a great deal of promise for desalination and water purification technologies. Membranes made of $Ti_3C_2T_x$ have proven to be stable and effective in water desalination operations. Scientists must focus on creating novel MXenes-based nanocomposites going forward to desalinate water, with a focus on enhancing solar desalination and capacitive deionization performance. Currently, it is thought that the cost of making MXenes is excessive given the amount of product produced [93]. Low yields are the consequence of the fact that MXenes are mainly produced in small amounts in laboratories. Novel approaches to the large-scale synthesis of MXenes that are economical, ecologically benefits, and efficient will propel this field's research forward and open new business prospects. For mass production, this means that costs should drop dramatically.

2.3 | MXene for Mechanical Energy Harvesting Applications

The world has been facing a severe issue with the lack of energy. Creating abundant, inexpensive, and sustainable energy sources is one of the most important projects for our contemporary society. Numerous efforts have been undertaken to identify renewable energy sources, such as wind, solar energy, and hydropower. Energy harvesting devices play a crucial role

TABLE 2 | Summary of MXene-based solar desalination units.

MXene membrane	Uniqueness of the research	Operating temperature (°C)	Solar condition	Water evaporation rate	Solar thermal efficiency	References
Copper selenide/MXene	Solar-driven water evaporation	63.5	Under six suns	12.60kg/(m^2·h)	—	[94]
MXene based monoliths	Light-to-heat-to-electricity and freshwater generation	129	Natural light 0.91 kW·m^{-2}	1.39 kg/(m^2·h)	82.9%	[95]
Cu_3BiS_3@V_2C/BF membrane with bimetal sulfide/V_2CT_x MXene	Solar steam generator with electricity and water purification	42.1	Under one sun	1.68 kg/(m^2·h)	95.2%	[85]
MXene/PDA hydrogel	Highly efficient solar evaporation and desalination unit	38.7	Under one sun	3.02 kg/(m^2·h)	94.7%	[96]
Superhydrophobic fabric composite membrane	Superhydrophobic MXene fabric based solar desalination	64	Under one sun	1.526 kg/(m^2·h)	93.3%	[97]
MXene/wood aerogel	Sustainable solar-driven interfacial evaporation	39.5	Under one sun	1.77 kg/(m^2·h)	92.6%	[86]
Polyimide/MXene hybrid aerogel	MXene/PCM-based desalination unit	74	Under one sun	1.24 kg/(m^2·h)	87.28%	[98]

in reducing carbon emissions and utilizing renewable energy sources by efficiently gathering and transforming dissipated energy from everyday living or the environment into electrical energy needed for various applications. Since energy harvesters can produce power without burning fossil fuels, they are seen to be one of the most appealing solutions to the energy and carbon emission problems. Considering this, different energy harvesting technologies have been developed, such as triboelectric nanogenerators (TENGs), piezoelectric nanogenerators (PENGs), electromagnetic generators, and thermoelectric generators. Of these, TENG is seen as a possible substitute because of its ability to produce high-voltage electricity from mechanical energy, which arises from the combination of electrostatic induction and contact-induced electrification. Mechanical energy is a type of energy found throughout nature, including motion, movement, and vibration. The functioning of various machines and human actions creates mechanical energy [99–102]. Efficient capturing, utilization, and usage of this energy is predicted to result in self-supply in a variety of microsystems while significantly reducing energy losses. TENGs have several benefits, including lightweight, cheap cost, and an easy construction procedure. Numerous TENG-based self-powered applications, including electronic skin, medical sensors, wave energy harvesting, and environmental screening sensors, were developed with the significant advantages of TENGs in mind. However, to apply the self-powered applications, the large dimensions of a TENG-based self-sustaining system are necessary to create sufficient electrical power, which makes the use of the TENG in everyday life impracticable [103–106]. Mechanical sensor technology has advanced significantly in recent years thanks to advances in material innovation, structural engineering, and systematic device integrations. Technological innovations and advancements in the wearable gadget industry have resulted in high customer demand. Therefore, creating energy-saving devices is of the utmost significance. Mechanical generating devices that are small, integrated, multifaceted, electronic, stable, scalable, and have a high energy density are becoming increasingly common due to the development of flexible materials. These devices find application in human-computer interaction, underwater research, smart homes, transportation, self-powered devices, and in vivo biomedical science. In the field of soft robotics and wearables, flexible energy harvesting devices are crucial because they can adjust to the circumstances surrounding irregular objects, soft bodies, human bodies, and so forth, and allow electronic devices or structural components to mimic the mechanical properties of biological tissues more accurately. Flexible materials that capture energy have the potential to run on their own, which lowers energy usage. Investigating more effective materials for generating electricity and the relationship between the structure of materials and energy harvesting are crucial [99–107].

The microscopic and bulk electrical characteristics of MXenes are greatly influenced by their composition, which may influence TENG performance. The surface termination composition affects the local surface dipole moments and Fermi level, which modifies MXene's work function. It was demonstrated that enhancing the hydroxyl concentration of functional groups decreased the work function while a higher concentration of oxygen functionalities enhanced the work function. As recently shown for $Ti_3C_2T_x$ in an MXene-based TENG, these intentional modifications to the TENG materials work function have shown the ability to increase the triboelectric voltage output. Because of their hydrophilic character, colloidal stability, and adjustable chemistry, MXenes are superior fillers than other widely used materials such as silica, TiO_2, Ag nanowires, $BaTiO_3$, nanocarbons, and so forth. MXene may be treated to provide a range of features, including carrier transport, energy conversion, selective permeability, adjustable electrical properties, electromagnetic shielding, and more, in a straightforward and affordable manner. Moreover, MXene's great adaptability enables it to be mixed with a range of materials to create flexible materials with unique characteristics for a broad range of applications. The electrical, thermal, and ionic properties of MXenes can be optimized to improve the flexible material's energy-harvesting performance in various ways. Additionally, the functional groups of MXene can modify and adjust the material's properties to obtain appropriate properties under various application conditions, such as cathode/anode properties, adjustable electrical conductivity, and ionic filtration. Additionally, MXene may be composited in several ways with other flexible materials [99, 100, 103, 108].

Rani et al. [108] used polyvinylidene fluoride (PVDF)-MXene as the negative tribolayer and PAN@ZIF-67 as the positive triboelectric layer to fabricate the TENG device. Figure 4A schematically represents the synthesis protocol of electrospun PVDF@MXene nanofibers. Fabricated TENG device functioned in vertical contact–separation mode. MXenes are deposited in varying quantities to PVDF; MXene enhances the charge transfer capabilities of TENGs. With a power of 305 V, 10.9 W/m^2, and 10.6 μA, the improved TENG device has shown potential for self-powered sensing and energy harvesting. The assembled device glowed 40 LEDs under hand tapping, instantly charged commercial capacitors, powered portable clock LCD, and was utilized to examine human motions as the self-powered sensor. Figure 4B represents the sensing and real-time applications of the TENG mounted at various places on the smart door and harvested electrical behaviors of the TENG device while door opening, door tapping, door knocking, tapping leg, and playing calling bell "music on" and "music off" [108]. The challenging conditions at sea level can have a detrimental impact on the performance of TENGs used for blue energy harvesting. Sun et al. [109] incorporated MXene into a PVA layer to improve anti-fouling behavior, dielectric property, moisture resistance, and wear resistance of the PVA-MXene tribo electrode. Figure 5A represents the schematic representation of the PVA-MXene film synthesis methods, cross-linking mechanism, and microstructure. The formation of the hydrogen bond process between water molecules and PVA at high humidity is depicted in Figure 5B. Assembly of the micro-capacitor through MXene sheets and PVA is shown in Figure 5C. This enhancement enables effective electrocatalytic water sterilization and energy generation in challenging environments. The PVA tribo-electrode's anti-fouling, moisture resistance, dielectric characteristics, and wear resistance were improved by optimizing the MXene doping ratio. Eight weight percent MXene doping provides a hydration layer; MXene doping enhances the anti-fouling performance of PVA by increasing the number of hydrogen bonding sites on its surface, which allows for the adsorption of larger molecules of water as electro positivity materials. Concurrently, MXene boosts the hybrid

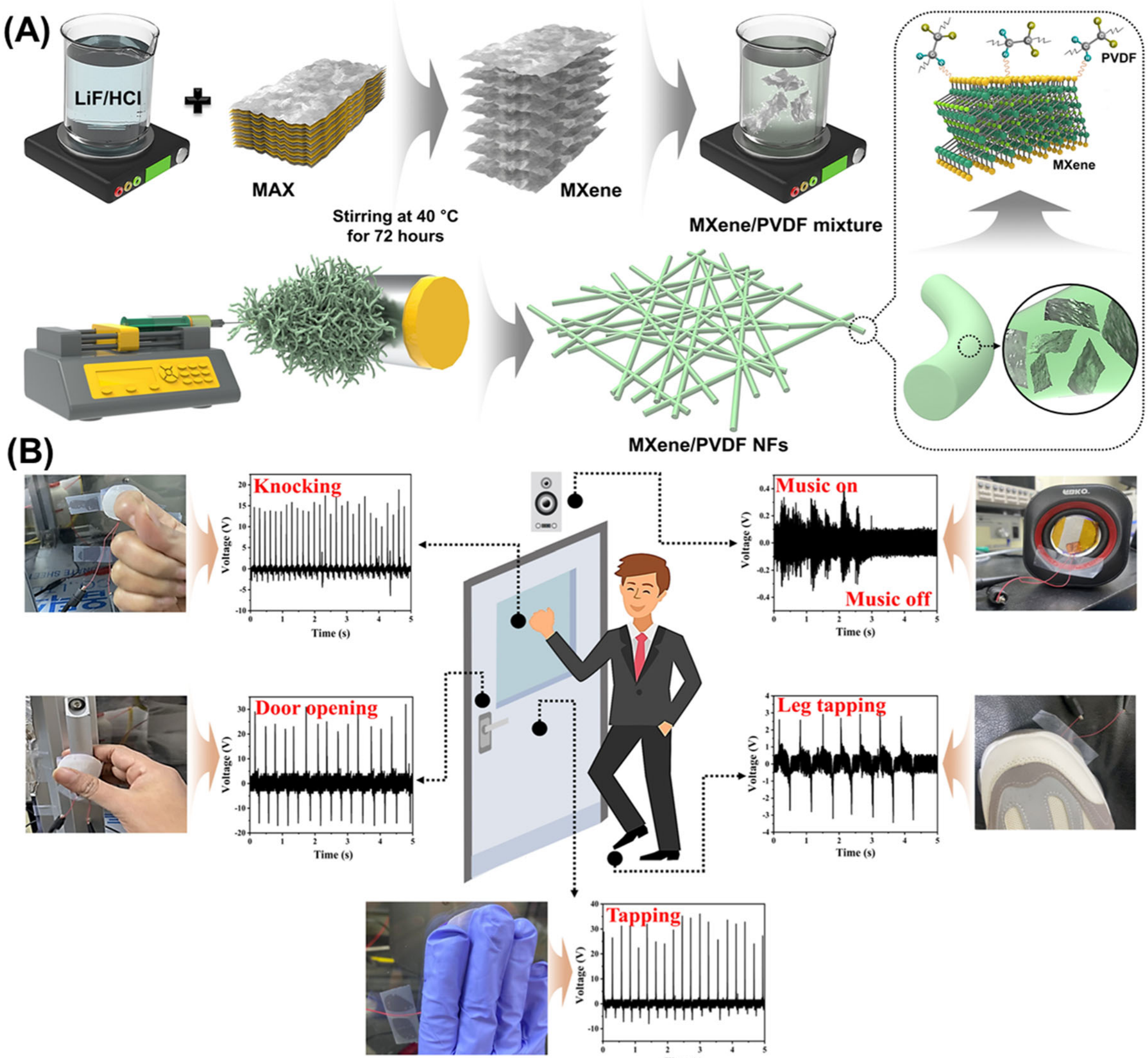

FIGURE 4 | (A) Schematic representation of synthesis protocol of electrospun PVDF@MXene nanofibers. (B) Sensing and real-time applications of the TENG placed at various places on the smart door. Harvested electrical behaviors of TENG device while door opening, door tapping, door knocking, tapping leg, and playing calling bell "music on" and "music off". Reproduced with permission: Copyright 2023, Wiley-VCH [108].

transfer film's load capacity, significantly enhances the PVA film's wear resistance, and can create a microcapacitor to enhance the dielectric characteristics of the film. Furthermore, a biomimetic PVDF electrode was created by mimicking the hydrophobic process of leaves, which greatly enhanced PVDF's resistance to fouling and moisture. The current and voltage of the fabricated TENG reached 36.6 μA and 1056 V at a humidity of 95% and enhanced by 2.37 times. The triboelectric enrichment mechanism and moisture resistance phenomenon of PVA/MXene-PVDF TENG is exemplified in Figure 5D. This signifies the influence of the hydrogen bonding coupling and improvement of the micro-capacitor. Figure 5E depicts the schematic figure of self-powered sterilization of the water system. C-Cu_2O/AgNPs bactericidal filtration electrode synthesis approach is demonstrated in Figure 5F. The binding energy and charge density of PVA and PVA-MXene after and before absorbing the water molecules were estimated by using DFT calculations. Furthermore, at 2000 mL/min flow rate, designed self-powered water sterilization device based on PVA/MXene/PVDF-based TENG obtained a 98.99% sterilization rate, which was much greater than standard AC power (86.80%) [109].

He et al. [110] prepared a high-precision TiO_2-CuO-MXene-based ethanol sensor operational at 25°C. Due to p-n heterojunction generated by CuO and TiO_2, the abundance of functional groups and MXene extensive specific surface area, as well as its exceptionally low LOD (0.3 ppm), recovery time (13 s)/quick response (16 s), and impressive stability over time for trace identification of the ethanol gas at the room temperature. Further, the sensor displays outstanding response values (95% @1 ppm ethanol). Additionally, the silicone or MXene@silicone double dielectric layer was introduced as a triboelectric layer to create an efficient TENG. This significantly improves the TENG's output performance by increasing the dielectric layer's capacity for storing charge. The SMS-TENG's open-circuit voltage may reach 1160 V at the ideal doping ratio, which is enough to light 720 LEDs. The resistive responsiveness of ethanol sensing is transformed into a voltage response through the combination of the sensor with SMS-TENG, which

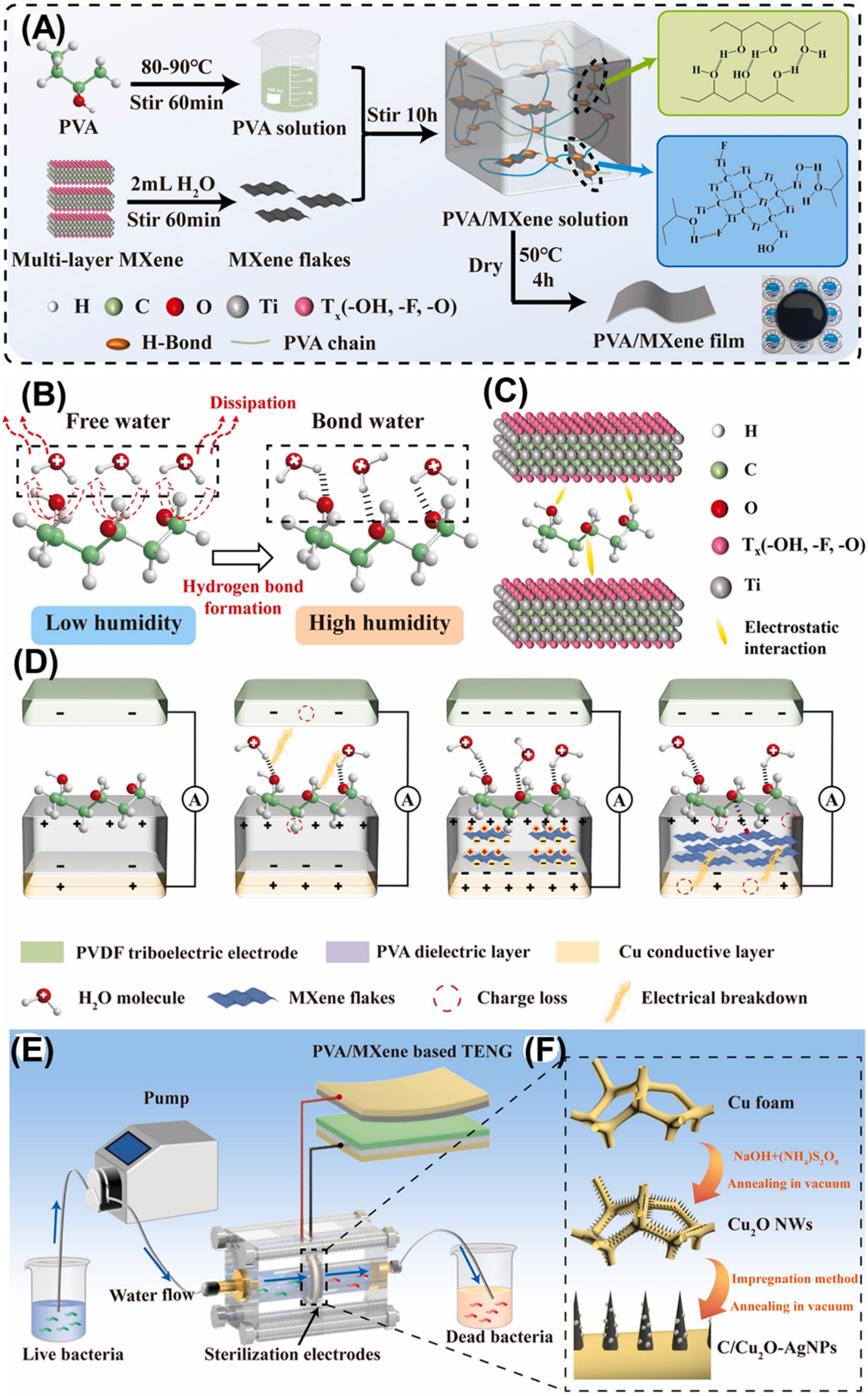

FIGURE 5 | (A) Schematic representation of the PVA/MXene film synthesis methods, cross-linking mechanism, and its microstructure. (B) Schematic of the formation of the hydrogen bond process between water molecules and PVA at high humidity. (C) Schematic of the assembly of assembly of the micro-capacitor through MXene sheets and PVA. (D) Triboelectric properties enrichment mechanism and moisture resistance phenomenon of PVA/MXene-PVDF TENG. (E) Schematic figure of the self-powered sterilization of water system. (F) C-Cu_2O/AgNPs bactericidal filtration electrode synthesis approach. Reproduced with permission: Copyright 2023, Elsevier [109].

increases the response value to 15.8 times. To create a self-powered ethanol recognition alarm system and enable the inspection robot to detect ethanol at the ppb level, the designed SMS-TENGs are anticipated to be arrayed on the robot as an energy supply and paired with the TiO_2-CuO-MXene ethanol sensor [110]. Tan et al. [111] prepared a biocompatible and high-performance porous TENG with friction layers made through PDMS sponge and MXene-silk fibroin composite aerogel (SF@MXene-A). The inclusion of the MXene into silk fibroin aerogel improved the specific surface area and the resultant charge density of the surface, delivering an approach for the construction of high-performance aerogel TENG. A ratio of about 1:1 between MXene and silk fibroin allows the TENG with the biocompatible silk fibroin aerogel to operate at peak efficiency, producing an optimal voltage of 545 V and a maximum current of 16.13 μA [111]. In adverse environments, developing high-performance TENGs remains hindered by triboelectric materials' weak stability, irreversible surface, and low surface charge density. Specifically, because 2D MXene materials are hydrophilic, water molecules tend to erode their surfaces under high humidity, which reduces TENG stability and output performance. In this esteem, Sardana et al. [112] developed a methodology for designing a contamination and humidity-resistant MXene-based TENG utilizing an electrospinning strategy. Initially, MXene/MoS_2 composites mixed in polymer cellulosic matrix were used to create nanofibrous layers, which benefited from the regulated air-trapping holes and high surface roughness. Moreover, stearic acid was chemically added to the produced nanofibrous layers to improve the hydrophobic properties and the electronegativity of the resulting MXene/MoS_2 composites. Four distinct combinations of MXene-MoS_2-cellulose acetate nanofibers have been produced in a typical synthesis. This shows that an increase in MoS_2 concentration would efficiently modify the surface oxidation, hydrophilicity, and roughness of MXene in addition to inducing an enhanced triboelectric potential due to piezoelectricity. Conversely, the stearic acid modification finally produced a low surface energy superhydrophobic surface with water contact angle of around 154°. Under conditions of high humidity, the integrated TENG demonstrated a long-term stable enhanced output voltage of around 140 V and an instant power density of approximately 2975 mW/cm^2. Furthermore, self-cleaning qualities were shown, assuring the TENG's durability and reusability in a polluted environment. Furthermore, utilizing the liquid-solid contact-electrification TENG mode of operation, the synthesized MXene-based superhydrophobic layer can capture energy from dropping water droplets. This work directs the research on the effective harvesting of dispersed ambient energy and lays the path for designing and developing triboelectric materials resistant to contamination and humidity [112]. PVA film composites with humidity-sensitive capabilities were created as friction layers to attain self-powered TENGs with better electrical performance under humidity by exploiting the synergistic impact of lithium chloride (LiCl) and MXene [113]. The composite material has a strong linear association with rising humidity and displays remarkable and steady output performance throughout the humidity range (30%–95%). The short-circuit current of PVA and PTFE-fabricated TENG (P-TENG) increases to 31.91 μA at 95% RH, which is three times its output. The composite material's water absorption capability and surface roughness are greatly enhanced by the abundant hydroxyl group in the PVA, LiCl high hygroscopicity, and microcapacitor system created by the MXene nanosheets. This leads to a good triboelectric output for the TENG. The TENG's short-circuit current has exceptional adsorption-desorption performance as humidity drops and responds very sensitively to changes in ambient humidity across a wide range of relative humidity (from 50% to 98%). Additionally, TENG, which is thought of as a power supply under high humidity conditions, was developed and can instantly light up 240 LEDs, with a 194.37 $\mu C/m^2$ transfer charge density. With the help of this advancement, consistent energy generation and self-powered sensing in high-humidity conditions like fog and the ocean can be possible [113]. The impact of MXenes' adjustable chemistry on triboelectric power production remains largely unexplored, despite the increasing interest in these materials for energy applications. The chemical makeup of MXenes, especially Ti_3CNT_x carbonitride versus $Ti_3C_2T_x$, the carbide that has received the most attention, was examined by Wicklein et al. [114] to determine how it affected the interactions of MXenes using sodium alginate and subsequently, the efficiency of the TENG device. Obtained results suggested a synergistic effect is produced by adding 2 weight percent of Ti_3CNT_x to alginate, which leads to greater triboelectric activity than the $Ti_3C_2T_x$ structure. According to spectroscopic investigations, Ti_3CNT_x surface has a greater oxygen and fluorine content, which promotes hydrogen bonding with the sodium alginate matrix and raises the alginate oxygen atoms' surface charge density. This was further verified by Kelvin probe force microscopy, which demonstrated a higher negative surface potential on Ti_3CNT_x-alginate, allowing for significant charge transfer across TENG electrodes. The improved Ti_3CNT_x-alginate TENG produced 670 V, 0.28 W/m^2, and 15 μA. Further additional oxidation of the MXene surface by plasma might enhance the triboelectric performance. Ti_3CNT_x-alginate can serve as a tribonegative or tribopositive material based on the counter-contacting material since MXene has different surface terminations. The results obtained offer a more profound comprehension of how the composition of MXene influences its interactions with biopolymers and the adjustable triboelectrification behavior that follows [114]. With the fast advancement in self-powered gadgets, intelligent wearable electronics are urgently required to overcome the constraints of traditional power sources. Single-electrode TENG has gained popularity because of its ease of manufacture, portability, and application as an energy source for wearable gadgets that use electricity. He et al. [115] developed a responsive, flexible, and multifunctional single electrode TENG based on the chitin nanocrystals (ChNCs) and the MXene film (CM-TENG). Figure 6A shows the schematic sketch of MXene nanosheets synthesis. SEM images of Ti_3AlC_2 and m-$Ti_3C_2T_x$ were shown in Figure 6B,C. MXene TEM image was portrayed in Figure 6D. MXene, m-$Ti_3C_2T_x$, and Ti_3AlC_2 XRD patterns are shown in Figure 6E. ChNCs serve as interface adhesives to make it easier to assemble MXene nanosheets, which greatly enhances the mechanical and electrical conductivity of the composite film. ChNCs structure is shown in Figure 6F. TEM image of ChNCs was portrayed in Figure 6G. The MXene nanosheet surfaces' negative charges are neutralized by positively charged ChNCs, allowing the composite film to transfer the charges quickly during the electrostatic inductive procedure. The liquid stage exfoliation procedures aid in providing rich surface-active groups (−F, −OH, and −O) and

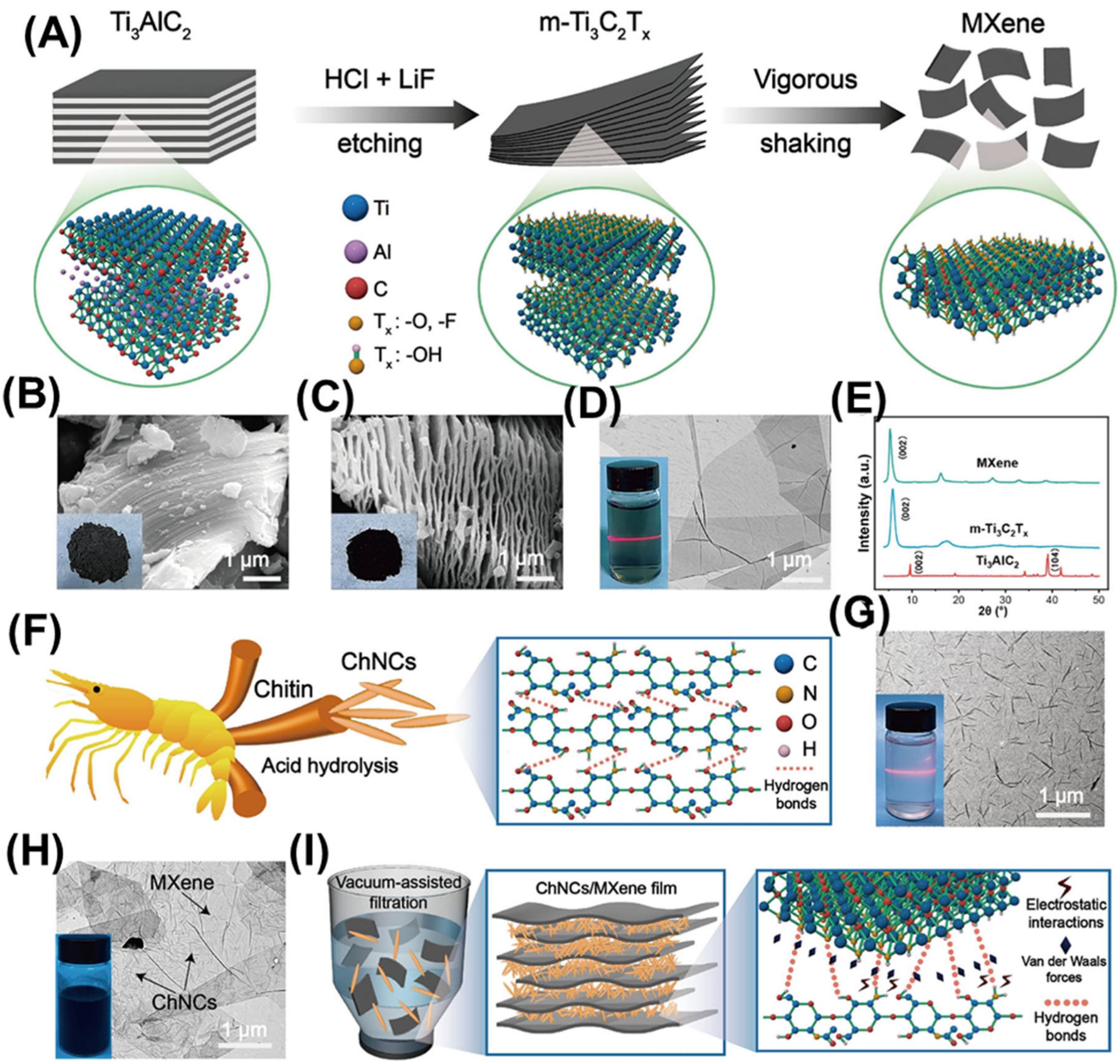

FIGURE 6 | (A) Schematic sketch of MXene nanosheets synthesis. (B) and (C) SEM images of Ti_3AlC_2 and $m\text{-}Ti_3C_2T_x$. (D) MXene TEM image. (E) MXene, $m\text{-}Ti_3C_2T_x$, and Ti_3AlC_2 XRD patterns. (F) ChNCs structure. (G) ChNCs TEM image. (H) Layers of MXene attached with ChNCs. (I) ChNCs-MXene composite film preparation process through vacuum assisted filtration approach. Reproduced with permission: Copyright 2024, Elsevier [115].

hydrophilic properties, which supported ChNCs to adsorb easily onto MXene nanosheets surface (Figure 6H). ChNCs MXene composite film preparation process through vacuum aided filtration approach (Figure 6I). The CM-TENG electrical performance achieved up to 99.5 mW/m^2 of power density, hence the fabricated device can be used as tactile and strain sensors. This study provided an approach to electrostatically driven self-assembly of ChNCs and MXene, which has interesting applications in low-frequency mechanical energy harvesting and self-sustaining wearable electronic devices [115].

Lai et al. [116] developed a procedure PVA modulating PEG to aid the movement of cations along the polymer chains, which substantially boosted the performance of hydrogel in PPh TENG. This was further increased by incorporating Ti_3C_2 layered nanosheets, which serve as ionic conductors. The streaming vibration potential, an effective electrostatic mechanism introduced by these nanosheets, greatly enhances the operation of the gadget. Figure 7A schematically depicts the MXene nanosheets surface functionalization process within PVA-borax-PEG hydrogel utilized in TENGs. Figure 7B clarifies the movement of the water molecules over the MXene nanosheets, which substantially increases the tribo charges produced on the surfaces. Figure 7C illustrates a 3D network structure in the PVA-MXene-PEG hydrogel TENG and its mechanism, emphasizing MXene microchannels role. Moreover, the utilization of CPTMS and FOTS to alter the MXene nanosheets surface to design F-MXene and Cl-MXene hydrogel TENGs, labeled as F-MPPh and Cl-MPPh TENGs, respectively. Figure 7D demonstrates the SVP mechanism and how the compressive stress convinces a positive flow of charges in Ti_3C_2 microchannel. The streaming vibration potential influence is improved by the altered nanosheets of MXene in the hydrogel, which is further significant than the un-altered nanosheets of MXene. This is explained by the fact that the electrically charged double layer that forms between the water and nanosheets of MXene has a greater charge density. Figure 7E shows the influence of tensile stress, illustrating the positive

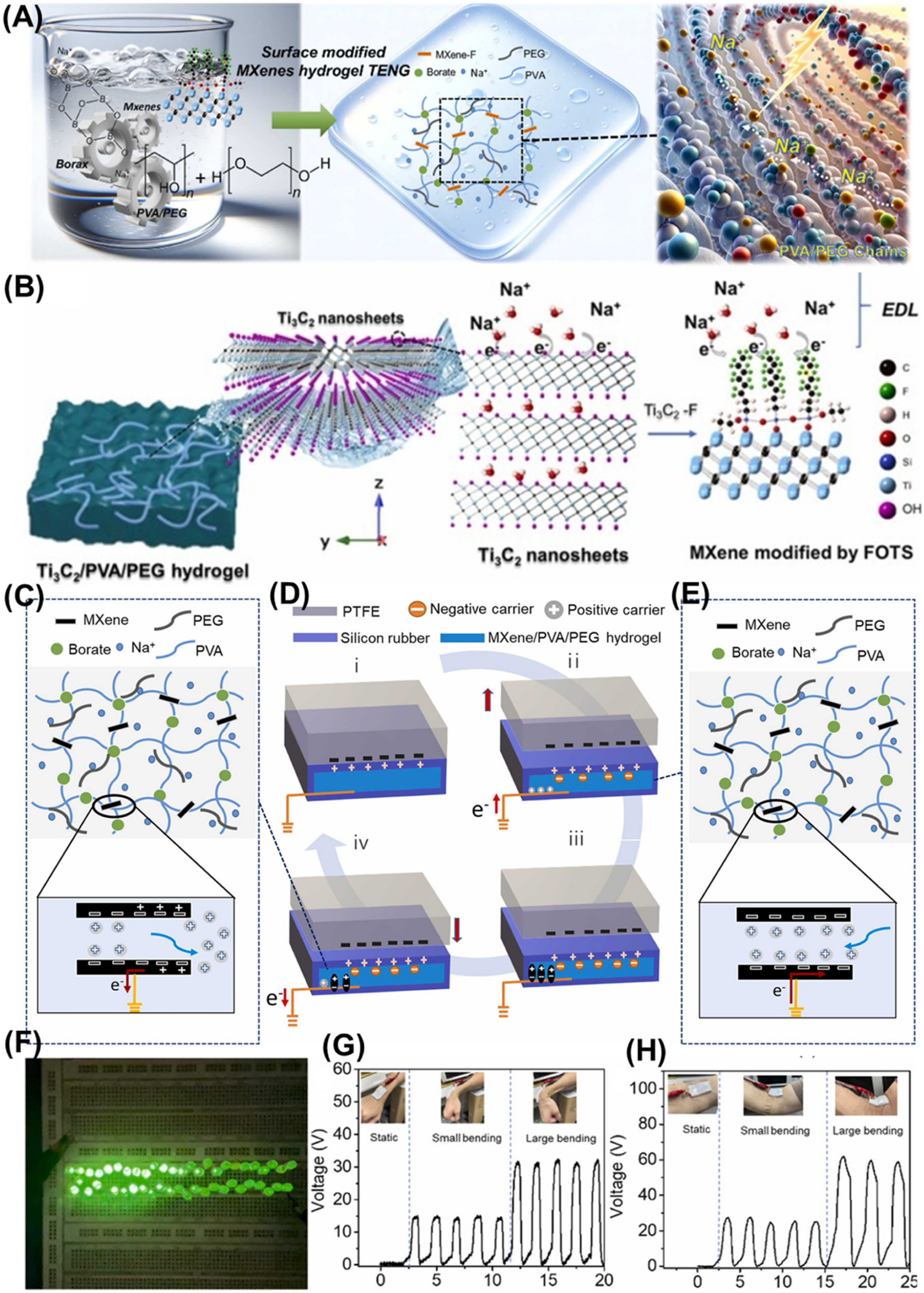

FIGURE 7 | (A) Schematic diagram of MXene nanosheets surface functionalization process within PVA-borax-PEG hydrogel utilized in TENGs. (B) Schematic illustration of electron transfer process occurring at the interface of water and Ti_3C_2 (electrical double layer). (C) 3D network structure illustration in the PVA-MXene-PEG hydrogel TENG and its mechanism, emphasizing MXene microchannels role. (D) The SVP mechanism demonstrates how the compressive stress convinces a positive flow of charges in Ti_3C_2 microchannel. (E) Demonstrating the influence of tensile stress, illustrating the positive charges flow out of Ti_3C_2 microchannel. (F) TENG glowing 51 LED under hand tapping. (G) Voltage observed when the TENG device bent downwards at various angles. (H) Voltage recorded when the TENG device bends upwardly with different angles. Reproduced with permission: Copyright 2024, Elsevier [116].

charges flow out of Ti_3C_2 microchannel. The F-MPPh and Cl-MPPh device exhibited 212 and 190 V voltages, respectively.

The overall distribution of electric potential increases substantially, according to theoretical calculations. As water molecules pass through the MXene nanosheets, this rise happens on both surfaces of them. The remarkably high sensitivity of the F-MPPh TENG to mechanical stimuli makes it a good candidate for incorporation into motion sensors intended to track human motions, such as the bending of wrists and elbows. With the fabricated TENG device, 51 LEDs have been grown under hand tapping, as shown in Figure 7F, and Figure 7G shows voltage attained when the TENG device is bent downwards at various angles. Figure 7H depicts the voltage recorded when the TENG device bends upward with different angles. Current research has focused on a hydrogel material based on 2D MXene, exploring the unique qualities of ionic slime TENGs to improve this TENG's streaming vibration potential mechanism. Through the streaming vibration potential mechanism, mechanical vibrations may be converted into electrical energy by the hydrogel's microchannels and fluid-filled capillaries [116].

By concurrently collecting the utilized mechanical power in two harvesters, hybridized of the two distinct mechanical harvesters of energy can offer a solution to this problem by improving the electrical efficiency of the energy harvester. The piezoelectric and triboelectric hybridized generator was created by Yun et al. [117] by the incorporation of MXene and barium titanate filler into polydimethylsiloxane (HGMBP). Through theoretical and practical investigation, the role of the MXene as a bifunctional conductive filler is explored. The ideal MXene concentration is determined, and a significant voltage of 80 V, current of 14 μA, and 13.5 W/m^2 power density are achieved. As an application, the finger joint motions of an actual hand with which the HGMBPs are connected are effectively used to operate a 3D printer-designed robot hand. Additionally, the k-mean clustering approach is used in the development of the object identification system, and excellent classification accuracy (93.33%) is achieved in the differentiation of various materials. These findings demonstrate the outstanding potential of the suggested HG-MBP as a material identification sensor and person gesture modulation system. It is anticipated that this technology will be used as the future e-skin in human–machine interfaces. Fluorine atoms have been successfully included as terminating groups in the MXene structure. Next, an experimental and theoretical analysis was conducted to determine how the presence of fluorine atoms in MXene contributed to the improvement of electrical power produced by the HG-MBP. The outcomes showed how MXene has great promise for use as a dual-functional filler that can both induce and trap charges. Furthermore, an object detection system and an actual human mobility manipulation system were created as applications because of the HGMBP's adaptability. The suggested HG-MBP had the ability to identify the stretching motions of actual fingers successfully, enabling the 3D-printed robot hand to mimic finger action. Additionally, the HGMBP's ability to be used as a substance identification device was exemplified. To extract the complementary effects of triboelectricity and piezoelectricity in a hybrid nanogenerator, we employed MXene as a dual-functional conducting filler in this study. Furthermore, it was confirmed that the device's great flexibility and sensitivity made it a viable candidate for use in material identification and motion detection for human modification systems [117]. Zong et al. [118] used PDMS-encapsulated CNF, and $Ti_3C_2T_x$ (MXene) aerogel film was used for designing flexible PENG devices with a substantial transforming energy capacity. This film can collect low-frequency motions to generate energy from human activity. Cellulosic dipole alignment is achieved by inducing a local polarization locking and optimizing the structural regularity of the CNF network through the usage of 2D MXene nanosheets. Basically, by preventing the more energy-intensive process of electrical poling to boost piezoelectricity, this approach enhanced the piezoelectric properties of cellulose. Additionally, the thin coating of PDMS gives the PENG exceptional flexibility and mechanical stability. In the meantime, it keeps MXene from oxidizing, which keeps it active. With a 10% weight percentage MXene, the optimized CNF/MXene/PENG produced 0.49 μA of current and 30.8 V of voltage. Wang et al. [119] reported on designing polydimethylsiloxane MXene/gelatin (PMMG) TENG with petal surface microstructures. Designed TENG has the advantages of simple preparation, high electrical output behavior, low cost, and environmental friendliness. The electrical output behavior of TENG may be greatly enhanced, with a current output increase of up to 139.7%, by doping 0.03 weight percent of MXene in the PDMS. To make PMMG-TENG, four distinct petals are utilized as the natural moulds. As compared to PMMG-TENG without structure, the results indicate that PMMG-TENG, having peony petal surface structure, offers superior electrical efficiency, with a current output increase of 228.17%. PMMG-TENG, having peony petal surface structure, displays exceptional electrical behavior, signifying maximum voltage (417.39 V), and maximum current (12.01 μA) with TENG device size of 3 cm × 3 cm, with 170 $\mu W/cm^2$ power density at 107 Ω load resistance. After 10,000 cycles, the PMMG-TENG's output performance is still in line with the starting state, demonstrating outstanding output stability. With ease, at least 100 LEDs may be turned on by the PMMG-TENG (3 V working voltage). At 75°C, gelatin film demonstrates remarkable degradation performance, requiring just 150 s to completely break down in water. In addition to its outstanding energy-collecting capabilities, PMMG-TENG offers a wide range of potential uses in the self-powered sensing space [119]. In various industries, including the chemical and agricultural sectors, the development of autonomous ethanol sensors is crucial in the Internet of Things (IoTs) era. He et al. [120] created a self-powered, trace-level, moisture-resistant gas sensor that can precisely measure the concentration of ethanol at ambient temperature. TENG-driven ethanol gas sensing system was fabricated by connecting TENG in series through interdigital electrodes coated with β-$Ni(OH)_2$ MXene composite. The NP-TENG generates an output power density of 482.9 mW/m^2 and 427.95 V (peak-to-peak) at room temperature and in a highly humid environment. This demonstrates the device's profuse self-powered capability to operate portable electronic devices, such as thermo-hygrometer sensors and LEDs, as well as to sense body movements, such as elbow bends and finger touches. Fabricated integrated ethanol sensor reveals a ~6.67 response, fast response (15 s), and recovery time (4 s), towards 100 ppm ethanol vapor at 87% of relative humidity and 26°C of room temperature. Additionally, the sensor has long-term stability, tremendous repeatability, and selectivity. This study addresses the need for low-powered, compact, and manageable sensors for IoT applications in industry and agriculture, while also expanding the application range of TENG for self-powered gas sensors [120]. Kim et al. [121] focused on the fabrication of an integrated tribo-piezo electric hybrid generator utilizing a simple approach. In this process MXene and tin diselenide ($SnSe_2$) are incorporated into PDMS as conductive fillers and piezoelectric materials, respectively. $SnSe_2$, a semiconductor of the n-type and piezoelectric, increases its work function and dielectric constant by improving the separation of charges and storage under mechanical pressure. This is due to the electron-donating property of Sn and the electronegativity of SE. Charge transport and dielectric characteristics are enhanced using MXene, a conductive filler that creates a conductive network. Fluorine has the strongest electron attraction, which further increases the work function of MXene produced using lithium fluoride. Additionally, by increasing electron mobility and conductivity inside the PDMS, these materials facilitate charge separation and boost induced charge creation, which greatly increases the nanogenerator's electrical output. The hypothesized piezoelectric characteristics of $SnSe_2$ help to produce extra piezoelectric charges when the hybrid generator is operating, which raises the electrical output. The enhanced electrical output from polling and the electrical output produced by the sandwich-structured hybrid nanogenerator, which reduced the triboelectric effect, serve as evidence for the piezoelectric characteristics of $SnSe_2$. With a load resistance of 50 MΩ, the hybrid nanogenerator reaches a maximum power density of $19.77\,W/m^2$ and 202.31 V and 108.55 μA. The hybrid nanogenerator's use in speed detection and vehicle speed measurement is proven. The hybrid nanogenerator-based system and an industrial radar module are used to measure vehicle speeds. The results show that the speeds detected by these two approaches have a remarkable accuracy, with less than 10% error. When a car passes by, the hybrid nanogenerator's power is captured by a power regulation integrated circuit, which is then utilized to power the alarm component when speed is detected. These outcomes demonstrate the hybrid nanogenerator's potential for a range of self-powered technologies [121]. Zhang et al. [122] designed conformally adhesive, highly stretchable, and self-healing hydrogel for strain-sensing applications. Many studies have been conducted on conductive hydrogels for monitoring human mobility and health. However, hydrogels' inability to adhere well to skin interferes with their ability to monitor in real-time while minimizing signal loss. This study uses hydrogels made of acrylic acid (AA), sulfobetaine methacrylate (SBMA), cellulose nanofibers (CNFs), and AA–N-hydrosuccinimide ester (AA–NHS). In the presence of initiators were gelled within a few minutes after including $Ti_3C_2T_x$ as a flexible and versatile crosslinking agent. SBMA and AA copolymerized to create the hydrogel chief network structure, and the incorporated CNF progressed the hydrogel tensile strain (1737%–2240%). With a total adhesion strength of 11.6 kPa, the hydrogels conformally attached to porcine skin by the action of ester bonds induced by NHS and the zwitterionic adhesion mechanism. The hydrogel sensors demonstrated rapid response (95 ms) and excellent sensitivity (4.98-gauge factor) when combined as strain sensors. After that, the hydrogel was put together to serve as an electrode in the TENG for self-powered sensing and mechanical energy harvesting. The TENG had strong electrical output characteristics and had the ability to use the mechanical energy gained from walking to charge commercial capacitors [122]. Xu et al. [123] effectively decorated commercialized melamine foam with 1D AgNWs and 2D MXene by employing a straightforward vacuum-assisted dip-coating technique. The manufacturing cycle was relatively quick, the composite foams were prepared in an easy-to-green manner, and repeatability and scalability were guaranteed. The resulting composite foam, which combined energy generation, EMI shielding, and temperature management capabilities into one, showed great conductivity for electricity and low-density thanks to its special porous construction and multiscale linked frame. With continual double conductive networks, the multiple scales composite foam demonstrated an exceptional 48.32 dB EMI shielding performance. Furthermore, the composite foam's surface sustained a steady-state temperature of 90.8°C at a relatively small voltage of 0.8 V, demonstrating an impressive Joule heating capacity. It's interesting to note that the bigger size's steady-state temperature for the composite foam at 0.9 V was determined to be 106°C, the same as the smaller sizes. Notably, the ultra-thin Ecoflex film-deposited conductive composite foam worked well as the single electrode TENG's negative electrode. The findings of simulations and experiments both demonstrated its remarkable ability to gather energy. Additional research was conducted on this foam-based TENG to monitor human activity, light up light-emitting bulbs, and charge commercial capacitors. Jiang et al. [124] create hydrogels with surfaces containing randomly spread micro-spines by mixing acrylamide (AM) and sodium alginate (SA) as the hydrogel's constituents. An extremely conducting MXene layer is printed *via* inkjet onto the hydrogel microspines' surface to create a wearable sensor. The resultant sensor has impressive features such as $15.03\,kPa^{-1}$ of sensitivity, 10 Pa LOD, 0.12–70 kPa of operating range, fast response, quick recovery, reliable performance (more than 1000 cycles), and exceptional resistance to low temperatures. Furthermore, even while operating at −20°C and in an ice bath, this hydrogel-based sensor makes it easier to efficiently gather human tracking data, such as voice patterns, joint, and pulse motions. The ability to construct surface-based inkjet MXene hydrogels that are into a deformable TENG is significant because it permits mechanical energy collection. The TENG displayed 5 V and 2.5 μA. Remarkably, it functioned dependably in an ice bath and at −20°C. After naturally rehydrating for 48 h after dehydration, most of its functioning was restored. The exceptional energy harvesting and signal output potentials of the sensor determine their probable applications in biomonitoring, personal healthcare, wearable electronics, and future-generation artificial skin [124]. Unique and exceptional properties such as electrical conductivity, surface functionalization, high specific surface area, tunable work function, mechanical flexibility, hydrophilicity, high dielectric constant, composites synergistic effects, chemical stability, and energy generation capability of MXene-based materials make them ideal materials for enhancing the energy harvesting behaviors of the TENG. Comparison of MXenes-based TENG devices output performance has been shown in Table 3.

TABLE 3 | Comparison of MXenes based TENG devices output performance.

S. No	Positive material	Negative material	Voltage	Current	Power density	References
1	PAN and ZIF-67	PVDF/MXene	305 V	10.6 µA	10.9 W/m^2	[108]
2	Glass	PDMS and chitin nanocrystals/MXene	56 V	3.1 µA	99.5 mW/m^2	[115]
3	PVA/MXene	PVDF	1056 V	36.6 µA	—	[109]
4	MXene/PVA/PEG hydrogel	PTFE	212 V	0.9 µA	3 mW/m^2	[116]
5	PVA	PTFE	—	31.91 µA	194.37 µC/m^2	[113]
6	MXene-alginate	FEP	670 V	15 µA	0.28 W/m^2	[114]
7	Silk fibroin@MXene	PDMS	545 V	16.12 µA	13.25 W/m^2	[111]
8	PA66	MXene/Silicone	1160 V	40 µA	17.04 mW	[110]
9	Melamine foam@ MXene/AgNW	PVDF	115 V	0.9 µA	514.2 mW/m^2	[123]
10	Sodium alginate SAEL hydrogels	PET	5 V	2.5 µA	—	[124]
11	PAS/CNF/MXene hydrogel	—	143 V	10 µA	—	[122]
12	Al	PDMS/BaTiO$_3$@MXene	80 V	14 µA	13.5 W/m^2	[117]
13	Cu	β-Ni(OH)$_2$@PVDF	427.95 V	10.9 µA	482.9 mW/m^2	[120]
14	Al	SnSe$_2$ and MXene@PDMS	202.31 V	108.55 µA	19.77 W/m^2	[121]
15	Gelatin	PDMS-MXene	417.39 V	12.01 µA	170 µW/cm^2	[119]
16	Silicone rubber	MoS$_2$/MXene/CA	140 V	—	2975 mW/cm^2	[112]

2.4 | MXene for Electrochemical Sensing

MXenes and its derived composite materials have materialized as prospecting candidates for the construction of electrode materials in electrochemical sensing applications. The characteristics and uses of MXenes with metallic components are well recognized. Several doping techniques using different materials are also being investigated to improve the properties and functionality of MXenes. These nanoparticles have promising ion transport capabilities, excellent electrical conductivity, a specific large surface area, adaptability to surface functionalization, and tuneable interlayer spacing. The tremendous progress made in the design and development of innovative nanomaterials and nanocomposites has enabled the synthesis of unique nanostructures for a wide variety of applications. Increased performance, selectivity, and sensitivity can be achieved more easily with the use of functionalized nanomaterials with customized characteristics [125–128]. 2D materials contain fine atomic arrangements with lateral dimensions from a few nm to µm. These materials are highly suitable for producing environmental remediation sensors, adsorbents, membranes, and photocatalysts due to their abundant surface atoms and high surface area. MXenes are a relatively recent category of nanomaterials with two dimensions that have the potential to be applied to the development of extremely effective and long-lasting environmental applications. The exceptional metallic conductivity, excessive volumetric capacity, exceptional mechanical and electrical properties, and versatility to create very sensitive (bio)sensors have all drawn significant interest in 2D transition-metal carbide/nitride layered materials for electrochemical sensing. It has been demonstrated that adding nanoparticles to a (bio) sensor can improve its detection capabilities even further [129–132]. The usage of nanomaterials as sensing materials in electrochemical (bio)sensing offers various advantages like high carrier mobility, surface area to volume ratio, excellent mechanical strength, and thermal conductivity. Electrochemical sensing strategies are of notable interest to researchers and technologists worldwide owing to their cost-effectiveness, short response time, ease of handling, excellent sensitivity, and miniaturization. Numerous methods are available for sensitively detecting distinct target analytes at varying concentrations by electrochemical characterization. Electrochemical methods have attained massive attention owing to their quick response, low cost, high sensitivity, and so forth. Over the past decades, several electrochemical sensing approaches have been widely developed for the detection of various contaminants. Electrochemical approaches employ the connection between electricity and chemistry by profiling the output signals (e.g., current, potential, phase, charge, frequency, etc.) produced by chemical processes that usually occur at the electrolyte and electrode interface. Chief sensing techniques utilized for the electrochemical analysis are potentiometry, differential pulse anodic stripping voltammetry, impedimetry, amperometry, linear sweep voltammetry, voltammetry, conductometry, cyclic voltammetry, differential pulse voltammetry, square wave anodic stripping voltammetry, and anodic stripping voltammetry. The features of the working electrode have a significant impact on the efficacy of electrochemical detection. The working electrode can be chemically or biologically modified with electron mediators to increase the sensitivity and selectivity of a sensor and guarantee site-specific detection of the target analyte. Nanomaterials hold great promise for this application because of their beneficial quantum mechanical properties and huge specific surface area [130, 131, 133]. The design and development of sophisticated sensing strategies have been made easier by recent developments in nanotechnology and created new pathways for the synthesis of 2D materials and their composites. MXenes and MXene-based composites have been used widely in electrochemical sensing applications [125, 130–132, 134]. Liao et al. [135] synthesized nitrogen-doped MXene porous carbon composite through the nucleation and the ZIF-8 MOF conversion on the 2D hierarchical Ti_3C_2 MXene nanosheets. With insertion of ZIF-8 MOF, Ti_3C_2 nanosheets restacking was efficiently avoided, consequently the electrochemical properties of the material improved significantly. Prepared N-doped-Ti_3C_2 porous carbon composite was used for the simultaneous electrochemical sensing of 4-aminophenol and acetaminophen. Obtained findings suggest that the as-fabricated sensor possesses exceptional electrochemical activity for the 4-aminophenol and acetaminophen, which was ascribed to synergistic influence of porous carbon N- and Ti_3C_2 that accelerates the transfer of electrons on the surface of the electrode. Obtained findings demonstrated the high electrocatalytic activity of the as-fabricated electrochemical sensor for acetaminophen and 4-aminophenol, which was ascribed to the synergistic actions of PC and nitrogen-doped MXene, which accelerated the transfer of electrons on the surface of the electrode. Under the optimized electrochemical conditions, the linear detection range for the acetaminophen and 4-aminophenol was 1–150 μM. The limit of detections for the acetaminophen and 4-aminophenol were found to be 0.050 and 0.059 μM (signal-to-noise ratios = 3) respectively. Moreover, the nitrogen doped MXene porous carbon composite electrochemical sensor was used to determine acetaminophen and 4-aminophenol in paracetamol tablets and industrial wastewater, and adequate recoveries have been obtained [135]. Recently, 3D porous laser-scribed graphene (LSG) is being used as a probable electrode material for the fabrication of flexible electrochemical sensing applications owing to its low cost and high efficiency. Nevertheless, the growing of nanoparticles typically depends on reducing agents and conditions, which restricts their application in the fabrication of flexible biosensors. To solve this issue, Wang et al. [136] used MXene nanosheets to functionalize 3D LSG sheets with a C─O─Ti covalent crosslink to prepare an MXene-LSG hybrid scaffold. To improve LSG-MXene's catalytic efficiency, shape-controlled gold-palladium bimetallic nanoparticles were created on its surface using a self-reduction technique that took 6 min at ambient temperature. The resulting hybrid nanocomposite was utilized to assess uric acid (8–100, 200–800 μM), dopamine (12–240 μM), and ascorbic acid (10–1600 μM). The designed sensor showed LOD of 1.47 μM for uric acid, 3 μM for ascorbic acid, and 0.13 μM for dopamine. Moreover, Au-Pd/MXene-LSG was effectively applied to assess ascorbic acid, uric acid, and dopamine in urine samples. Vertically aligned MXene-LSG hybrid scaffold exhibits exceptional electrochemical characteristics and durability, in addition to offering an exceptionally large specific surface area for electrochemical processes. The predicted synergistic signal amplification from the combination of gold and palladium nanoparticles makes the suggested sensing device a viable option for the noninvasive continuous detection of biomarkers in human fluids [136]. Elumalai et al. [137] utilized an ultrasonicated solution processing-based galvanic deposition technique to deposit AuNPs on the delaminated $Ti_3C_2T_x$ nanosheets. AuNP@$Ti_3C_2T_x$ nanocomposite was placed on the GCE and applied for label-free and simultaneous electrochemical recognition of the uric acid and the folic acid at the physiological pH. Altered GCE has a fascinating figure of merits, folic acid and uric acid working potentials well separated (+ 0.70 V and + 0.35 V vs. Ag|AgCl), and 0.03–1520 μM wide linear response for uric acid. 0.02–3580 μM linear response for folic acid. Appreciable electrochemical sensitivities for folic acid and uric acid (0.494 and 0.53 $\mu A/(\mu M\cdot cm^2)$) and 11.5 nM of LOD for uric acid and 6.20 nM of LOD for folic acid. AuNP-$Ti_3C_2T_x$ nanocomposite electrode displayed good repeatability, acceptable reproducibility, and excellent stability. The strategy was used to examine spiked serum samples, and the modified GCE has displayed substantial recoveries for uric acid (97.1%–98.8%) and folic acid (96.8%–98.0%) [137].

Chen et al. [138] used $Ti_3C_2T_x$ MXene and nitrogen-doped rGO composite (MXene-N-rGO) as the electrode material to fabricate an electrochemical sensor to detect adrenaline. Nanocomposite was prepared through a single step hydrothermal approach using ethylenediamine as the reducing agent and nitrogen source. Nitrogen-doped in the rGO served as the bridge between rGO and MXene through tight hydrogen bonds. SEM images revealed that the N-rGO surface had a considerable number of MXenes with accordion-like morphology. MXene/N-rGO composite demonstrated a synergetic catalytic activity for adrenaline oxidation, which resulted from N-rGO's unique catalytic activity and MXene's wide surface area and good conductivity. These properties of nanocomposite have a notable influence on the amplification of the signal for adrenaline detection, with 10.0 nM to 90.0 μM of linear range and 3.0 nM LOD. Fabricated MXene-N-rGO modified electrodes demonstrated repeatability, appreciable stability, and good reproducibility. Furthermore, the proposed sensor was effectively used for the voltametric detection of adrenaline in urine (97.75% to 103.0% of recovery) [138]. Prussian blue (PB) has enzyme mimic properties due to its propensity for reactive oxygen species (ROS) radicals. Because of this enzyme mimic property, it is beneficial and promising to imagine the use of PB for target analytes sensing. In this instance, Mohan et al. [139] proposed electrodeposition of PB on the Nb_2CT_x MXene modified carbon cloth for the nonenzymatic hydrogen peroxide electrochemical detection. Nb_2CT_x was dropped on carbon cloth followed by electrochemical deposition of PB utilizing chronoamperometry (0.7 V). The underlying surface of Nb_2CT_x was found to have homogeneous PB coverage. The electrochemical deposition time was adjusted by altering the amount of deposition (240, 360s, 480s, and 600s), and the material formed after 480 s was shown to have higher sensing qualities for hydrogen peroxide detection. The Nb_2CT_x-PB480 modified carbon cloth was competent to detect hydrogen peroxide linearly (1–10 and 10–100 μM)

200 nM of LOD. Moreover, the designed sensor was able to exhibit good selectivity to hydrogen peroxide even in presence of the interfering molecules like ascorbic acid, sodium chloride, uric acid, and dopamine. Furthermore, the material demonstrated good storage stability, as seen by 97% of retention activity even after 1 week of storage. PB and MXene composite possess significant potential for being utilized as a selective and sensitive sensing element for hydrogen peroxide electrochemical detection [139]. Yang et al. [140] developed TiO_2@MXene heterostructures with oxygen-rich vacancy defects to fabricate electrocatalysts to detect imidacloprid. TiO_2 nanoparticles were produced in situ on MXene and employed as scaffolding to prevent MXene nanosheet stacking. The resulting TiO_2@ MXene heterostructure has a good, layered structure and a large specific surface area. Following that, electrochemical activation is used to treat TiO_2@MXene, boosting the amount of surface oxygen vacancies and significantly improving the composite's conductivity and adsorption capacity. As a result, the produced VOTiO_2@MXene shows high electrocatalytic activity in the imidacloprid electrochemical reduction. Under the ideal conditions, CV and LSV techniques were used to evaluate imidacloprid's electrochemical behavior at the VO-TiO_2@MXene/GCE. Fabricated VO-TiO_2@MXene sensor presented an apparent reduction peak (−0.05 V) with 0.07–10.0 μM and 10.0–70.0 μM linear ranges with 23.3 nM LOD. The sensor accurately detects imidacloprid in vegetable and fruit samples, with a recovery rate of 97.9%–103% and an RSD of less than 4.3% [140]. Thukkaram et al. [141] focused on the fabrication of $Ti_3C_2T_x$ and V_2O_5-modified GCE. Electrochemical analysis for bisphenol A detection was conducted using $Ti_3C_2T_x$-V_2O_5 GCE, and bisphenol A electrochemical oxidation was investigated using differential pulse voltammetry, electrochemical impedance spectroscopy, and cyclic voltammetry electrochemical strategy. The voltammetric response of material for the detection of bisphenol A in various concentrations has been investigated. DPV exhibited 414–31.2 μM linear range with 87 nM LOD detection limit for bisphenol A. Fabricated bisphenol A sensor produced satisfactory findings and had the potential to become a valuable platform in an environmental monitoring system [141]. Chen et al. [142] designed a distinctive screen-printed carbon electrode modified with 3D melamine-doped graphene oxide (GO)-MXene composite aerogel for the sensitive and simultaneous identification of Pb^{2+}, Cd^{2+}, and Zn^{2+} metal ions in the environment. A self-assembly approach was employed to create 3D MXene aerogels from MXene, melamine, and GO. Particularly, the 3D network-like structure formed with the combination of 2D MXene and rGO sheets can give a high surface area ratio and enhanced functional clusters, which will be useful in increasing electrical conductivity and promoting heavy metal ion uptake. In the 3–900 μg/L linear range, the designed sensing strategy can sensitively and simultaneously detect Pb^{2+}, Cd^{2+}, and Zn^{2+}, with LODs of 0.29, 0.45, and 0.48 μg/L, respectively. This study demonstrates reliability and precision in the identification of Yangtze River, Minzhu Lake, tap water samples, and rice, wheat, corn, and sorghum cereal samples and proposes a new technique for monitoring heavy metal ions in the natural environment [142].

MIPs, unlike other molecular identification elements, are used in a wide variety of fields because of their characteristic features. Nonetheless, most of the MIPs were developed using poor or nonconducting materials, which substantially hinders the electron transfer rate and decreases sensitivity detection. To successfully improve the sensitivity of MIPs based electrochemical sensors, composite electrochemical sensors have been constructed using innovative conductive materials such as graphene, multiwalled carbon nanotubes (CNTs), and MOF materials. MXene has sparked great interest among conductive materials due to its unique physical, mechanical, and structural qualities that are equivalent to or even superior to graphene. Shi et al. [143] proposed the fabrication of a molecularly imprinted electrochemical sensor using MXene fibers. First, the wet spinning approach produced MXene fibers with a high aspect ratio, allowing sheets like MXene to be uniformly organized, preventing MXene agglomeration and enhancing electrical conductivity. Afterward, MIPs with specific spots for recognition were created on the MXene fibers surface utilizing the electro polymerization technique. The electrochemical sensor took advantage of molecular imprinting technology and fibers of MXene to achieve high hydrocortisone sensitivity and selectivity. The designed electrochemical sensor exploited the advantages of molecular imprinting strategies and MXene fibers to gain improved hydrocortisone sensitivity and selectivity. Electrochemical analysis with 0.5 nM to 10.0 μM hydrocortisone concentrations under optimized experimental conditions demonstrated exceptional linearity and LOD (0.17 nM). Moreover, the electrochemical sensor demonstrated interference resistance, superior selectivity, repeatability, stability, and serum application performance [143]. There is a high need for electrochemical sensors that can detect neurochemicals like dopamine without the use of reagents. Paul et al. [144] synthesized a nanocomposite from the nonconductive MOF and Ti_3C_2-based MXene as the conductive probe for the voltametric sensing of dopamine. Modified MOF-Ti_3C_2 GCE was utilized for the detection of dopamine in the presence of 5-aminovaleric acid and ascorbic acid. MOF-Ti_3C_2 GCE demonstrated 110 nM of detection limit for the detection dopamine in 90–300 nM linear concentration range [144]. Noninvasive wearable sensors provide continuous glucose testing in sweat for diabetes management and treatment. Nevertheless, glucose catalytic and sweat sample processes pose problems in facilitating the creation of effective wearable glucose sensors. Li et al. [145] reported on the fabrication of wearable and flexible nonenzymatic sensor for the continuous detection of glucose in sweat. Synthesized Pt-MXene electrocatalyst by Pt nanoparticles hybridization onto $Ti_3C_2T_x$ MXene nanosheets with 0–8 mmol/L linear range for the glucose sensing under neutral conditions. Furthermore, the sensor's structure was improved with the immobilization of Pt-MXene in the conductive hydrogel to improve the sensor stability. Based on the optimized Pt-MXene, a wearable flexible glucose sensor was fabricated by using a microfluidic patch for the collection of sweat onto the flexible sensor. The sensor's usability for detecting glucose in sweat was evaluated, and the sensor was able to detect glucose changes in response to the body's replacement and utilization of energy, with a similar pattern observed in the blood. An in vivo glucose assay in sweat revealed that a manufactured sensor has the potential to measure glucose continuously, which is critical for diabetes treatment and control [145]. 5-Hydroxytryptamine is an essential neurotransmitter, and its presence in the body has considerable implications for human health. Chen et al. [146] designed a triangular-AgNP-L-cystiene-MXene electrocatalyst for the detection of 5-hydroxytryptamine. L-cysteine, an electrically active amino acid with a sulfhydryl group, creates a highly stable S─Ag bond with AgNPs, allowing it to substitute trisodium citrate (TSC) selectively in the TSC-capped triangular Ag nanoplates. Owing to biocompatibility, good conductivity, and substantial surface area, MXenes offer a decent sensing platform for Tri-AgNP/L-Cys loading. The sensor detected 5-hydroxytryptamine at concentrations ranging from 0.5–150 μM, with 0.08 μM LOD (S/N = 3). For 5-hydroxytryptamine sensing in serum samples, the sensor showed a 95.4%–102.3% recovery rate [146]. Homogeneous electrocatalytic sensors frequently have drawbacks of low signal-to-noise ratio, high signal background, and false positive results owing to pre-addition of electroactive materials. To overcome these limitations, novel homogenous electrochemical sensors that utilize in situ electroactive substance production are required, which is currently underexplored. Yu et al. [147] developed 2D nanozymes (cobalt-doped 2D MXene nanosheets [CMNSs]) with exceptional peroxidase properties. The designed material was used to fabricate electrochemical sensors based on the in-situ formation of electroactive substances to detect pesticides. 2D CMNSs were produced using a template-directed wet chemical technique and showed remarkable hydrophilia and water dispersibility, allowing them to catalyze o-phenylenediamine oxidation, resulting in a considerably higher reduction current. The development of homogeneous electrochemical sensors for organophosphate pesticides was made possible by 2D CMNSs with peroxidase-like properties, which showed a distinct response to the thiol compounds. These sensors were based on acetylthiocholine thiocholine hydrolysis, which was catalyzed by acetylcholinesterase, and the inhibition of acetylcholinesterase activity by organophosphate pesticides. In the examination of pakchoi extract solutions, the recovery for pesticides varied between 97.4% and 103.3%. The homogeneous electrochemical sensor that has been suggested, which is based on the in-situ synthesis of electroactive chemicals, will open up new avenues for the creation of substantial electrochemical sensors and show promise in the detection of pesticide residues in actual samples [147].

Gao et al. [148] developed a coral reef-like platinum-decorated MXene nano composite for the fabrication of sensitive platinum/MXene/GCE to accurately detect quercetin. MXene multilayer structure provides enough active sites for the electrochemical process and enhances electron transport, resulting in a decrease in the electrochemical impedance. Quercetin electrochemical behavior on platinum/MXene/GCE uncovers that the electrochemical redox procedure involves the involvement of two-electron or double proton reaction procedure. As ascertained, the platinum/MXene-GCE demonstrates exceptional stability, selectivity, repeatability, and reproducibility and indicates accurate recognition ability in real-time practical application. Furthermore, the platinum/MXene-GCE electrode has a low limit of detection and excellent sensitivity, which is superior to most prior findings. This study presents a promising technique for selective quercetin electrochemical detection, which could guide the advancement of the highly selective sensor with exceptional sensitivity [148]. Chavan et al. [149] demonstrated an ultrasensitive molecule structure for dopamine sensing in neuro-molecules utilizing $Ti_3C_2T_x$-MXene multilayer materials. It was synthesized using the in situ 4-aminophenyl boronic acid polymerization with an adaptable “two-step” technique. Figure 8A–C depicts the step-by-step schematic illustration of $Ti_3C_2T_x$/4-APBA alteration of SPC-electrode for dopamine detection. Figure 8A shows the picture of $Ti_3C_2T_x$ powder after dispersing the solution in a glass vial and its atomic structure. Figure 8B shows $Ti_3C_2T_x$ multilayered arrangements. Figure 8C depicts the fabrication process of the SPC electrode. Furthermore, its on-site use was obtained by designing the label-free SPCE for electrochemical monitoring of dopamine levels in human serum and buffer samples at point-of-care level analysis. Significantly, the excellent specificity of the $Ti_3C_2T_x$-4 aminophenyl boronic acid alteration for SPCE electrochemical measurement allows for easy implementation with minimal signal drift. Figure 8D exemplifies the DPV profiles of relative differences in current profiles after binding with different dopamine concentrations to the NHS-FC signaling probe on a modified electrode. Figure 8E represents the calibration profile plotted for the detection of dopamine based on DPV electrochemical analysis for subsequent SPCE. As proof of concept, this innovative electrochemical sensor was discovered to be conceptually inexpensive and simple. The Designed sensor selectively measured dopamine levels with 1.3 nM LOD (PBS buffer) and 1.9 nM (human serum sample). The sensor has a 40–500 nM linear detection range for dopamine concentrations with 0.0134 μA/nM of sensitivity [149].

Currently, people's mental and physical health is deteriorating because of increased stress and an unhealthy lifestyle. Cortisol, a crucial hormone responsible for the correct functioning of the human system, regulates physiological functions. Furthermore, cortisol can be used to measure psychological stress. Designing sensors for the detection of cortisol has enormous potential because they not only allow for prompt modifications, treatments, and adjustments by sensing the uncharacteristic physiological indicators, nevertheless they also provide comprehensive data to investigate on the relationship between cortisol and a variety of probable diseases. Liu et al. [150] reported on the fabrication of MIP electrochemical (bio)sensor that uses a porous nanocomposite-modified electrode for cortisol detection. Nanocomposite is synthesized by mixing graphene and $Ti_3C_2T_x$ sheets. Nanocomposite material with high electroactive surface area and elevated conductive properties promotes the transfer of charges ability on the electrode surface, increases the sensor's operative surface area and improves the cortisol engraved cavities content on the electrode, thus enhancing the detection capability of the sensor. By improving the fabrication process, the sensor has low LOD (0.4 fM), a wide range of detection (1 fM–10 μM), and strong specificity for the steroid hormones and interfering compounds with comparable cortisol structures [150]. Dipyridamole electrochemical detection is highly important since it is extensively utilized for the treatment of cardiovascular illnesses and to impart inhibitory effects for cancer patients. Ankitha et al. [151] reported on the fabrication of MXene and ReS_2 (ReS_2─Nb_2CT_x) composite using a hydrothermal approach. Nb_2CT_x was found to be partly oxidized, and ReS_2 nanoparticles were scattered on its surface during hydrothermal synthesis. ReS_2-Nb_2CT_x was utilized to alter carbon cloth electrodes to detect dipyridamole electrochemically. The ReS_2 ratio in the

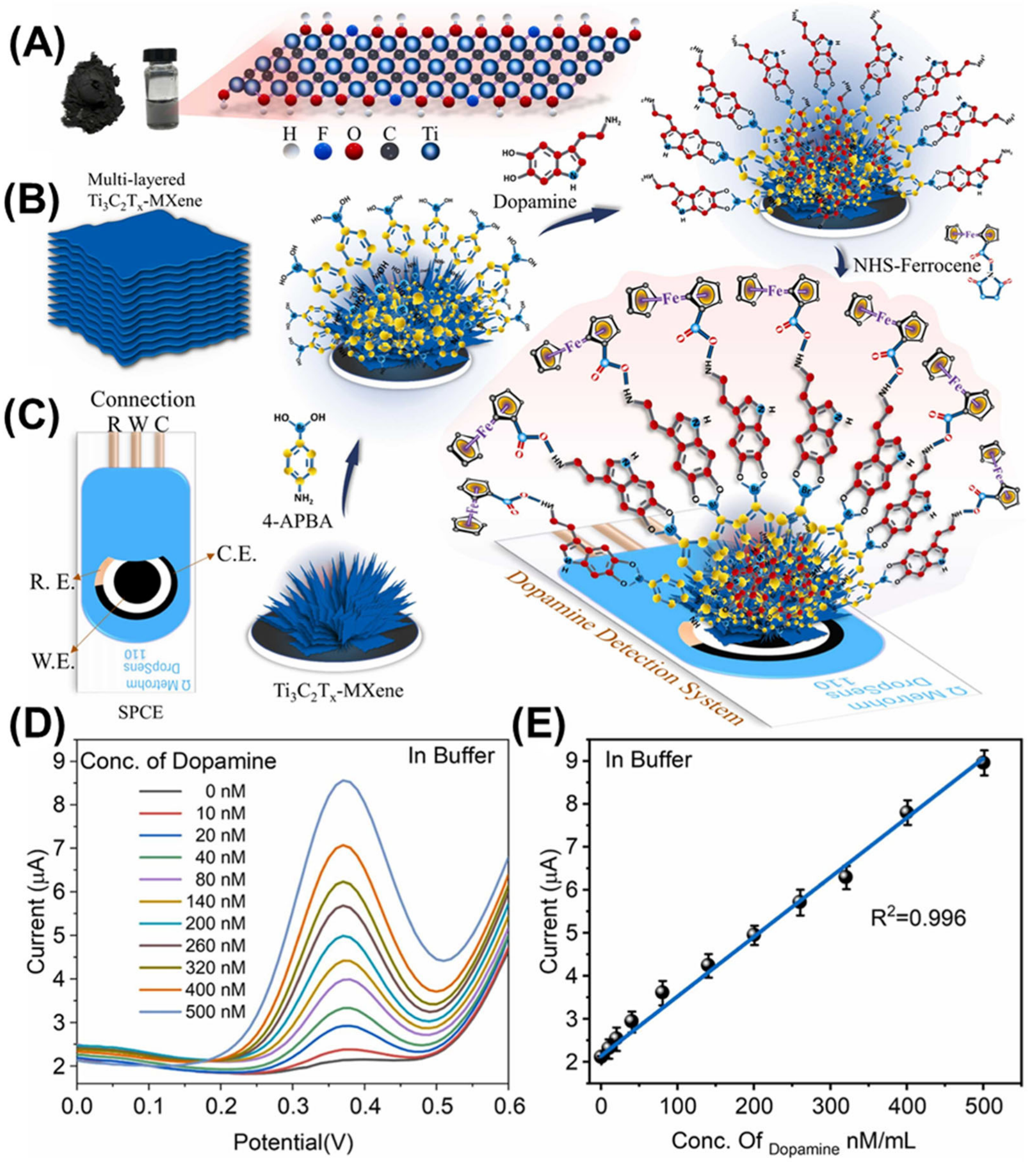

FIGURE 8 | Step-by-step schematic illustration $Ti_3C_2T_x$-4 APBA alteration of SPCE for dopamine detection. (A) Picture of $Ti_3C_2T_x$ powder after dispersing the solution in a glass vial. (B) $Ti_3C_2T_x$ multilayered arrangements. (C) Fabrication process of SPCE. (D) DPV profiles of relative differences in current profiles after binding of different dopamine concentrations to the NHS-FC signaling probe on the modified electrode. (E) Calibration profile plotted for the detection of dopamine on the basis of DPV electrochemical analysis for subsequent SPCE. Reproduced with permission: Copyright 2024, Elsevier [149].

composite was improved by altering the atomic ratio from 4 to 9, and ReS_2-Nb_2CT_x demonstrated the best sensing capabilities due to optimal interaction between ReS_2 and Nb_2CT_x. The sensor detected dipyridamole linearly from 100 pM to 1 μM, with 28 pM LOD. In the presence of various interferents, the modified electrode demonstrated great selectivity for dipyridamole, as well as repeatability and stability. Furthermore, the proposed sensor was employed to detect dipyridamole in the human serum samples [151]. Catechol (CC) and hydroquinone (HQ) are the two primary dihydroxybenzene isomers. These are hazardous contaminants found in wastewater that frequently mix and interfere with sample identification. For practical analysis and concurrent identification of catechol and hydroquinone in wastewater, Ranjith et al. [152] fabricated a hybrid electrochemical sensor using electrospun 1D $MnMoO_4$ nanofibers and a few-layered exfoliated 2D MXene. 2D MXene and 1D $MnMoO_4$ nanoarchitecture facilitated abundant defective edges, synergistically enhanced the influence of signal amplification and demonstrated superior electrochemical activity towards catechol and hydroquinone oxidation. Figure 9A represents the synthesis procedure of 1D/2D $MnMoO_4$-MXene hybrid nanocomposite sensor for simultaneous detection of catechol and hydroquinone. MXene-$MnMoO_4$-GCE displayed 0.102 V (hydroquinone) and 0.203 V (catechol) oxidation potentials. It showed the simultaneous and distinguished detection range (0.101 V) with a high anodic peak current. Figure 9B shows the DPV profiles of MXene-$MnMoO_4$ composite GCE in the 0.05 M PBS with different hydroquinone concentrations (5–68 nM) and constant (25 nM) catechol concentration and its corresponding calibration graph (Figure 9C). Figure 9D shows the DPV profiles of MXene-$MnMoO_4$ composite GCE in the 0.05 M PBS with different catechol

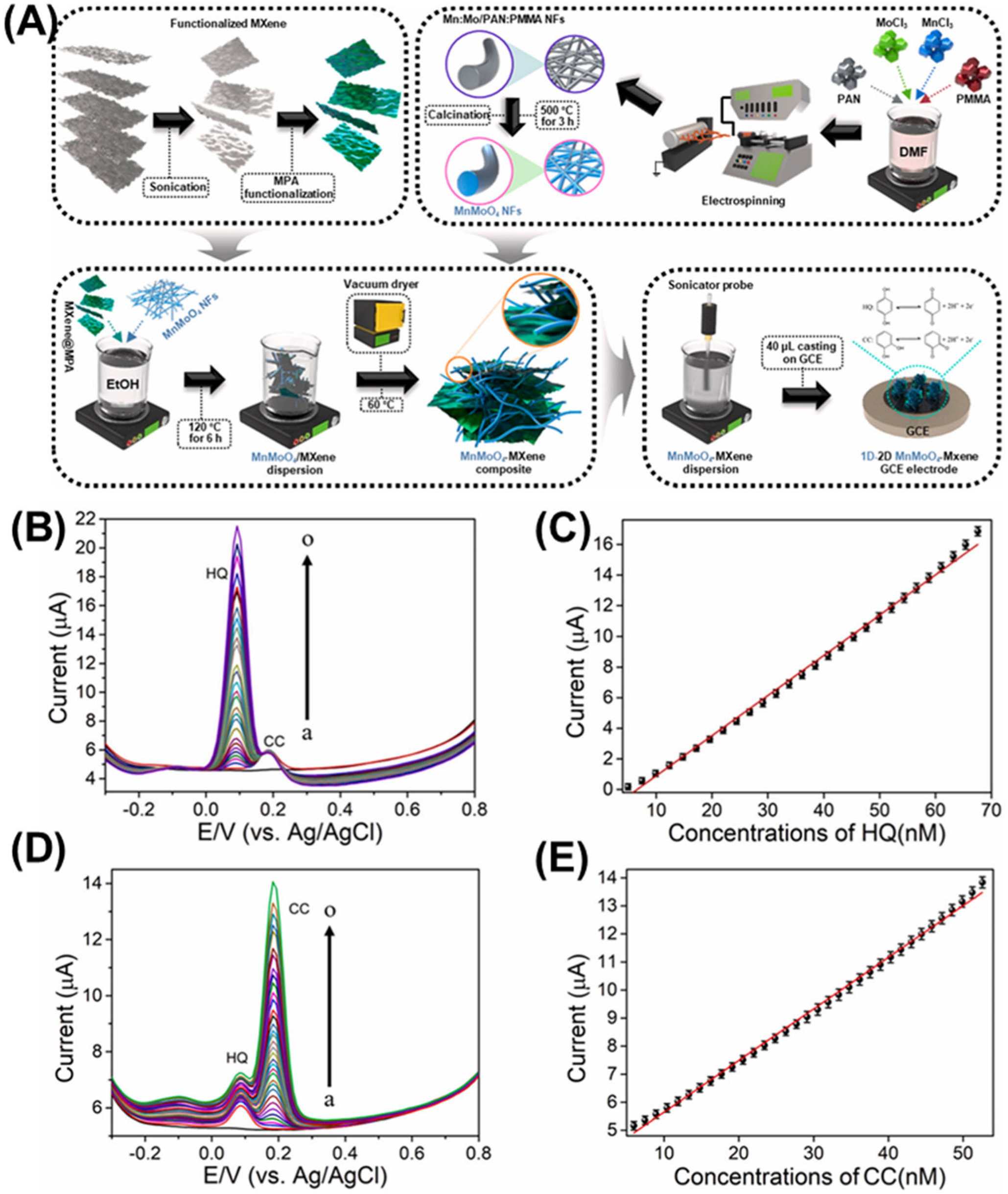

FIGURE 9 | (A) Representation of the 1D–2D $MnMoO_4$-MXene nanocomposite sensor synthesis for the simultaneous detection of catechol and hydroquinone. (B) DPV profiles of MXene-$MnMoO_4$ composite GCE in PBS buffer (0.05 M) with different hydroquinone concentrations (5–68 nM) and constant (25 nM) catechol concentration and its (C) corresponding calibration graph. (D) DPV profiles of MXene-$MnMoO_4$ composite GCE in PBS buffer (0.05 M) with different catechol concentrations (6–53 nM) and constant (25 nM) hydroquinone concentration and its (E) corresponding calibration graph. Reproduced with permission: Copyright 2022, Elsevier [152].

concentrations (6–53 nM) and constant (25 nM) hydroquinone concentration and its corresponding calibration graph (Figure 9E). Noteworthily, the fabricated 1D–2D hybridized sensor presented 5–65 nM wide linear response from for the catechol and hydroquinone. Prepared sensor has shown 0.26 nM LOD for the hydroquinone and 0.30 nM LOD for catechol with great stability. The realistic 1D–2D nanocomposite-based sensor efficiently identified catechol and hydroquinone in water utilizing the differential pulse voltametric technique [152].

Ranjith et al. [153] synthesized MXene-$FeWO_4$ ternary heterostructure in another study through electrospinning. Bimetallic $FeWO_4$ nanofibers were then surface tagged to delaminated $Ti_3C_2T_x$ single-layered MXenes. Figure 10A represents the formation process of MXene, $FeWO_4$ nanofibers, fabrication procedure of the MXene-$FeWO_4$ composite sensor for the detection of rutin and electrode fabrication strategy. An electrically charged interconnecting network composed of a single-layered MXene and mixed metal oxide nanofibers with many faulty plane/edge sites showed strong electrocatalytic rutin oxidation characteristics. Obtained findings show that the proposed material outperformed bare GCE, WO_3-GCE, $FeWO_4$-GCE, MXene-GCE, and MXene-WO_3-GCE electrodes about anodic peak intensity and overpotential. Figure 10B shows the rutin SWV profiles with different (4 to 147 nM) concentrations on MXene/$FeWO_4$/GCE (7.0 pH), and Figure 10C shows the corresponding calibration

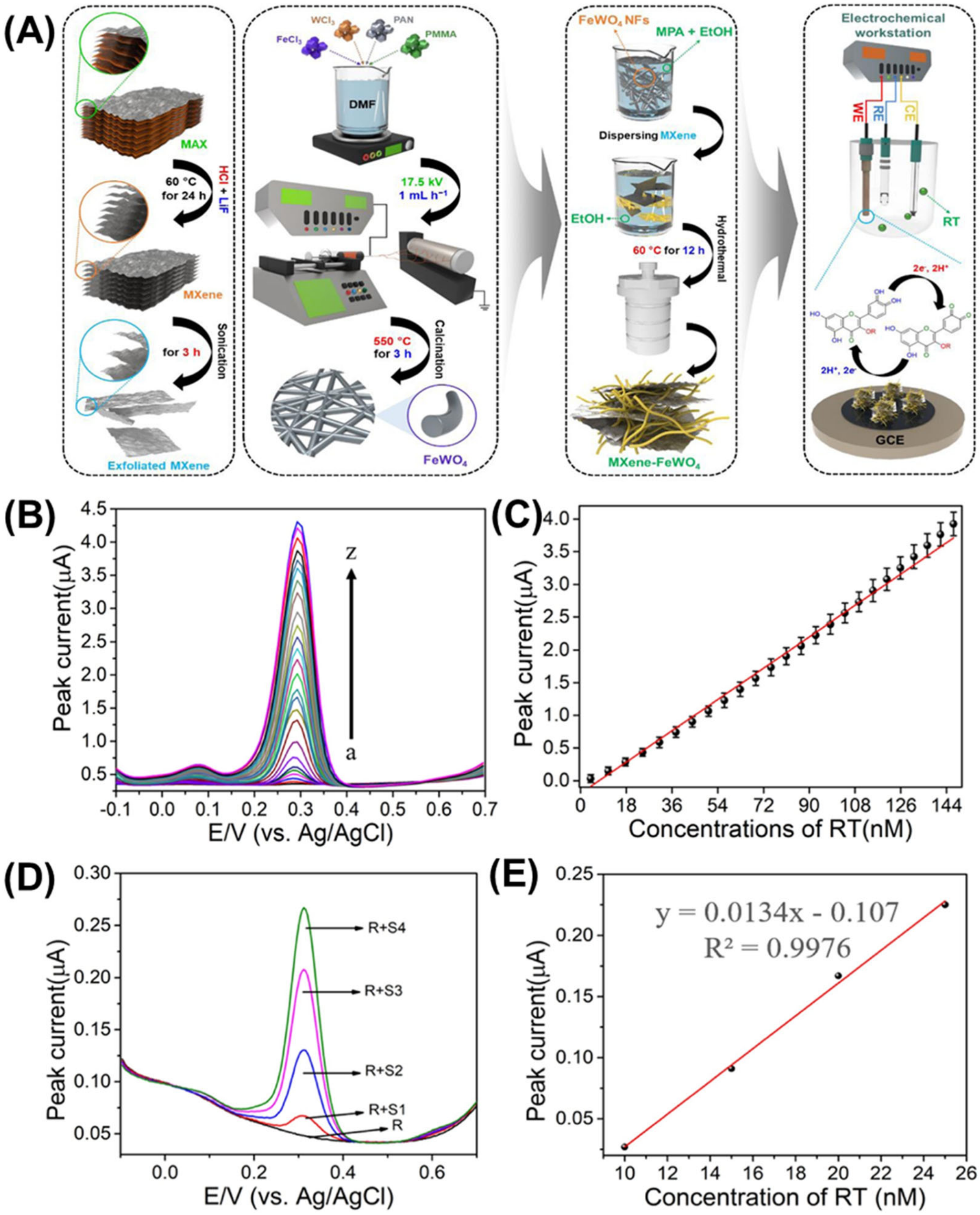

FIGURE 10 | (A) Schematic representation of formation of MXene, FeWO$_4$ nanofibers, fabrication procedure of MXene-FeWO$_4$ composite sensor for the detection of rutin and electrode fabrication strategy. (B) Rutin SWV profiles with different (4 to 147 nM) concentrations on MXene/FeWO$_4$/GCE (7.0 pH). (C) Corresponding calibration graph between rutin concentrations and the anodic current profile of sensor. (D) Rutin analysis in the human serum utilizing MXene/FeWO$_4$/GCE through standard addition system. (E) Corresponding calibration graph for oxidation peak current versus rutin. Reproduced with permission: Copyright 2021, Elsevier [153].

graph between rutin concentrations and anodic current profile of sensor. Figure 10D shows the rutin analysis in the human serum utilizing MXene/FeWO$_4$/GCE through a standard addition system, and Figure 10E shows the corresponding calibration graph for oxidation peak current versus rutin. Volumetric investigations of the produced MXene-FeWO$_4$ nanocomposite revealed 0.42 nM LOD, a 4–147 nM linear range, and 0.3799 μA/(nM·cm^2) high sensitivity. As confirmed by electrochemical analysis, the MXene/FeWO$_4$ nanocomposite demonstrated acceptable stability and continual anti-interference capability. Additionally, the designed nanocomposite revealed suitable recoveries when employed to detect the rutin in black tea, orange juice and human serum samples. The designed sensor revealed exceptional anti-interference capability and selectivity compared to other interfering analytes used in this study [153]. The fascinating properties of MXenes make them substantially suitable for electrochemical sensing applications. Fascinating properties of MXenes for electrochemical sensing applications include high electrical conductivity, large surface area, hydrophilic nature, tunable surface chemistry, exceptional electrocatalytic activity, wide electrochemical window, mechanical flexibility, good biocompatibility, and stability. The electroanalytical performances of the MXene-based materials are shown in Table 4.

TABLE 4 | Electroanalytical performances of the MXene-based materials.

S. no	Electrode	Analyte/target	Linear range	Technique	LOD	References
1	$MnMoO_4$-MXene-GCE	Hydroquinone and catechol	5–65 nM	DPV	0.26 nM and 0.30 nM	[152]
2	MXene-$FeWO_4$-GCE	Rutin	4–147 nM	SWV	0.42 nM	[153]
3	$Ti_3C_2T_x$/-APBA/SPCE	Dopamine (buffer/serum)	40–500 nM	DPV	1.3 nM/1.9 nM	[149]
4	Pt/MXene/CH/Pt	Glucose detection in sweat	0–8 mM		29.15 μM	[145]
5	Pt-MXene/GCE	Quercetin	0.001–0.1, 0.1–1.0 ($nM \times 10^3$)	DPV	0.92 nM	[148]
6	Tris-AgNP/L-Cys/MXene	5-hydroxytryptamine	0.5–150 μM	DPV	0.08 μM	[146]
7	$Ti_3C_2T_x$-MXene sheets and graphene	Cortisol	1 fM to 10 μM	SWV	0.4 fM	[150]
8	MOF-Ti_3C_2/GCE	Dopamine		DPV	110 nM	[144]
9	N-Ti_3C_2/PC	4-aminophenol and acetaminophen	1–150 μM	DPV	0.059 μM and 0.050 μM	[135]
10	Au-Pd/MXene/LSG	Ascorbic acid, dopamine, and uric acid	10–1600 μM for AA, 12–240 μM DA, and 8–100, 200–800 μM UA.	DPV	3 μM AA, 0.13 μM DA, and 1.47 μM UA	[136]
11	V_2O_5@$Ti_3C_2T_x$	Bisphenol A	411 nm–31.2 μM	DPV	87 nm	[141]
12	AuNP@$Ti_3C_2T_x$ (MXene)	Uric acid and folic acid	0.02–3580 μM for uric acid and 0.03–1520 μM for folic acid		6.20 nM for uric acid and 11.5 nM for folic acid	[141]
13	VO-TiO_2@MXene	Imidacloprid	0.07–10.0 μM and 10.0–70.0 μM	LSV	0.023 μM	[140]
14	MXene/N-rGO/GCE	Adrenaline	0.01–90 μM	DPV	3 nM	[138]
15	3D MGMX/SPCE	Zn^{2+}, Cd^{2+}, and Pb^{2+}	3–900 μg/L	DPASV	0.48, 0.45, and 0.29 μg/L	[142]
16	MXene fibers/MIPs/SPE	Hydrocortisone	$0.5–1 \times 10^4$ nM	DPV	0.17 nM	[143]

2.5 | MXene Used for Environmental Remediation

The rapid growth of industry and economy has led to significant environmental damage, especially to water resources, due to the release of pollutants like heavy metals, radioactive elements, and organic substances [154, 155]. This has created complex contamination and health risks. Nanomaterials are being increasingly used as cost-effective and environmentally friendly solutions, particularly in wastewater treatment, serving various functions like catalysts and adsorbents. These advanced nanomaterials encompass a range of substances such as graphene, CNTs, LDHs, nanoscale zerovalent iron (nZVI), MOFs, COFs, among others. However, their practical application is hindered by factors like high costs and complex preparation processes (e.g., graphene, CNTs, MOFs, COFs), limited removal capabilities (e.g., LDHs, nZVI), and chemical instability (e.g., nZVI, MOFs, COFs) [156]. Consequently, there is a pressing need for researchers to explore cost-effective materials, exhibit excellent removal efficiency, and possess high chemical stability for effective environmental remediation [157].

MXenes represent a novel class of 2D nanomaterials composed of transition metal nitrides, carbides, and carbonitrides. The general formula for MXenes is $M_{n+1}X_nT_x$ (where $n = 1$–3), with M representing early transition metals like Ti, Zr, Hf, V, Sc, Nb, Ta, and Mo, X denoting carbon and/or nitrogen, and T referring to surface terminated groups such as —F, —OH, —O, and so forth [158]. Titanium-based MXenes, notably Ti_2CT_x and $Ti_3C_2T_x$, are particularly promising for environmental remediation due to their abundant elemental availability and nontoxic degradation products [159]. $Ti_3C_2T_x$ MXenes, obtained by selectively etching the A layers in Ti_3AC_2 (where A is Zn, Si, Al, and Ga), has become a focal point in MXene-based nanomaterial research for water purification [160]. This is primarily attributed to the exceptional intrinsic properties of $Ti_3C_2T_x$:

1. $Ti_3C_2T_x$ possesses abundant terminal functional groups and a large specific surface area, providing numerous binding sites for strong chemical interactions with contaminants [25].
2. Its outstanding metallic conductivity ensures high-efficiency separation of photogenerated electrons and holes, as well as rapid carrier migration.
3. The reactivity of exposed terminal metal sites on $Ti_3C_2T_x$ may surpass that of carbon-based materials [161].

Nanomaterial performance and utility are heavily influenced by their dimensions and shapes. The accordion structure of layered $Ti_3C_2T_x$ MXenes can easily transform into 0D quantum dot (QD) materials and ultrathin 2D single nanosheets, expanding possibilities for developing high-performance environmental remediation materials [162]. MXenes are relatively new 2D nanomaterials that have been extensively studied, particularly in the realms of environmental remediation [163–166], outlined MXenes' applications in environmental remediation, including their use as adsorbents, catalytic substrates, membranes for water treatment/desalination, and bactericidal agents. Kumar et al. [167] delved into the preparation, characteristics, and applications of MXenes/MXene-based composites, particularly in catalysis, water remediation, and sensor technologies.

One of the applications of MXene in environmental remediation is the removal of antibiotics from the environment. Antibiotics play a crucial role in treating bacterial infections in various sectors such as poultry farming, placental mammal breeding, and medical treatment [168]. Commonly used antibiotics include sulfas, tetracyclines, fluoroquinolones, and other antibiotic drugs. However, excessive antibiotic use can cause significant environmental harm. Sulfonamide antibiotics like sulfamethoxazole and trimethoprim (SMZ) have complex structures, are hydrophilic, and exhibit chemical stability [169]. Photocatalysis is one effective method for degrading antibiotics. Researchers have documented the degradation of these antibiotics and explored the use of MXene-based polymers for this purpose [170].

Jatoi et al. [165] summarize different studies for antibiotic removal by MXene and concluded that MXene-regulated MOF heterojunctions can effectively catalyze the degradation of Cathomycin (TC) complex —HCl, achieving an 82.80% degradation in 60 min. The results from the experiments conclude that gas and hydroxide played crucial roles as active components in the photocatalytic breakdown of TC—HCl. When comparing the photocatalytic breakdown rates of SMZ on $CuFe_2O_4$/MXene (CFO/Ti_3C_2) heterostructures (with a rate constant of $k = 0.0128\ min^{-1}$), they were found to be higher than those on Ti_3C_2 MXene alone ($2.52 \times 10^4\ min^{-1}$). The degradation pathway of SMZ on CFO/Ti_3C_2 involved the action of —OH radicals, leading to the disruption of S-N linkages, amine oxidation, and chemical reactions [171].

Numerous researchers have suggested that $Ti_3C_2T_x$ MXene exhibits antimicrobial properties, capable of targeting waterborne microorganisms such as *Escherichia coli*, *Staphylococcus aureus*, and *Bacillus subtilis*. However, the research on MXene's antimicrobial effects is currently limited [172]. Shahzad et al. [173] made a groundbreaking discovery by demonstrating that $Ti_3C_2T_x$ MXene could serve as an effective and affordable antimicrobial agent for water purification. Their study revealed a significant reduction in microbial activity, particularly as the dose of $Ti_3C_2T_x$ increased, showcasing its potent antimicrobial properties. Furthermore, the antimicrobial efficacy of $Ti_3C_2T_x$ varied significantly from GO, indicating its superior antibacterial capabilities. While Ti_3C_2 demonstrates clear antibacterial effects compared to Ti_2C-MXene, the incorporation of silver into MXene composites has been shown to enhance their antimicrobial properties beyond those of Ti_2C MXene [174, 175].

MXenes have properties such as excellent electrical conductivity, hydrophilicity, and the ability to intercalate ions. For instance, Sukidpaneenid et al. [176] have transformed MXene (MX) into MX-TiO_2 composites via a straightforward and rapid microwave hydrothermal process in an HCl/NaCl solution. This treatment facilitated the formation of fine TiO_2 particles on the MX substrate, rendering the resulting MX-TiO_2 composites photo-catalytically active. These composites were utilized for the removal of enrofloxacin (ENR), a common contaminant found in water bodies. The proportion of MX and TiO_2 in the composites was adjustable by controlling the hydrothermal

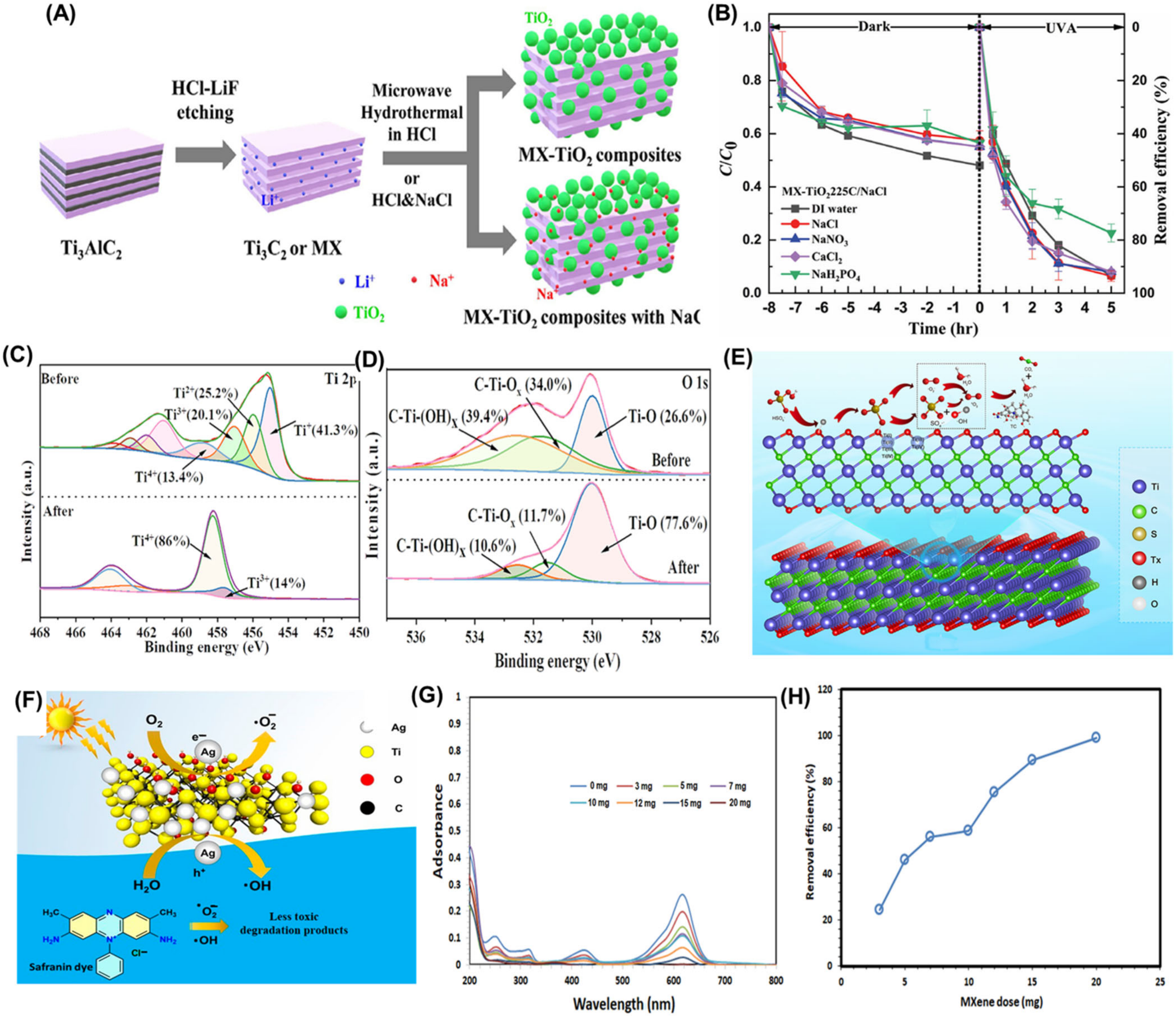

FIGURE 11 | (A) Synthesis of Ti_3C_2-TiO_2 (MX-TiO_2) composites, with or without the inclusion of NaCl. (B) Investigating the impact of various salts on the removal of enrofloxacin, as measured by the C/C_0 ratio, under both dark conditions and UVA radiation. The experimental parameters include a salt concentration of 10 mmol/L, a catalyst loading of 1 g/L, and an initial enrofloxacin concentration of 10 mg/L. Reproduced with permission: Copyright 2023, Elsevier [176]. XPS spectra for Ti 2p (C) and O 1 s (D) of Ff-$Ti_3C_2T_x$ before and after reaction, (E) proposed reaction mechanism of the Ff-$Ti_3C_2T_x$/PMS system. Reproduced with permission: Copyright 2023, Elsevier [177]. (F) Suggested photocatalytic process for breaking down safranin dye employing Ag@ $Ti_3C_2T_x$ nanocomposites. Reproduced with permission: Copyright 2024, MDPI [178]. The impact of varying doses of MXNS on MG removal was investigated in terms of (G) alterations in the UV-vis absorbance spectrum, and (H) fluctuations in removal efficiency corresponding to different MXNS doses. Reproduced with permission: Copyright 2022, MDPI [179].

temperature, allowing for the creation of composites with tuneable adsorption and photocatalytic properties. Figure 11A is provided to demonstrate the synthesis of Ti_3C_2-TiO_2 (MX-TiO_2) composites with or without NaCl. The sizes of the components in the illustration are not to scale and are intended for visualization purposes only. Notably, the addition of NaCl played a crucial role, as composites synthesized without NaCl exhibited poor ENR adsorption. The inclusion of NaCl during hydrothermal treatment led to the intercalation of sodium ions into the composite structure, significantly enhancing ENR adsorption from 1 to 6 mg ENR/g composite. The adsorbed ENR on the composites could be efficiently degraded by free radicals generated from photoexcited TiO_2 particles, showcasing high photocatalytic degradation efficiency. This highlights the synergistic effect between adsorption and photocatalytic degradation in the synthesized compounds [180].

Moreover, the impact of various salts (NaCl, $NaNO_3$, NaH_2PO_4, $CaCl_2$) at a concentration of 10 mmol/L on the adsorption and photocatalytic degradation of the MX-TiO_2@225 C/NaCl composite was investigated and depicted in Figure 11B [176]. In the absence of light, the presence of salts led to a slight reduction in the ENR removal efficiency of the composite, decreasing from 51% in DI water to approximately 43% with salts present. This decrease could be attributed to the competition between ENR and the salt cations for adsorption onto the MX component of the composite. Interestingly, divalent Ca^{2+} ions did not demonstrate any significant difference in adsorption compared to monovalent Na^+ ions. This suggests that ENR binds strongly enough to the MX component of the composite, such that the presence of either monovalent or divalent cations in the surrounding medium does not significantly impact its adsorption behavior. The presence of NaCl, $NaNO_3$, or $CaCl_2$ salts did not significantly affect the photocatalytic degradation rates, which remained like those in DI water. However, NaH_2PO_4 led to a notable decrease in photocatalytic degradation, likely due to phosphate binding to the positive TiO_2 surface, suppressing its photocatalytic activity. Interestingly, phosphate anions did not cause a significant change in composite adsorption under dark conditions, indicating that ENR primarily absorbed onto the MX component, which has a negative zeta potential due to its surface functional groups. MX has been shown to have high cation adsorption capability but minimal anion adsorption [181].

Another example of antibiotics removal by MXene is fluorine-free $Ti_3C_2T_x$ (Ff-$Ti_3C_2T_x$) using a safer and more environmentally friendly tetramethylammonium hydroxide solution (TMAOH) at a controlled temperature of 40°C, with continuous reaction for 1 week. Wang et al. [177] prepared Ff-$Ti_3C_2T_x$ which exhibited exceptional hydrophilicity and exposed more active sites on the surface, which enhances the activation of peroxymonosulfate (PMS). The catalyst showed superior degradation of tetracycline hydrochloride (TC) compared to Fluorine-$Ti_3C_2T_x$ (F-$Ti_3C_2T_x$). We systematically investigated the effects of catalyst dosage, optimal PMS concentration, initial pH, common coexisting ions (Cl^-, $SO_4{}^{2-}$, $HCO_3{}^-$, and humic acid), and different real water environments on TC degradation in the Ff-$Ti_3C_2T_x$/PMS system. Moreover, the degradation efficiency for both Doxycycline and Oxytetracycline exceeded 89.7%. Additionally, Ff-$Ti_3C_2T_x$ showed excellent reusability with a mineralization efficiency of 49.7%. Figure 11C–E presents the XPS spectra for Ti 2p and O 1 s of Ff-$Ti_3C_2T_x$ before and after the reaction, and the proposed reaction mechanism of the Ff-$Ti_3C_2T_x$/PMS, respectively. XPS analysis explains chemical changes in elements during the activation and catalytic degradation of PMS in the Ff-$Ti_3C_2T_x$/PMS system. The Ti binding energy, divided into four peaks, revealed shifts corresponding to different valence states in Figure 11C. After three usage cycles, a decrease in ≡Ti(III) and the disappearance of ≡Ti(I) and ≡Ti (II) suggested the involvement of low-valence ≡Ti in the reaction, while an increase in ≡Ti(IV) indicated its role as the active site for PMS activation and ROS generation. The O 1 s spectra displayed three types of oxygen coordination (Ti─O bonds, C─Ti─O_x bonds, and C─Ti─$(OH)_x$ bond), with reduced contents of C─Ti─O_x and C─Ti─$(OH)_x$ after catalytic reaction, showing their participation in PMS activation in Figure 11D. These findings confirmed the catalytic role of Ti_3C_2 surface functional groups. Based on ROS identification and XPS analysis, a proposed mechanism depicted in Figure 11E illustrates both radical and non-radical mediated PMS activation mechanisms during TC degradation, facilitated by the super hydrophilicity of Ff-Ti_3C_2T.

Lv et al. [182] presented the results for dye removal, which encompass a group of organic compounds known for imparting vivid and enduring colors to other substances, whether in molecular or dispersed form. These compounds are categorized based on their chemical properties and applications into various types such as disperse dyes, azoic dyes, reaction dyes, acid dyes, polycondensation dyes, vat dyes, and cationic dyes [183, 184]. For example, methylene blue, a representative cationic dye, finds extensive use across diverse industries including pharmaceuticals, cosmetics, printing, and textiles [185, 186]. MXenes have garnered attention as a promising material with attributes like a substantial surface area, high thermal and electrical conductivity, and an adjustable band gap, showcasing notable hydrophilicity and stability. These qualities make MXene-based 2D nanomaterials efficient photocatalysts for breaking down organic pollutants due to their adsorption and reducing capabilities [187]. Faheem et al. [178] synthesized silver nanoparticles on exfoliated MXene sheets, with varying ratios of silver salt to MXene (1:50 and 1:20 by weight), using polyvinyl pyrrolidone as a dispersant. This modification led to excellent catalytic performance, with the nanocomposites degrading around 99% of safranin dye within 15 min at a concentration of 5 mg Ag50@$Ti_3C_2T_x$. Figure 11F shows the degradation process of saffron dye. It is primarily governed by redox reactions occurring on the surface of silver nanoparticles embedded in MXene sheets, facilitated by the presence of electrons and holes. When visible light interacts with the catalyst surface, photogenerated electrons and holes are produced, leading to the formation of radical ions. Specifically, radical ions •OH and $\bullet O^{2-}$ are generated as electrons reduce adsorbed O_2 molecules to $\bullet O^{2-}$, while holes oxidize water molecules into hydroxyl radicals. These radical species, being highly reactive, interact with the dye molecules and convert them into less toxic byproducts. The layered structure of the MXene sheet effectively traps electrons due to its high receptivity and enhances charge carrier separation owing to the large catalyst surface area. These trapped electrons subsequently react with adsorbed oxygen, leading to the conversion of oxides into superoxide radicals, $\bullet O^{2-}$. Conversely, holes carrying a positive charge react with water molecules to form hydroxyl radicals.

Other than saffron, malachite is also one of the highly discussed dyes to remove by using MXene. Albukhari et al. [179] synthesized 2D MXene nanosheets (MXNSs) from Ti_3AlC_2 MAX phase powders. These synthesized MXNSs were then employed as a solid adsorbent for removing malachite green dye (MG) from water. The adsorption experiments demonstrated that solution temperature and pH significantly impacted MG removal using MXNS. Optimal removal efficiency was achieved within 150 min with 20 mg of MXNS at ambient temperature and a pH of 6.0. The maximum MG removal capacity was found to be 4.6 mg/g of MXNS, resulting in a removal efficacy of 46.0%, while the minimum removal capacity was 2.5 mg MG per gram of MXNS, with a removal efficacy of 99.1%. Figure 11G investigated the impact of MXNS solid adsorbent dosage on MG removal through adsorption. It illustrates changes in the UV-vis absorbance spectrum, and Figure 11H depicts alterations in removal efficiency concerning MXNS doses. The highest removal capacity achieved was 4.6 mg of MG per gram of MXNS using 5 mg of MXNS, resulting in a removal efficiency of 46.0%. Conversely, the lowest removal capacity observed was 2.5 mg of MG per gram of MXNS using 20 mg of MXNS, with a removal efficiency of 99.1%. Notably, MG removal using MXNS increased with higher MXNS doses, likely due to enhanced access to adsorption active sites as the adsorbent dose increased [188].

2.6 | Removal of Heavy Metal Ions by Using MXene

Issues related to water continue to be a significant concern worldwide. Various elements, including urban development, industrial activities, and population expansion, have placed considerable pressure on water resources. One of the principal sources of pollution in this context is the improper disposal of industrial waste [189]. This waste, often untreated, contributes to pollution with a vast array of pollutants, including toxic dyes, chemical byproducts, and dangerous substances emanating from sectors such as textiles, printing, plastics, leather, food processing, and pharmaceuticals [190]. These pollutants pose increasing risks to human health and the environment. Therefore, finding safe, chemically viable, and eco-friendly methods for eliminating these contaminants is of utmost importance [191].

Technologies such as sorption, membrane filtration, photocatalytic degradation, and electrocatalytic detection are recognized as effective and cost-efficient methods for environmental remediation, aimed at capturing, isolating, breaking down, and detecting pollutants [192]. Materials like polymers, carbon derivatives, metals, and metal oxides have been utilized in these innovative approaches for adsorption, photocatalysis, or as bases for sensors [193]. MXene compounds, which have been extensively developed and synthesized, are notable for their unique structure comprising transition metal, carbon or nitride groups, and surface functionalities such as ─OH, ─F, and ─O [194]. These surface characteristics significantly enhance the physical and chemical properties of MXenes, influencing their performance in applications involving surface interaction, including catalysis and membrane filtration [195]. Unlike graphene, which exhibits limited wettability, MXenes display superior hydrophilicity and a propensity for specific ion exchanges and redox reactions, attributed to their surface functionalities [158]. Previous studies have demonstrated that the presence of multiple active sites on MXene surfaces enables them to efficiently remove contaminants like heavy metal ions and organic dyes from the environment [81].

Heavy metal ions pose a significant threat to the environment due to their persistent and long-lasting nature. Their toxicity remains potent even at low levels, leading to the generation of harmful pollutants that require immediate mitigation. Various methods, such as chemical precipitation, flotation, sorption, and electrodialysis, are employed to eliminate these ions. Unlike dyes that are more concentrated in aquatic environments and easier to remove, heavy metal ions present a greater challenge due to their lower concentrations [196]. Biological treatment methods are often ineffective at these low concentrations. MXene and its compounds, known for their significant surface area and various surface functions, are considered effective adsorbents for heavy metal ions. Numerous studies have demonstrated MXene's high capacity for adsorbing a wide range of heavy metal ions onto its surfaces [197, 198]. Zhang et al. [199] developed a novel sandwiched field composite of MXene and iron oxide (MXI) by incorporating magnetic oxide at timed intervals into MXene. One of the various applications of the MXI composite is its ability to absorb trace amounts of phosphate. This composite demonstrated superior performance compared to traditional adsorbents, achieving a separation time of 20 s and process efficiencies of 21,102 and 24,102 kg^{-1} in both simulated and real phosphate effluents. The exceptional sequestration capability was attributed to the unique nano-ferric compound structure, where ultrafine nano-Fe_2O_3 components could deeply penetrate MXene layers, increasing the surface area and enhancing active layer accessibility. Apart from the heavy metals mentioned earlier, researchers have also explored the removal of other heavy metal ions like Cu^{2+}, Hg^{2+}, and Ag^{+1}. For instance, Shahzad et al. [200] demonstrated that magnetic $Ti_3C_2T_x$ had a high surface adsorption capacity for Hg^{2+} at 128 mg/g, surpassing MXene-based composites such as MXene-$SA_{2:20}$ and MXene-$SA_{4:20}$ (with sorption capacities around 364.52 and 932.84 mg/g, respectively). This enhanced sorption potential of MXene is attributed to its remarkable porosity, high aspect ratio, and abundant functional groups.

N-doped MXene QDs have shown significant sensitivity to various positively charged metal ions under visible light, with Cu^{2+} causing the highest photoluminescence (PL) quenching at 56%, followed by Fe^{3+} (32%) and other ions (10%). This suggests strong interactions between copper ions and N-doped amino units, leading to PL quenching due to Cu_2@QD complex formation. Phenolic resin compounds are hazardous hydrocarbon pollutants commonly found in industries like petrochemicals, printing, dyeing, and pesticides. $Fe_2O_3/Ti_3C_2T_x$ and $Ag/Ti_3C_2T_x$ composites are widely utilized for the removal and degradation of hydrocarbons in the presence of radiation, thanks to their efficient and significant properties [165]. Additionally, Feng et al. [201] developed a unique $Ti_3C_2T_x$ composite by replacing terminal fluorine atoms on $Ti_3C_2T_x$ with oxygen-containing functional groups, followed by an alkalization process. This composite showed improved catalytic performance for hydrodechlorination of 4-chlorophenols, achieving an 82.2% conversion rate.

The process of removing heavy metal cations and co-existing anions is a key aspect of producing purified water for industrial use. Over the past decade, significant attention has been directed towards laminar MXene membranes in separation technology. These membranes, particularly thermal self-crosslinking MXene variants, have shown promising anti-swelling properties. However, the reduction in negative charge during self-crosslinking can lead to a decline in ion separation efficiency due to reduced adsorption capacity or weakened control over surface charge. To address this issue and restore surface charge, researchers have adopted a method involving the hydroxylation of MXene membranes by replacing ─F with ─OH using an alkali such as KOH, as mentioned in Figure 12A. The ion rejection test was performed using a custom apparatus equipped with a membrane area measuring 9.62 cm^2. An external electric voltage served as the driving force to augment ion permeation. This experimental configuration featured three cells created by employing two selective Ak-MXene membranes, illustrated in Figure 12B. The central

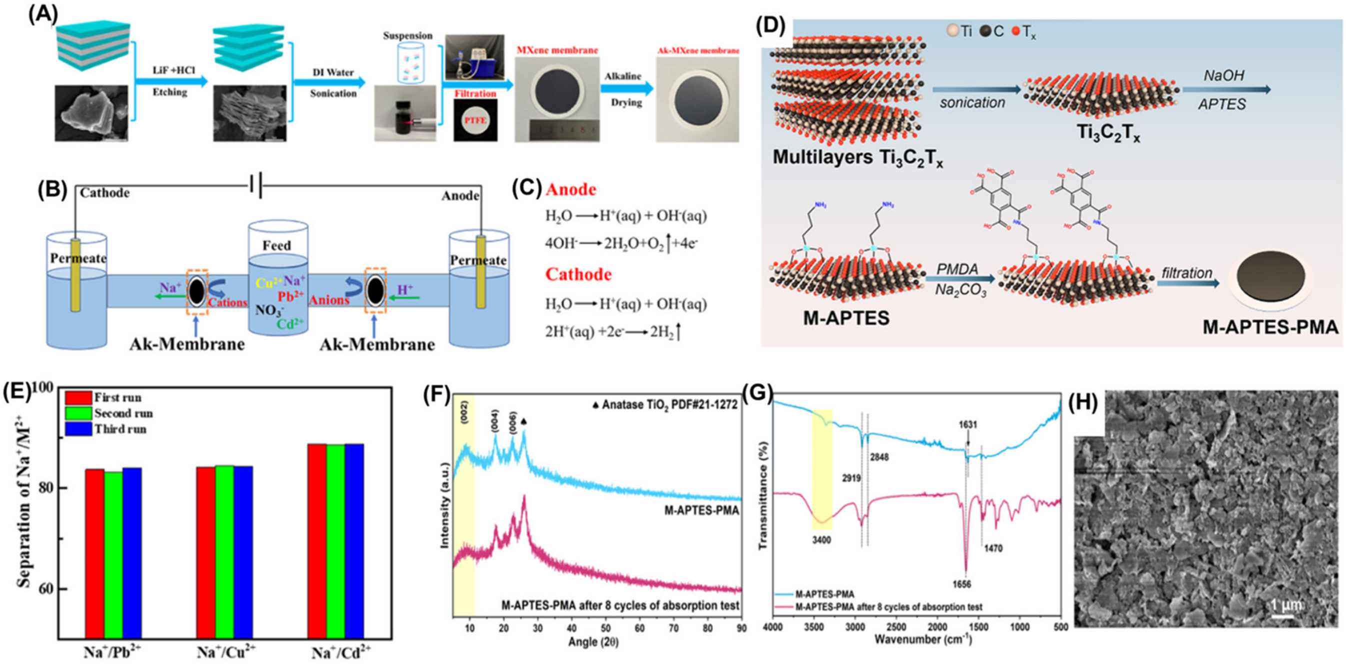

FIGURE 12 | (A) Preparation of Ak-membrane, (B) removal of heavy metal ions and permeation under applied voltage, and (C) the reactions in anode and cathode sides, (D) the separation factors for three different subsequent runs under the optimized parameters. Reproduced with permission: Copyright 2021, Elsevier [202]. (E) Schematic of fabrication process of the M-APTES-PMA, (F) XRD patterns, and (G) FT-IR of the M-APTES-PMA membrane before and after eight cycles of absorption test. (H) Surface SEM of the M-APTES-PMA membrane after eight cycles of absorption test. Reproduced with permission: Copyright 2023, Elsevier [203].

chamber functioned as the feed chamber, whereas the chambers flanking it functioned as permeation chambers. The membranes were affixed securely using an airtight sealant, and electrodes were positioned within the permeation chambers to apply an electric field. One Ak-MXene membrane near the cathode cell was employed for cation filtration from the feed, while another membrane was used to repel anions and prevent the electrolysis of anions (Cl^- and NO_3^-) at the anode. pH test paper was utilized to monitor the gas produced near the electrodes for acidity and alkalinity assessment. During the tests, a high-sensitivity electronic balance measured water weight loss to monitor ion sieving. To eliminate the influence of pressure differences on ion sieving, experiments were conducted under various applied voltages without pressure alterations. The initial solution had controlled concentrations of Na^+ and Pb^{2+} (or Cu^{2+} and Cd^{2+}) at around 50 mg/L, with anions added to the introduced cations. The expected chemical reactions on the anode and cathode sides are mentioned in Figure 12C [202].

Similarly, the difference in separation factors between MXene and Ak-MXene membranes becomes more pronounced as the testing duration extends, indicating that an increase in surface charge has a positive impact on separation efficiency. To assess the consistency of the fabricated membranes, separation factors were evaluated for three distinct Ak-MXene membranes, as depicted in Figure 12D. Slight fluctuations observed for Na^+/Pb^{2+}, Na^+/Cu^{2+}, and Na^+/Cd^{2+} pairs underscore the reliability of both the membrane and the synthesis process. The resulting hydroxylated MXene membrane exhibits superior performance in terms of wettability and Zeta potential compared to the pristine MXene membrane, enhancing the rejection and separation of ions. When these selectively modified membranes are used to remove heavy metal cations (such as Pb^{2+}, Cu^{2+}, and Cd^{2+}) along with co-existing anions (e.g., Cl and/or NO_3) under an appropriate electronic field strength, a rejection rate of 99.5% can be achieved at 12 V for a 383 nm-thick hydroxylated MXene membrane, surpassing that of the pristine MXene membrane. Consequently, co-existing anions are also excluded at a rate of approximately 97% due to increased surface charge control. Furthermore, the hydroxylated MXene membrane exhibits selective separation permeance for Na^+/Pb^{2+}, Na^+/Cu^{2+}, and Na^+/Cd^{2+} pairs. By adjusting the interlayer spacing through the thermal self-linking process, excellent operational durability and reproducibility are achieved during a 70-min test period. These findings underscore the potential of developing and implementing 2D laminar membranes, particularly hydroxylated MXene variants, for wastewater treatment and separation applications.

Another approach is the development of titanium carbide ($Ti_3C_2T_x$), an emerging 2D material that holds significant importance in oil-water separation due to its abundant hydrophilic groups on the surface [203]. A precise grafting method is available to modify MXene sheets with pyromellitic acid groups, resulting in the preparation of a multifunctional MXene-based membrane. The process of preparing the M-APTES-PMA membrane is outlined in Figure 12E. Initially, the "Al" layer in the Ti_3AlC_2 MAX phase was etched using the "HCl/LiF" system, resulting in a single-layer MXene sheet obtained through ultrasonic dispersion and centrifugation. Subsequently, the MXene sheets underwent alkali treatment to increase surface hydrophilicity and create more sites for

APTES modification, which enhances oil-water separation efficiency. Pyromellitic dianhydride (PDMA) was then grafted onto the MXene surface through 3-Aminopropyl triethoxysilane (APTES) modification, forming covalent bonds via amidation reactions with the amino group and anhydride. The M-APTES-PMA sample was obtained through a hydrolysis reaction, and finally, the M-APTES-PMA membrane was fabricated by filtering the M-APTES-PMA suspension onto a PVDF substrate membrane. To evaluate the stability of the M-APTES-PMA membrane following eight cycles of heavy metal ion removal, we employed XRD, FT-IR, and SEM techniques for characterization purposes. Figure 12F shows a slight increase in intensity at the characteristic peak of 25.6°, possibly due to the oxidation of MXene sheets by Cu^{2+}, resulting in TiO_2 formation [204]. In the FT-IR analysis (Figure 12G), the stretching vibration peaks of APTES, PMA, and amide bonds were still evident, indicating the preservation of chemical bonds after eight absorption cycles. Additionally, SEM images (Figure 12H) depicted stacked sheets on the membrane surface, along with flatter cracks, likely caused by fluid flow compression. These observations suggest that the M-APTES-PMA membrane maintained stability even after undergoing eight absorption cycles [203]. Due to the plentiful hydrophilic groups on the surface of MXene sheets, the membrane exhibited exceptional superhydrophilic and anti-oil adhesion characteristics. It also displayed remarkable separation performance (6731.8 $L/(m^2 \cdot h \cdot bar)$ and $> 99.97\%$) for high-viscosity emulsions. The inclusion of grafting groups notably enhanced the membrane's removal efficiency for various heavy metal ions ($> 99\%$). Furthermore, it displayed superior chemical stability, flexibility, and effective separation of harsh emulsions [203].

Notably, MXene has been documented in various nanofiber forms, creating flexible, stable, and porous composites widely utilized in electronic and optoelectronic applications [205–207]. Surprisingly, MXene-based nanofibers have not yet been explored for the removal of heavy metal ions. Creating a composite nanofiber membrane of MXene/CNFs through PVP proves to be an efficient method for capturing harmful substances from water solutions. This approach offers high mechanical strength, a micro-porous structure, specific surface area, reusability, and stability, attributes inherent to CNFs (carbon composite-based nanofibers). Moreover, leveraging the active sites on MXene with CNFs enhances the selectivity for heavy metals, reducing the risk of human diseases and safeguarding aquatic life. To achieve this, we synthesized MXene from Ti_3AlC_2 MAX phase and incorporated it into PVP nanofibers, followed by a carbonization process to produce MXene/CNFs for heavy metal adsorption. The MXene/carbon composite-based nanofibers (MXene/CNFs) membrane efficiently removes Pb^{2+} and As^{3+} ions to their allowable limits, as demonstrated in an effective adsorption study. The adsorption outcomes corresponded well with both the Langmuir and pseudo-second-order models. Notably, the MXene/CNFs composite membrane exhibited a substantial adsorption capacity for Pb^{2+} (12.5 mg/g) and As^{3+} (3.3 mg/g) at an optimal neutral pH within 20 and 30 min, respectively. The findings depicted in Figure 13A highlighted a significant impact of pH on the adsorption of heavy metals. Cheng et al. [208] noted that as the pH transitions from acidic to neutral, the removal rate increases, but it decreases as the pH shifts towards alkalinity. The reduced removal rates observed under acidic and alkaline conditions may stem from the coagulation and precipitation of heavy metals. Conversely, the increased removal rate at a neutral pH mentioned in Figure 13B can be attributed to the ionic state of heavy metals, which facilitates their attraction to the surface of nanofibers [209].

Moreover, the MXene/CNFs composite membrane demonstrated effective recyclability for up to four cycles, achieving removal efficiencies of 77% for Pb^{2+} and 60% for As^{3+}. This underscores the potential of the prepared MXene/CNFs membrane as an efficient, cost-effective, lightweight, and eco-friendly solution for removing lead and arsenic ions within permissible limits for drinking water. For the first time, a novel hybrid material combining MXene, and chitosan-coated PUF has been developed for wastewater treatment, specifically targeting heavy metal ions such as Cr(VI), as demonstrated through a fixed-bed column study. The MXene and chitosan layers were applied to the PUF in three different layers, resulting in maximum adsorption capacity. This configuration achieved approximately 70% removal of Cr(VI) within the first 10 min and over 60% removal after 3 h. The study also examined the impact of pH, the quantity of MXene and CS (chitosan) coated PUF, and the duration of the reaction on the adsorption efficiency of Cr(VI) through the MXene─CS blend. Figure 13C illustrates the adsorption behavior of $MX_3@CS_3@PUF$ at different pH values. The impact of varying pH levels (2, 4, and 6) on the removal of Cr(VI) from an aqueous solution was investigated. Islam et al. [210] explained that due to the anionic nature of chromium species, the removal of Cr(VI) decreased as pH values increased. The removal efficiency of Cr(VI) was 65% at $pH = 2$, 54% at $pH = 4$, and 20% at $pH = 6$ after 4 h. These findings suggest that acidic conditions favor the removal of Cr(VI). Following each adsorption cycle, regeneration of the $MX_3@CS_3@PUF$ sample was achieved using 0.2 M HCl. The regeneration performance of $MX_3@CS_3@PUF$, tested at a Cr(VI) concentration of 10 ppm, is depicted in Figure 13D, covering three cycles. MXene and chitosan were applied to PUF foam in three distinct layers, demonstrating the highest adsorption capacity. This configuration achieved the removal of approximately 70% of Cr(VI) within the first 10 min and over 60% removal after 3 h at a metal ion concentration of 20 ppm. The elevated removal efficiency can be attributed to the electrostatic interaction between the negative charge of MXene and the positive charge of chitosan on the PUF surface, a feature absent in MX@PUF. These findings were derived from a series of fixed-bed column studies conducted under continuous wastewater flow conditions [211].

Mercury (Hg), widely used in various industries, poses a significant risk as a water pollutant, capable of causing neurological damage. The U.S. Environmental Protection Agency (EPA) has set a maximum permissible limit of 2 ppb for Hg ions in both water and wastewater streams [212]. A straightforward single-step technique for $Ti_3C_2T_x$ carboxylation utilizes a chelating agent featuring a linear structure, resulting in robust carboxylic acid groups with enhanced mobility. This method explores the impact of introducing carboxyl functional groups onto the surface of $Ti_3C_2T_x$ MXene on its ability to adsorb

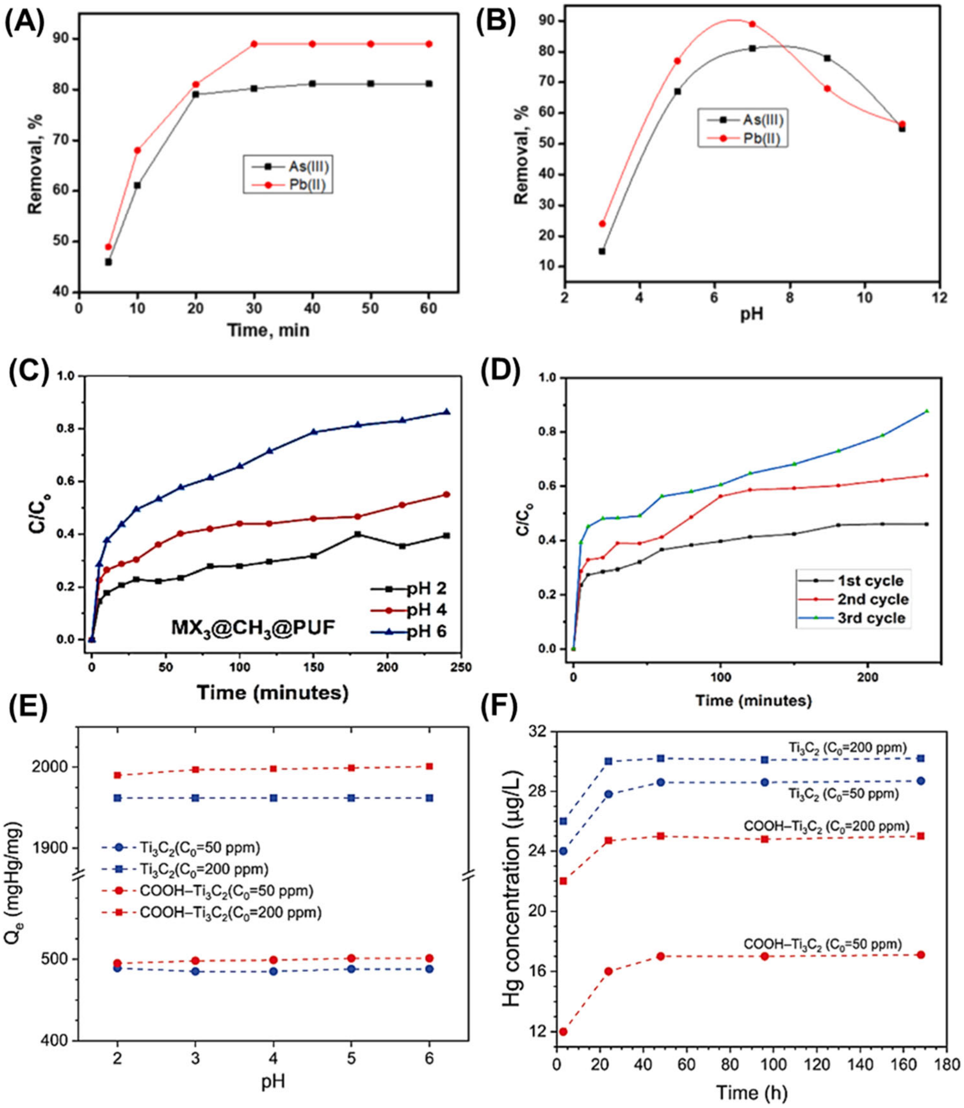

FIGURE 13 | (A) Time and (B) pH effect on adsorption of Pb^{2+} and As^{3+} using MXene/CNFs composite membrane. Reproduced with permission: Copyright 2023, Elsevier [209]. (C) Effect of pH and (D) regeneration step of MX_3@CS_3@PUF for three cycles. Reproduced with permission: Copyright 2023, Elsevier [211]. (E) Mercury uptake of $Ti_3C_2T_x$ and COOH─$Ti_3C_2T_x$ at different pH values, (F) the mercury leaching from the adsorbents versus the extraction time. Reproduced with permission: Copyright 2022, Elsevier [214].

mercury while also reducing $Ti_3C_2T_x$ oxidation, all without compromising the dispersibility and hydrophilicity of the MXene. $Ti_3C_2T_x$ and COOH─$Ti_3C_2T_x$ exhibited notable mercury uptake within the pH range of 2–6 (Figure 13E). The pH level of the effluent plays a crucial role as it can alter the ion complexes, surface charge, and functionalities of the adsorbent. The adsorption capacity of COOH─$Ti_3C_2T_x$ showed a slight increase with rising pH in the range of 2–3, whereas that of $Ti_3C_2T_x$ remained relatively constant. As discussed previously, the less negative surface charge of $Ti_3C_2T_x$ and COOH─$Ti_3C_2T_x$ at lower pH levels may negatively impact their efficiency in adsorbing positively charged Hg ions. Conversely, Hg^{2+} predominates in acidic solutions, undergoing hydrolysis to $Hg(OH)^+$ as the pH approaches neutral values.

Furthermore, studies by Ngatijo et al. [213] suggest that mercury ions tend to establish covalent bonds, which are less influenced by changes in pH compared to ionic interactions. The potential for leaching adsorbed mercury ions from $Ti_3C_2T_x$ and COOH─$Ti_3C_2T_x$ was assessed using two initial Hg concentrations. After 7 days of agitation at room temperature, the highest concentration of mercury ions recorded was 30 μg/L for $Ti_3C_2T_x$ (Figure 13F). This level falls below the U.S. EPA's safe threshold (< 200 μg/L), indicating it as nonhazardous industrial waste. In contrast, the amount of leached mercury from COOH─$Ti_3C_2T_x$ was significantly lower than that from $Ti_3C_2T_x$ due to strong interactions between mercury ions and the COOH functional groups. The concentration of mercury leachate from both samples increased with higher initial concentrations, yet it remained well below the EPA's safety limit. Initially, there was a rapid leaching rate of mercury ions into the solution, which gradually decreased as soluble mercury ions diffused into the solution during the first 24 h. This led to a reduction in the concentration gradient within the adsorbent layers and leachate, resulting in a slower leaching rate over time. Furthermore, the covalently-bonded mercury on $Ti_3C_2T_x$ and COOH─$Ti_3C_2T_x$ remained securely bound and did not leach into the solution [214].

3 | Conclusion and Future Aspects

In summary, the current MXene-based PCMs review highlights the potentiality of 2D MXene nanomaterials in thermal energy conversion, storage, and desalination sectors. The outstanding characteristics of MXene, including its remarkable electrical and thermal conductivity and high light absorptivity, position it as the most promising material for applications in photo-/electrothermal conversion and thermal radiation management. Furthermore, the extensive surface area inherent in MXene enables the creation of vast interfaces for efficient energy transfer and conversion processes, whether light-to-heat conversion efficiency or light-to-water evaporation efficiency. At the same time, its 2D lamellar structure facilitates rapid thermal energy exchange at the interface between solid and liquid phases. A comprehensive understanding of MXene as PCM challenges and insights into future perspectives discussed below will be crucial in unlocking the full potential of MXene for real-world applications.

1. Methodically investigating the impacts of varying MXene factors, such as the number of layers, thickness, and lateral size analysis, on the performance characteristics is crucial for enhancing thermal storage capacity and improving thermal conductivity within the pristine MXene materials as PCM.
2. To delve into the intricate mechanisms at play when incorporating various nanoparticles into MXene PCMs, with the principal objective of developing the field and pushing the boundaries of material design for enhanced thermal performance.
3. To develop novel shape-stabilized PCMs where MXene can be an enhancer in the light-thermal absorption and conversion process. Later, for example, the polyethylene glycol supporting material can be incorporated to obtain high phase change performance; hence, the thermal stability is approaching 90% enthalpy efficiency.
4. The feasibility of integrating alternative PCMs with diverse melting points enables the customization of thermal characteristics to meet specific demands in solar energy storage systems. Developing MXene hybrid aerogels with CNTs and polymers could enhance the light absorption performance, resulting in more robust photothermal energy conversion efficiency.
5. Efforts should be made to expand the range of MXene-based PCMs' operating temperatures and targeted applications to potentially engineer the thermal properties for targeted solar energy storage requirements.
6. A spatial confining forced network assembly can be introduced to create a 3D MXene assembly to have good compatibility to advance solar energy storage efficiency.
7. Indeed, designing MXene-based integrated sponges through rGO or similar graphene-like materials could significantly enhance the thermophysical and photo absorption properties for real-time solar energy storage applications.
8. Considering MXene as top-of-the-line electromagnetic shielding nanomaterials proves the conversion and dissipation of heat within the MXene materials; hence, absorbed EMVs lead to light-to-heat photothermal conversion efficiency materials. At the same time, MXene restricts almost all the electromagnetic emission inspired to check its light-to-water evaporation efficiency.
9. It is significant to simultaneously evaluate the light-to-heat photothermal conversion efficiency and the light-to-water evaporation efficiency of MXene-based PCMs to conclude their internal light-to-heat conversion nanomaterials.
10. Though MXene materials have good thermal conductivity and heat transfer characteristics, macroscopic MXene in the film form suffers from low values. This necessitates the resolution of two pivotal scientific challenges: the regulation of the surface termination of MXene and the mitigation of the thermal resistance at the interface between MXene nanosheets during the fabrication process of macroscopic materials.
11. The mechanical properties, such as tensile and compressive strength, must undergo a systematic investigation for the MXene-based PCMs to ensure smooth device flexibility operation and long-term performance. Mainly, graphene-like materials resist atomic change or movement under the application of external stimuli due to the resisting inner atomic structure. CNTs produce buckles at their weak joint sections, impeding the continuous electronic conduction paths under external pressure and compromising the device's sensitivity and functions. However, MXene can overcome it due to its wide interlayer spacings accordion-like open internal layer arrangements.
12. Furthermore, applying MXene-based PCMs extends to regulating solar panel temperatures, thereby augmenting their operational efficiency and longevity due to their ability to store surplus energy produced by solar panels throughout the day and subsequently disperse it during the night. Their adeptness in offering consistent and effective temperature management facilitates reducing energy wastage and optimizing energy systems' effectiveness.
13. It is imperative to thoroughly assess the feasibility of introducing other carbonaceous additives or oxide/sulfide/phosphide materials into the composites to potentially augment specific properties such as light absorption, heat dissipation, thermal stability, and phase change characteristics, thereby broadening the MXene-based PCMs application potential and versatility.
14. Conducting comprehensive long-term stability studies is essential to evaluate the durability and performance of the MXene-based PCMs under extended cycling conditions. These can offer valuable insights into their reliability and suitability for practical applications in various fields. These investigations and perspectives not only contribute to advancing the fundamental understanding of these innovative materials but also pave the way for their practical utilization in real-world energy storage systems.

15. A detailed computational investigation must be employed to understand the MXene-based PCMs, emphasizing the importance of their structure–property nexus to demonstrate the improved light-thermal absorption and conversion efficiencies, making them suitable for sustainable energy applications.
16. The potential that lies in the promising use of PCMs in storing large amounts of heat produced through solar radiation or heat must also be explored, enhancing their resistance to leakage and improving their photo-to-thermal performance.
17. The 2D laminar MXene structure, versatile surface reactivity, and outstanding thermal attributes allow the investigation of desirable PCM conditions, making them highly suitable for thermal energy production and retention applications.
18. A thorough, in-depth exploration is needed for the structural diversity and their associated effects on the energy storage device performances of MXenes as PCMs for next-generation energy storage systems.
19. The first-principles computational evidence and the mechanistic details must be interpreted together to understand the underlying thermal resistance behavior, specifically at the interface of MXene nanosheets while fabricating macroscopic MXene PCM materials.
20. Furthermore, the AI and ML-enabled generative models in deciding the type and stoichiometry of MXene materials must play a crucial role in determining whether the targeted MXene PCM should undergo light-to-heat conversion or light-to-water evaporation or both, prioritizing their internal conversion efficiencies.

Acknowledgments

This work was supported by the Hong Kong Innovation and Technology Commission (GHP/247/22GD).

Conflicts of Interest

The authors declare no conflicts of interest.

Data Availability Statement

Data will be made available on request.

References

1. H. Schmidt, F. Giustiniano, and G. Eda, “Electronic Transport Properties of Transition Metal Dichalcogenide Field-Effect Devices: Surface and Interface Effects,” *Chemical Society Reviews* 44, no. 21 (2015): 7715–7736.

2. X. Duan, C. Wang, A. Pan, R. Yu, and X. Duan, “Two-Dimensional Transition Metal Dichalcogenides as Atomically Thin Semiconductors: Opportunities and Challenges,” *Chemical Society Reviews* 44, no. 24 (2015): 8859–8876.

3. M. Xu, T. Liang, M. Shi, and H. Chen, “Graphene-Like Two-Dimensional Materials,” *Chemical Reviews* 113, no. 5 (2013): 3766–3798.

4. K. Hantanasirisakul and Y. Gogotsi, “Electronic and Optical Properties of 2D Transition Metal Carbides and Nitrides (MXenes),” *Advanced Materials* 30, no. 52 (2018): 1804779.

5. M. Naguib, M. Kurtoglu, V. Presser, et al., “Two-Dimensional Nanocrystals Produced by Exfoliation of Ti_3AlC_2,” *Advanced Materials* 23 (2011): 4248–4253.

6. N. Goel, A. Kushwaha, and M. Kumar, “Two-Dimensional MXenes: Recent Emerging Applications,” *RSC Advances* 12, no. 39 (2022): 25172–25193.

7. Y. Gogotsi and Q. Huang, “MXenes: Two-Dimensional Building Blocks for Future Materials and Devices,” *ACS Nano* 15, no. 4 (2021): 5775–5780.

8. S. Kumar, N. Kumari, and Y. Seo, “MXenes: Versatile 2D Materials With Tailored Surface Chemistry and Diverse Applications,” *Journal of Energy Chemistry* 90 (2024): 253–293.

9. B. Anasori, M. R. Lukatskaya, and Y. Gogotsi, “2D Metal Carbides and Nitrides (MXenes) for Energy Storage,” *Nature Reviews Materials* 2, no. 2 (2017): 16098.

10. D. Mohapatra, Y. Shin, M. Z. Ansari, et al., “Process Controlled Ruthenium on 2D Engineered V-MXene via Atomic Layer Deposition for Human Healthcare Monitoring,” *Advanced Science* 10, no. 12 (2023): 2206355.

11. M. Naguib, M. W. Barsoum, and Y. Gogotsi, “Ten Years of Progress in the Synthesis and Development of MXenes,” *Advanced Materials* 33, no. 39 (2021): 2103393.

12. M. Naguib, O. Mashtalir, M. R. Lukatskaya, et al., “One-Step Synthesis of Nanocrystalline Transition Metal Oxides on Thin Sheets of Disordered Graphitic Carbon by Oxidation of MXenes,” *Chemical Communications* 50, no. 56 (2014): 7420–7423.

13. D. Mohapatra, J. E. Byun, M. Z. Ansari, et al., “Layer Engineered MXene Empowered Wearable Pressure Sensors for Non-Invasive Vital Human-Machine Interfacing Healthcare Monitoring,” *Advanced Materials Technologies* 8, no. 24 (2023): 2301175.

14. G. Van Lier, C. Van Alsenoy, V. Van Doren, and P. Geerlings, “Ab Initio Study of the Elastic Properties of Single-Walled Carbon Nanotubes and Graphene,” *Chemical Physics Letters* 326, no. 1–2 (2000): 181–185.

15. R. Li, L. Zhang, L. Shi, and P. Wang, “MXene Ti_3C_2: An Effective 2D Light-To-Heat Conversion Material,” *ACS Nano* 11, no. 4 (2017): 3752–3759.

16. V. Velmurugan and K. Srithar, “Prospects and Scopes of Solar Pond: A Detailed Review,” *Renewable and Sustainable Energy Reviews* 12, no. 8 (2008): 2253–2263.

17. W. Xu, J. Su, J. Lin, J. Huang, M. Weng, and Y. Min, “Enhancing the Light-Thermal Absorption and Conversion Capacity of Diatom-Based Biomass/Polyethylene Glycol Composites Phase Change Material by Introducing MXene,” *Journal of Energy Storage* 72 (2023): 108253.

18. A. R. Akhiani, H. S. Cornelis Metselaar, B. C. Ang, M. Mehrali, and M. Mehrali, “MXene/rGO Grafted Sponge With an Integrated Hydrophobic Structure Towards Light-Driven Phase Change Composites,” *Composites, Part B: Engineering* 264 (2023): 110885.

19. Y. Wang, F. Wang, C. Shi, et al., “Monolithic MXene Aerogels Encapsulated Phase Change Composites With Superior Photothermal Conversion and Storage Capability,” *Nanomaterials* 13, no. 10 (2023): 1661.

20. I. Hussain, A. Hanan, F. Bibi, O. J. Kewate, M. S. Javed, and K. Zhang, “Non-Ti (M_2X and M_3X_2) MXenes for Energy Storage/Conversion,” *Advanced Energy Materials* 14 (2024): 2401650.

21. C. Lamiel, I. Hussain, J. H. Warner, and K. Zhang, “Beyond Ti-Based MXenes: A Review of Emerging Non-Ti Based Metal-MXene Structure, Properties, and Applications,” *Materials Today* 63 (2023): 313–338.

22. Y. Li, Y. Li, L. Zhao, et al., “Recent Progress in the Antidegradation Strategies of Two-Dimensional Transition Metal Carbides (MXenes),” *Journal of Environmental Chemical Engineering* 12, no. 3 (2024): 112762.

23. M. Naguib, V. N. Mochalin, M. W. Barsoum, and Y. Gogotsi, “25th Anniversary Article: MXenes: A New Family of Two-Dimensional Materials,” *Advanced Materials* 26, no. 7 (2014): 992–1005.

24. M. Shekhirev, C. E. Shuck, A. Sarycheva, and Y. Gogotsi, “Characterization of MXenes at Every Step, From Their Precursors to Single Flakes and Assembled Films,” *Progress in Materials Science* 120 (2021): 100757.

25. Y. Wei, P. Zhang, R. A. Soomro, Q. Zhu, and B. Xu, “Advances in the Synthesis of 2D MXenes,” *Advanced Materials* 33, no. 39 (2021): 2103148.

26. L. Han, X. Zhang, J. Ji, and K. Ma, “Research Progress on the Influence of Nano-Additives on Phase Change Materials,” *Journal of Energy Storage* 55 (2022): 105807.

27. M. Subramanian, A. T. Hoang, B. Kalidasan, et al., “A Technical Review on Composite Phase Change Material Based Secondary Assisted Battery Thermal Management System for Electric Vehicles,” *Journal of Cleaner Production* 322 (2021): 129079.

28. V. V. Tyagi, K. Chopra, B. Kalidasan, et al., “Phase Change Material Based Advance Solar Thermal Energy Storage Systems for Building Heating and Cooling Applications: A Prospective Research Approach,” *Sustainable Energy Technologies and Assessments* 47 (2021): 101318.

29. B. Kalidasan, A. K. Pandey, S. Shahabuddin, M. Samykano, M. Thirugnanasambandam, and R. Saidur, “Phase Change Materials Integrated Solar Thermal Energy Systems: Global Trends and Current Practices in Experimental Approaches,” *Journal of Energy Storage* 27 (2020): 101118.

30. A. K. Pandey, M. S. Hossain, V. V. Tyagi, N. Abd Rahim, J. A. L. Selvaraj, and A. Sari, “Novel Approaches and Recent Developments on Potential Applications of Phase Change Materials in Solar Energy,” *Renewable and Sustainable Energy Reviews* 82 (2018): 281–323.

31. B. Kalidasan and A. K. Pandey, “Next Generation Phase Change Materials: State-of-the-Art Towards Sustainable Future,” *Progress in Materials Science* 148 (2025): 101380.

32. N. H. Solangi, N. M. Mubarak, R. R. Karri, et al., “MXene-Based Phase Change Materials for Solar Thermal Energy Storage,” *Energy Conversion and Management* 273 (2022): 116432.

33. X. Zhou, X. Hu, J. Yu, et al., “2D Layered Material-Based Van Der Waals Heterostructures for Optoelectronics,” *Advanced Functional Materials* 28, no. 14 (2018): 1706587.

34. F. Ezzah Ab Latif, A. Numan, N. M. Mubarak, et al., “Evolution of MXene and Its 2D Heterostructure in Electrochemical Sensor Applications,” *Coordination Chemistry Reviews* 471 (2022): 214755.

35. A. Sundaram, J. S. Ponraj, C. Wang, et al., “Engineering of 2D Transition Metal Carbides and Nitrides MXenes for Cancer Therapeutics and Diagnostics,” *Journal of Materials Chemistry B* 8, no. 23 (2020): 4990–5013.

36. S. K. Kailasa, D. J. Joshi, J. R. Koduru, and N. I. Malek, “Review on MXenes-Based Nanomaterials for Sustainable Opportunities in Energy Storage, Sensing and Electrocatalytic Reactions,” *Journal of Molecular Liquids* 342 (2021): 117524.

37. Y. Ma, M. Zou, W. Chen, et al., “A Structured Phase Change Material Integrated by MXene/AgNWs Modified Dual-Network and Polyethylene Glycol for Energy Storage and Thermal Management,” *Applied Energy* 349 (2023): 121658.

38. D. Gowthami, R. K. Sharma, and M. Khalid, “2D MXene Based Nanocomposites for Solar Driven Renewable Energy Storage Utilizing Binary Eutectic Phase Change Material,” *Journal of Molecular Liquids* 391 (2023): 123246.

39. N. Aslfattahi, R. Saidur, A. Arifutzzaman, et al., “Experimental Investigation of Energy Storage Properties and Thermal Conductivity of a Novel Organic Phase Change Material/MXene as a New Class of Nanocomposites,” *Journal of Energy Storage* 27 (2020): 101115.

40. A. A. Khan, S. M. Yahya, and M. A. Ali, “Synthesis and Characterization of Titania–MXene-Based Phase Change Material for Sustainable Thermal Energy Storage,” *Sustainability* 15, no. 1 (2022): 516.

41. B. Kalidasan, A. Pandey, R. Saidur, et al., “MXene-Based Eutectic Salt Hydrate Phase Change Material for Efficient Thermal Features, Corrosion Resistance & Photo-Thermal Energy Conversion,” *Materials Today Sustainability* 25 (2024): 100634.

42. D. Huang, Y. Chen, L. Zhang, et al., “Flexible Thermoregulatory Microcapsule/Polyurethane-MXene Composite Films With Multiple Thermal Management Functionalities and Excellent EMI Shielding Performance,” *Journal of Materials Science & Technology* 165 (2023): 27–38.

43. H. Yue, Y. Ou, J. Wang, et al., “$Ti_3C_2T_x$ MXene/Delignified Wood Supported Flame-Retardant Phase-Change Composites With Superior Solar-Thermal Conversion Efficiency and Highly Electromagnetic Interference Shielding for Efficient Thermal Management,” *Energy* 286 (2024): 129441.

44. H. Liu, R. Fu, X. Su, et al., “MXene Confined in Shape-Stabilized Phase Change Material Combining Enhanced Electromagnetic Interference Shielding and Thermal Management Capability,” *Composites Science and Technology* 210 (2021): 108835.

45. L. Li, Y. Cao, X. Liu, J. Wang, Y. Yang, and W. Wang, “Multifunctional MXene-Based Fireproof Electromagnetic Shielding Films With Exceptional Anisotropic Heat Dissipation Capability and Joule Heating Performance,” *ACS Applied Materials & Interfaces* 12, no. 24 (2020): 27350–27360.

46. Z. Cheng, G. Chang, B. Xue, et al., “Hierarchical Ni-Plated Melamine Sponge and MXene Film Synergistically Supported Phase Change Materials Towards Integrated Shape Stability, Thermal Management and Electromagnetic Interference Shielding,” *Journal of Materials Science & Technology* 132 (2023): 132–143.

47. L. Jiang, W. Zhang, R. Zhang, et al., “High Latent Heat Phase Change Materials Composites Based on MXene/Biomass-Derived Cellulose Nanocrystalline Aerogel for Solar-Thermal Energy Conversion and Storage,” *Ceramics International* 50, no. 10 (2024): 17428–17438.

48. M. M. Umair, Y. Zhang, S. Zhang, X. Jin, and B. Tang, “A Novel Flexible Phase Change Composite With Electro-Driven Shape Memory, Energy Conversion/Storage and Motion Sensing Properties,” *Journal of Materials Chemistry A* 7, no. 46 (2019): 26385–26392.

49. X. Min, B. Sun, S. Chen, et al., “A Textile-Based SnO_2 Ultra-Flexible Electrode for Lithium-Ion Batteries,” *Energy Storage Materials* 16 (2019): 597–606.

50. Y. Yue, N. Liu, W. Liu, et al., “3D Hybrid Porous MXene-Sponge Network and Its Application in Piezoresistive Sensor,” *Nano Energy* 50 (2018): 79–87.

51. Y. Shao, W. Hu, M. Gao, et al., “Flexible MXene-Coated Melamine Foam Based Phase Change Material Composites for Integrated Solar-Thermal Energy Conversion/Storage, Shape Memory and Thermal Therapy Functions,” *Composites, Part A: Applied Science and Manufacturing* 143 (2021): 106291.

52. W. Zuo, R. Li, C. Zhou, Y. Li, J. Xia, and J. Liu, “Battery-Supercapacitor Hybrid Devices: Recent Progress and Future Prospects,” *Advanced Science* 4, no. 7 (2017): 1600539.

53. X. Fan, L. Liu, X. Jin, W. Wang, S. Zhang, and B. Tang, “MXene $Ti_3C_2T_x$ for Phase Change Composite With Superior Photothermal Storage Capability,” *Journal of Materials Chemistry A* 7, no. 23 (2019): 14319–14327.

54. K. Zhao, Z. Guo, J. Wang, and H. Xie, “Enhancing Solar Photothermal Conversion and Energy Storage With Titanium Carbide (Ti_3C_2) MXene Nanosheets in Phase-Change Microcapsules,” *Journal of Colloid and Interface Science* 650 (2023): 1591–1604.

55. L. Tang, X. Zhao, C. Feng, et al., “Bacterial Cellulose/MXene Hybrid Aerogels for Photodriven Shape-Stabilized Composite Phase Change Materials,” *Solar Energy Materials and Solar Cells* 203 (2019): 110174.

56. D. Huang, Z. Wang, X. Sheng, and Y. Chen, “Bio-Based MXene Hybrid Aerogel/Paraffin Composite Phase Change Materials With Superior Photo and Electrical Responses Toward Solar Thermal Energy Storage,” *Solar Energy Materials and Solar Cells* 251 (2023): 112124.

57. Y. He, J. Wen, J. Huang, and L. Gan, “Multifunctional Enhancement Strategy for MXene-Based Fire Alarm Sensors via Interlocked ‘Brick/Mortar’ Structure of Dimension-Hybrid Nanoparticle System,” *Journal of Materials Research and Technology* 33 (2024): 8142–8150.

58. J. M. Jang, J. H. Kim, J. Lee, et al., “Gradient-Structured MXene/ZIF/CNT Hybrid Films for Largely Enhanced Electromagnetic Absorption in EMI Shielding,” *Chemical Engineering Journal* 503 (2024): 158691.

59. Y. Wu, C. Chen, F. Pan, X. Li, and W. Lu, “High-Entropy TiVNb-MoC_3T_x MXene Hybrid With Balanced Dielectric-Magnetic Loss for High-Efficient Electromagnetic Wave Absorption With Environmental Stability,” *Chemical Engineering Journal* 499 (2024): 156024.

60. X. Lu, H. Huang, X. Zhang, et al., “Novel Light-Driven and Electro-Driven Polyethylene Glycol/Two-Dimensional MXene Form-Stable Phase Change Material With Enhanced Thermal Conductivity and Electrical Conductivity for Thermal Energy Storage,” *Composites, Part B: Engineering* 177 (2019): 107372.

61. Z. Mo, P. Mo, M. Yi, et al., “$Ti_3C_2T_x$@Polyvinyl Alcohol Foam-Supported Phase Change Materials With Simultaneous Enhanced Thermal Conductivity and Solar-Thermal Conversion Performance,” *Solar Energy Materials and Solar Cells* 219 (2021): 110813.

62. Y. Luo, Y. Xie, H. Jiang, et al., “Flame-Retardant and Form-Stable Phase Change Composites Based on MXene With High Thermostability and Thermal Conductivity for Thermal Energy Storage,” *Chemical Engineering Journal* 420 (2021): 130466.

63. P. Lin, J. Xie, Y. He, et al., “MXene Aerogel-Based Phase Change Materials Toward Solar Energy Conversion,” *Solar Energy Materials and Solar Cells* 206 (2020): 110229.

64. H. Wu, X. Hu, X. Li, et al., “Large-Scale Fabrication of Flexible EPDM/MXene/PW Phase Change Composites With Excellent Light-to-Thermal Conversion Efficiency via Water-Assisted Melt Blending,” *Composites, Part A: Applied Science and Manufacturing* 152 (2022): 106713.

65. X. Liu, F. Lin, X. Zhang, et al., “Paraffin/$Ti_3C_2T_x$ MXene@ Gelatin Aerogels Composite Phase-Change Materials With High Solar-Thermal Conversion Efficiency and Enhanced Thermal Conductivity for Thermal Energy Storage,” *Energy & Fuels* 35, no. 3 (2021): 2805–2814.

66. F. Wang, J. Guo, S. Li, et al., “Facile Self-Assembly Approach to Construct a Novel MXene-Decorated Nano-Sized Phase Change Material Emulsion for Thermal Energy Storage,” *Ceramics International* 48, no. 4 (2022): 4722–4731.

67. Y. Bai and S. Wang, “MXene/d-Mannitol Aerogel Phase Change Material Composites for Medium-Temperature Energy Storage and Solar-Thermal Conversion,” *Journal of Energy Storage* 67 (2023): 107498.

68. N. H. Solangi, N. M. Mubarak, R. R. Karri, S. A. Mazari, S. K. Kailasa, and A. Alfantazi, “Applications of Advanced MXene-Based Composite Membranes for Sustainable Water Desalination,” *Chemosphere* 314 (2023): 137643.

69. Y. Wei, Z. Xie, and H. Qi, “Superhydrophobic-Superoleophilic SiC Membranes With Micro-Nano Hierarchical Structures for High-Efficient Water-in-Oil Emulsion Separation,” *Journal of Membrane Science* 601 (2020): 117842.

70. L. Chen, G. Shi, J. Shen, et al., “Ion Sieving in Graphene Oxide Membranes via Cationic Control of Interlayer Spacing,” *Nature* 550, no. 7676 (2017): 380–383.

71. L. Ries, E. Petit, T. Michel, et al., “Enhanced Sieving From Exfoliated MoS_2 Membranes via Covalent Functionalization,” *Nature Materials* 18, no. 10 (2019): 1112–1117.

72. M. Jian, R. Qiu, Y. Xia, et al., “Ultrathin Water-Stable Metal-Organic Framework Membranes for Ion Separation,” *Science Advances* 6, no. 23 (2020): eaay3998.

73. I. Hussain, T. Hussain, S. Yang, et al., “Integration of CuO Nanosheets to Zn-Ni-Co Oxide Nanowire Arrays for Energy Storage Applications,” *Chemical Engineering Journal* 413 (2020): 127570.

74. S. Vafakhah, Z. Beiramzadeh, M. Saeedikhani, and H. Y. Yang, “A Review on Free-Standing Electrodes for Energy-Effective Desalination: Recent Advances and Perspectives in Capacitive Deionization,” *Desalination* 493 (2020): 114662.

75. S. K. Hwang, S.-M. Kang, M. Rethinasabapathy, C. Roh, and Y. S. Huh, “MXene: An Emerging Two-Dimensional Layered Material for Removal of Radioactive Pollutants,” *Chemical Engineering Journal* 397 (2020): 125428.

76. R. M. Ronchi, J. T. Arantes, and S. F. Santos, “Synthesis, Structure, Properties and Applications of MXenes: Current Status and Perspectives,” *Ceramics International* 45, no. 15 (2019): 18167–18188.

77. M. Sajid, “MXenes: Are They Emerging Materials for Analytical Chemistry Applications?—A Review,” *Analytica Chimica Acta* 1143 (2021): 267–280.

78. M. Jeon, B.-M. Jun, S. Kim, et al., “A Review on MXene-Based Nanomaterials as Adsorbents in Aqueous Solution,” *Chemosphere* 261 (2020): 127781.

79. J. Jang, A. Shahzad, S. H. Woo, and D. S. Lee, “Magnetic $Ti_3C_2T_x$ (MXene) for Diclofenac Degradation via the Ultraviolet/Chlorine Advanced Oxidation Process,” *Environmental Research* 182 (2020): 108990.

80. A. Shahzad, K. Rasool, W. Miran, et al., “Two-Dimensional $Ti_3C_2T_x$ MXene Nanosheets for Efficient Copper Removal From Water,” *ACS Sustainable Chemistry & Engineering* 5, no. 12 (2017): 11481–11488.

81. Y. A. J. Al-Hamadani, B.-M. Jun, M. Yoon, et al., “Applications of MXene-Based Membranes in Water Purification: A Review,” *Chemosphere* 254 (2020): 126821.

82. K. Zhou, K. Gong, C. Wang, M. Zhou, and J. Xiao, “Construction of Ti_3C_2 MXene Based Fire Resistance Nanocoating on Flexible Polyurethane Foam for Highly Efficient Photothermal Conversion and Solar Water Desalination,” *Journal of Colloid and Interface Science* 630 (2023): 343–354.

83. Q. Zhang, G. Yi, Z. Fu, H. Yu, S. Chen, and X. Quan, “Vertically Aligned Janus MXene-Based Aerogels for Solar Desalination With High Efficiency and Salt Resistance,” *ACS Nano* 13, no. 11 (2019): 13196–13207.

84. P.-L. Wang, W. Zhang, Q. Yuan, T. Mai, M. Y. Qi, and M. G. Ma, “3D Janus Structure MXene/Cellulose Nanofibers/Luffa Aerogels With Superb Mechanical Strength and High-Efficiency Desalination for Solar-Driven Interfacial Evaporation,” *Journal of Colloid and Interface Science* 645 (2023): 306–318.

85. R. Xu, H. Cui, N. Wei, et al., “Advanced Design of Bimetal Sulfide/V_2CT_x MXene Photothermal Nanocomposites for Integrated Solar Steam Generation, Electricity Generation, and Water Purification,” *Desalination* 570 (2024): 117094.

86. H. Gao, N. Bing, Z. Bao, H. Xie, and W. Yu, “Sandwich-Structured MXene/Wood Aerogel With Waste Heat Utilization for Continuous Desalination,” *Chemical Engineering Journal* 454 (2023): 140362.

87. J. Zhao, Y. Yang, C. Yang, et al., “A Hydrophobic Surface Enabled Salt-Blocking 2D Ti_3C_2 MXene Membrane for Efficient and Stable Solar Desalination,” *Journal of Materials Chemistry A* 6, no. 33 (2018): 16196–16204.

88. M. Ding, W. Ma, P. Liu, J. Yang, K. Lan, and D. Xu, "Creating Aligned Porous Structure With Cobweb-Like Cellulose Nanofibrils in MXene Composite Aerogel for Solar-Thermal Desalination and Humidity Response," *Chemical Engineering Journal* 459 (2023): 141604.

89. M. Berkani, A. Smaali, F. Almomani, and Y. Vasseghian, "Recent Advances in MXene-Based Nanomaterials for Desalination at Water Interfaces," *Environmental Research* 203 (2022): 111845.

90. S. Abdolhosseinzadeh, X. Jiang, H. Zhang, J. Qiu, and C. Zhang, "Perspectives on Solution Processing of Two-Dimensional MXenes," *Materials Today* 48 (2021): 214–240.

91. D.-E. Lee, S. Moru, W.-K. Jo, and S. Tonda, "Dual-Cocatalyst-Promoted Photocatalytic Treatment of Persistent Waterborne Pollutants via In Situ MXene-Derived TiO_2/Ti_3C_2 Hybrids With Plasmonic Ag Nanoparticles," *Separation and Purification Technology* 352 (2025): 128261.

92. T. N. Jahangir, T. A. Kandiel, W. Fatima, M. A. Abdalmwla, A. Al-Ahmed, and A. Y. Ahmed, "Insights Into the Role of Co_3O_4/Ti_3C_2 MXene Hybrid Material in Photoelectrochemical Water Oxidation over $BiVO_4$ Photoanode," *Journal of Environmental Chemical Engineering* 12, no. 3 (2024): 113058.

93. K. Rasool, R. P. Pandey, P. A. Rasheed, S. Buczek, Y. Gogotsi, and K. A. Mahmoud, "Water Treatment and Environmental Remediation Applications of Two-Dimensional Metal Carbides (MXenes)," *Materials Today* 30 (2019): 80–102.

94. W. Xia, H. Cheng, S. Zhou, N. Yu, and H. Hu, "Synergy of Copper Selenide/MXenes Composite With Enhanced Solar-Driven Water Evaporation and Seawater Desalination," *Journal of Colloid and Interface Science* 625 (2022): 289–296.

95. Q. Zhang, S. Chen, Z. Fu, H. Yu, and X. Quan, "Temperature-Difference-Induced Electricity During Solar Desalination With Bilayer MXene-Based Monoliths," *Nano Energy* 76 (2020): 105060.

96. M. Pi, X. Wang, Z. Wang, and R. Ran, "Sustainable MXene/PDA Hydrogel With Core-Shell Structure Tailored for Highly Efficient Solar Evaporation and Long-Term Desalination," *Polymer* 230 (2021): 124075.

97. W. Xiao, J. Yan, S. Gao, et al., "Superhydrophobic MXene Based Fabric Composite for High Efficiency Solar Desalination," *Desalination* 524 (2022): 115475.

98. Z. Zheng, H. Liu, D. Wu, and X. Wang, "Polyimide/MXene Hybrid Aerogel-Based Phase-Change Composites for Solar-Driven Seawater Desalination," *Chemical Engineering Journal* 440 (2022): 135862.

99. D. Choi, Y. Lee, Z.-H. Lin, et al., "Recent Advances in Triboelectric Nanogenerators: From Technological Progress to Commercial Applications," *ACS Nano* 17, no. 12 (2023): 11087–11219.

100. Z. Li, Z. Li, J. Chang, and L. Chen, "MXene Based Flexible Materials for Energy Harvesting," *Materials Today Chemistry* 37 (2024): 101989.

101. G. Mohana Rani, K. S. Ranjith, S. M. Ghoreishian, et al., "Fabrication of MoS_2 Petals-Decorated PAN Fibers-Based Triboelectric Nanogenerator for Energy Harvesting and Smart Study Room Touch Sensor Applications," *Advanced Fiber Materials* 6 (2024): 1825–1838.

102. G. M. Rani, S. M. Ghoreishian, R. Umapathi, V. Vivekananthan, and Y. S. Huh, "A Biocompatible Triboelectric Nanogenerator-Based Edible Electronic Skin for Morse Code Transmitters and Smart Healthcare Applications," *Nano Energy* 128 (2024): 109899.

103. K. U. Kumar, S. Hajra, G. Mohana Rani, et al., "Revolutionizing Waste-to-Energy: Harnessing the Power of Triboelectric Nanogenerators," *Advanced Composites and Hybrid Materials* 7, no. 3 (2024): 91.

104. G. M. Sonu, G. M. Rani, D. Pathania, et al., "Agro-Waste to Sustainable Energy: A Green Strategy of Converting Agricultural Waste to Nano-Enabled Energy Applications," *Science of the Total Environment* 875 (2023): 162667.

105. G. M. Rani, C.-M. Wu, K. G. Motora, and R. Umapathi, "Waste-to-Energy: Utilization of Recycled Waste Materials to Fabricate Triboelectric Nanogenerator for Mechanical Energy Harvesting," *Journal of Cleaner Production* 363 (2022): 132532.

106. G. M. Rani, C.-M. Wu, K. G. Motora, R. Umapathi, and C. R. M. Jose, "Acoustic-Electric Conversion and Triboelectric Properties of Nature-Driven CF-CNT Based Triboelectric Nanogenerator for Mechanical and Sound Energy Harvesting," *Nano Energy* 108 (2023): 108211.

107. M. R. Gokana, C.-M. Wu, U. Reddicherla, and K. G. Motora, "Scalable Preparation of Ultrathin Porous Polyurethane Membrane-Based Triboelectric Nanogenerator for Mechanical Energy Harvesting," *Express Polymer Letters* 15 (2021): 1019–1031.

108. G. M. Rani, S. M. Ghoreishian, K. S. Ranjith, et al., "High Roughness Induced Pearl Necklace-Like ZIF-67@PAN Fiber-Based Triboelectric Nanogenerators for Mechanical Energy Harvesting," *Advanced Materials Technologies* 8, no. 19 (2023): 2300685.

109. X. Sun, L. Dong, Y. Liu, et al., "Biomimetic PVA-PVDF-Based Triboelectric Nanogenerator With MXene Doping for Self-Powered Water Sterilization," *Materials Today Nano* 24 (2023): 100410.

110. S. He, Y. Gui, Y. Wang, L. Cao, G. He, and C. Tang, "CuO/TiO_2/MXene-Based Sensor and SMS-TENG Array Integrated Inspection Robots for Self-Powered Ethanol Detection and Alarm at Room Temperature," *ACS Sensors* 9, no. 3 (2024): 1188–1198.

111. X. Tan, S. Wang, Z. You, J. Zheng, and Y. Liu, "High Performance Porous Triboelectric Nanogenerator Based on Silk Fibroin@MXene Composite Aerogel and PDMS Sponge," *ACS Materials Letters* 5, no. 7 (2023): 1929–1937.

112. S. Sardana, V. Sharma, K. G. Beepat, D. P. Sharma, A. K. Chawla, and A. Mahajan, "Flexible, Humidity- and Contamination-Resistant Superhydrophobic MXene-Based Electrospun Triboelectric Nanogenerators for Distributed Energy Harvesting Applications," *Nanoscale* 15, no. 47 (2023): 19369–19380.

113. J. Wang, Z. Xia, H. Yao, Q. Zhang, and H. Yang, "Self-Powered TENG With High Humidity Sensitivity From PVA Film Modified by LiCl and MXene," *ACS Applied Materials & Interfaces* 15, no. 40 (2023): 47208–47220.

114. B. Wicklein, G. Valurouthu, H. Yoon, et al., "Influence of MXene Composition on Triboelectricity of MXene-Alginate Nanocomposites," *ACS Applied Materials & Interfaces* 16, no. 18 (2024): 23948–23959.

115. Y. He, L. Zhao, X. Guo, X. Yang, B. Luo, and M. Liu, "Electrostatic-Driven Self-Assembled Chitin Nanocrystals (ChNCs)/MXene Films for Triboelectric Nanogenerator," *Chemical Engineering Journal* 485 (2024): 149949.

116. B.-Y. Lai, S.-N. Lai, H.-Y. Lin, and J. M. Wu, "Silane-Modified MXene/PVA Hydrogel for Enhanced Streaming Vibration Potential in High-Performance Flexible Triboelectric Nanogenerators," *Nano Energy* 125 (2024): 109554.

117. J. Yun, J. Park, M. Ryoo, N. Kitchamsetti, T. S. Goh, and D. Kim, "Piezo-Triboelectric Hybridized Nanogenerator Embedding MXene Based Bifunctional Conductive Filler in Polymer Matrix for Boosting Electrical Power," *Nano Energy* 105 (2023): 108018.

118. Y. Zong, R. Wang, S. Xu, R. Zhang, and Z. Zhang, "Flexible Piezoelectric Nanogenerator Based on Cellulose Nanofibril/MXene Composite Aerogels for Low-Frequency Energy Harvesting," *ACS Applied Nano Materials* 6, no. 10 (2023): 9021–9031.

119. Z. Wang, C. Hao, M. Cai, J. Cui, Y. Zheng, and C. Xue, "A High-output PDMS-MXene/Gelatin Triboelectric Nanogenerator With the Petal Surface-Microstructure," *Nano Research* 17, no. 5 (2024): 4151–4162.

120. S. He, Y. Gui, Y. Wang, and J. Yang, "A Self-Powered B-$Ni(OH)_2$/MXene Based Ethanol Sensor Driven by an Enhanced Triboelectric Nanogenerator Based on β-$Ni(OH)_2$@PVDF at Room Temperature," *Nano Energy* 107 (2023): 108132.

121. G. Kim, J. Yun, and D. Kim, "Enhancing Power Generation With a $SnSe_2$-MXene Composite in a Piezo-Triboelectric Hybrid Nanogenerator for Autonomous Energy Applications," *Nano Energy* 126 (2024): 109678.

122. W. Zhang, P.-L. Wang, X.-X. Ji, et al., "Ultrastretchable and Adhesive MXene-Based Hydrogel for High-Performance Strain Sensing and Self-Powered Application," *Composites, Part A: Applied Science and Manufacturing* 177 (2024): 107957.

123. C. Xu, Z. Li, T. Hang, et al., "Multi-Scale MXene/Silver Nanowire Composite Foams With Double Conductive Networks for Multifunctional Integration," *Advanced Science* 11 (2024): 2403551.

124. W. Jiang, J. Liu, H. Zhang, et al., "Low-Temperature Resistant Hydrogel With Inkjet-Printed MXene on Microspine Surface for Pressure Sensing and Triboelectric Energy Harvesting," *Chemical Engineering Journal* 483 (2024): 149117.

125. K. Gopalram, A. Kapoor, P. S. Kumar, et al., "MXenes and MXene-Based Materials for Removal and Detection of Water Contaminants: A Review," *Industrial & Engineering Chemistry Research* 62, no. 17 (2023): 6559–6583.

126. R. Umapathi, S. M. Ghoreishian, G. M. Rani, Y. Cho, and Y. S. Huh, "Review—Emerging Trends in the Development of Electrochemical Devices for the On-Site Detection of Food Contaminants," *ECS Sensors Plus* 1, no. 4 (2022): 044601.

127. R. Umapathi, S. M. Ghoreishian, S. Sonwal, G. M. Rani, and Y. S. Huh, "Portable Electrochemical Sensing Methodologies for On-Site Detection of Pesticide Residues in Fruits and Vegetables," *Coordination Chemistry Reviews* 453 (2022): 214305.

128. R. Umapathi, G. M. Rani, E. Kim, S. Y. Park, Y. Cho, and Y. S. Huh, "Sowing Kernels for Food Safety: Importance of Rapid On-Site Detction of Pesticide Residues in Agricultural Foods," *Food Frontiers* 3, no. 4 (2022): 666–676.

129. M. A. A. M. Abdah, H. T. A. Awan, M. Mehar, et al., "Advancements in MXene-Polymer Composites for High-Performance Supercapacitor Applications," *Journal of Energy Storage* 63 (2023): 106942.

130. C. Venkateswara Raju, C. H. Cho, G. Mohana Rani, et al., "Emerging Insights into the Use of Carbon-Based Nanomaterials for the Electrochemical Detection of Heavy Metal Ions," *Coordination Chemistry Reviews* 476 (2023): 214920.

131. R. Umapathi, C. Venkateswara Raju, S. Majid Ghoreishian, et al., "Recent Advances in the Use of Graphitic Carbon Nitride-Based Composites for the Electrochemical Detection of Hazardous Contaminants," *Coordination Chemistry Reviews* 470 (2022): 214708.

132. A. T. E. Vilian, R. Umapathi, S.-K. Hwang, Y. S. Huh, and Y. K. Han, "Pd–Cu Nanospheres Supported on Mo_2C for the Electrochemical Sensing of Nitrites," *Journal of Hazardous Materials* 408 (2021): 124914.

133. R. Umapathi, S. Sonwal, M. J. Lee, et al., "Colorimetric Based On-Site Sensing Strategies for the Rapid Detection of Pesticides in Agricultural Foods: New Horizons, Perspectives, and Challenges," *Coordination Chemistry Reviews* 446 (2021): 214061.

134. R. Umapathi, B. Park, S. Sonwal, et al., "Advances in Optical-Sensing Strategies for the On-Site Detection of Pesticides in Agricultural Foods," *Trends in Food Science & Technology* 119 (2022): 69–89.

135. D. Liao, Z. Liu, R. Huang, J. Yu, and X. Jiang, "In-Situ Construction of Porous Carbon on Embedded N-Doped MXene Nanosheets Composite for Simultaneous Determination of 4-Aminophenol and Acetaminophen," *Microchemical Journal* 175 (2022): 107067.

136. Y. Wang, P. Zhao, B. Gao, et al., "Self-Reduction of Bimetallic Nanoparticles on Flexible MXene-Graphene Electrodes for Simultaneous Detection of Ascorbic Acid, Dopamine, and Uric Acid," *Microchemical Journal* 185 (2023): 108177.

137. S. Elumalai, V. Mani, N. Jeromiyas, V. K. Ponnusamy, and M. Yoshimura, "A Composite Film Prepared From Titanium Carbide $Ti_3C_2T_x$ (MXene) and Gold Nanoparticles for Voltammetric Determination of Uric Acid and Folic Acid," *Microchimica Acta* 187 (2020): 33.

138. S. Chen, M. Shi, Q. Xu, et al., "$Ti_3C_2T_x$ MXene/Nitrogen-Doped Reduced Graphene Oxide Composite: A High-Performance Electrochemical Sensing Platform for Adrenaline Detection," *Nanotechnology* 32, no. 26 (2021): 265501.

139. A. Mohan, N. Shabana, M. Ankitha, and P. Abdul Rasheed, "Electrochemical Deposition of Prussian Blue on Nb_2CT MXene Modified Carbon Cloth for the Non-Enzymatic Electrochemical Detection of Hydrogen Peroxide," *Microchemical Journal* 185 (2023): 108301.

140. J. Yang, C. Deng, W. Zhong, et al., "Electrochemical Activation of Oxygen Vacancy-Rich TiO_2@MXene as High-Performance Electrochemical Sensing Platform for Detecting Imidacloprid in Fruits and Vegetables," *Microchimica Acta* 190, no. 4 (2023): 146.

141. M. P. Thukkaram, A. Chakravorty, A. A. Mini, K. Ramesh, A. N. Grace, and V. Raghavan, "Titanium Carbide MXene and V_2O_5 Composite-Based Electrochemical Sensor for Detection of Bisphenol A," *Microchemical Journal* 193 (2023): 109004.

142. Y. Chen, P. Zhao, Y. Liang, et al., "A Sensitive Electrochemical Sensor Based on 3D Porous Melamine-Doped rGO/MXene Composite Aerogel for the Detection of Heavy Metal Ions in the Environment," *Talanta* 256 (2023): 124294.

143. Z. Shi, Z. Wang, K. Li, Y. Wang, Z. Li, and Z. Zhu, "MXene Fibers-Based Molecularly Imprinted Disposable Electrochemical Sensor for Sensitive and Selective Detection of Hydrocortisone," *Talanta* 266 (2024): 125100.

144. J. Paul and J. Kim, "Reticular Synthesis of a Conductive Composite Derived From Metal-Organic Framework and MXene for the Electrochemical Detection of Dopamine," *Applied Surface Science* 613 (2023): 156103.

145. Q.-F. Li, X. Chen, H. Wang, M. Liu, and H. L. Peng, "Pt/MXene-Based Flexible Wearable Non-Enzymatic Electrochemical Sensor for Continuous Glucose Detection in Sweat," *ACS Applied Materials & Interfaces* 15, no. 10 (2023): 13290–13298.

146. J. Chen, S. Li, Y. Chen, J. Yang, J. Dong, and X. Lu, "L-Cysteine-Terminated Triangular Silver Nanoplates/MXene Nanosheets Are Used as Electrochemical Biosensors for Efficiently Detecting 5-Hydroxytryptamine," *Analytical Chemistry* 93, no. 49 (2021): 16655–16663.

147. L. Yu, J. Chang, X. Zhuang, H. Li, T. Hou, and F. Li, "Two-Dimensional Cobalt-Doped Ti_3C_2 MXene Nanozyme-Mediated Homogeneous Electrochemical Strategy for Pesticides Assay Based on In Situ Generation of Electroactive Substances," *Analytical Chemistry* 94, no. 8 (2022): 3669–3676.

148. F. Gao, W. Hong, B. Xu, et al., "MXene Nanosheets Decorated With Pt Nanostructures for the Selective Electrochemical Detection of Quercetin," *ACS Applied Nano Materials* 6, no. 8 (2023): 6869–6878.

149. S. G. Chavan, P. R. Rathod, A. Koyappayil, A. Go, and M. H. Lee, "'Two-step' Signal Amplification for Ultrasensitive Detection of Dopamine in Human Serum Sample Using $Ti_3C_2T_x$-MXene," *Sensors and Actuators B: Chemical* 404 (2024): 135308.

150. H. Liu, W. Qin, X. Li, et al., "Molecularly Imprinted Electrochemical Sensors Based on $Ti_3C_2T_x$-MXene and Graphene Composite Modifications for Ultrasensitive Cortisol Detection," *Analytical Chemistry* 95, no. 44 (2023): 16079–16088.

151. M. Ankitha, N. Shabana, and P. A. Rasheed, "A Novel ReS_2–Nb_2CT_x Composite as a Sensing Platform for Ultrasensitive and Selective Electrochemical Detection of Dipyramidole From Human Serum," *Graphene and 2D Materials* 8, no. 1 (2023): 27–37.

152. K. S. Ranjith, A. T. Ezhil Vilian, S. M. Ghoreishian, et al., "Hybridized 1D–2D $MnMoO_4$–MXene Nanocomposites as

High-Performing Electrochemical Sensing Platform for the Sensitive Detection of Dihydroxybenzene Isomers in Wastewater Samples," *Journal of Hazardous Materials* 421 (2022): 126775.

153. K. S. Ranjith, A. T. E. Vilian, S. M. Ghoreishian, R. Umapathi, Y. S. Huh, and Y. K. Han, "An Ultrasensitive Electrochemical Sensing Platform for Rapid Detection of Rutin With a Hybridized 2D-1D MXene-FeWO$_4$ Nanocomposite," *Sensors and Actuators B: Chemical* 344 (2021): 130202.

154. R. Amna, K. Ali, and S. M. Alhassan, "Computational Fluid Dynamics Analysis of Mercury Adsorption by Inverse-Vulcanized Porous Sulfur Copolymers," *Industrial & Engineering Chemistry Research* 62, no. 31 (2023): 12277–12290.

155. Y. Wu, X. Li, H. Zhao, et al., "Recent Advances in Transition Metal Carbides and Nitrides (MXenes): Characteristics, Environmental Remediation and Challenges," *Chemical Engineering Journal* 418 (2021): 129296.

156. D. Durgalakshmi, S. Rajendran, and M. Naushad, "Current Role of Nanomaterials in Environmental Remediation," in *Advanced Nanostructured Materials for Environmental Remediation* (Vol. 25), ed. M. Naushad (Springer Nature Switzerland AG, 2019), 1–20.

157. K. K. Singh, "Role of Nanotechnology and Nanomaterials for Water Treatment and Environmental Remediation," *International Journal of New Chemistry* 9, no. 3 (2022): 165–190.

158. X. Li, Z. Huang, C. E. Shuck, G. Liang, Y. Gogotsi, and C. Zhi, "MXene Chemistry, Electrochemistry and Energy Storage Applications," *Nature Reviews Chemistry* 6, no. 6 (2022): 389–404.

159. X. Chen, Y. Zhao, L. Li, et al., "MXene/Polymer Nanocomposites: Preparation, Properties, and Applications," *Polymer Reviews* 61, no. 1 (2021): 80–115.

160. A. VahidMohammadi, J. Rosen, and Y. Gogotsi, "The World of Two-Dimensional Carbides and Nitrides (MXenes)," *Science* 372, no. 6547 (2021): eabf1581.

161. A. Rosenkranz, M. C. Righi, A. V. Sumant, B. Anasori, and V. N. Mochalin, "Perspectives of 2D MXene Tribology," *Advanced Materials* 35, no. 5 (2023): 2207757.

162. P. Liu, H. Liu, T. Zhang, et al., "$Ti_3C_2T_x$ Quantum Dot-Modified $Ti_3C_2T_x$ Nanosheets Freestanding Films for Flexible Solid-State Pseudocapacitors," *Chemical Engineering Journal* 477 (2023): 146913.

163. I. Raheem, N. M. Mubarak, R. R. Karri, et al., "Rapid Growth of MXene-Based Membranes for Sustainable Environmental Pollution Remediation," *Chemosphere* 311 (2023): 137056.

164. L. Chen, M. Wakeel, T. Ul Haq, N. S. Alharbi, C. Chen, and X. Ren, "Recent Progress in Environmental Remediation, Colloidal Behavior and Biological Effects of MXene: A Review," *Environmental Science: Nano* 9, no. 9 (2022): 3168–3205.

165. A. S. Jatoi, N. M. Mubarak, Z. Hashmi, et al., "New Insights Into MXene Applications for Sustainable Environmental Remediation," *Chemosphere* 313 (2023): 137497.

166. S. Yu, H. Tang, D. Zhang, et al., "MXenes as Emerging Nanomaterials in Water Purification and Environmental Remediation," *Science of the Total Environment* 811 (2022): 152280.

167. J. A. Kumar, P. Prakash, T. Krithiga, et al., "Methods of Synthesis, Characteristics, and Environmental Applications of MXene: A Comprehensive Review," *Chemosphere* 286 (2022): 131607.

168. Y. Gao, Y. Dong, S. Yang, et al., "Size-Dependent Photothermal Antibacterial Activity of $Ti_3C_2T_x$ MXene Nanosheets Against Methicillin-Resistant *Staphylococcus aureus*," *Journal of Colloid and Interface Science* 617 (2022): 533–541.

169. K. Saravanakumar, K. Yun, V. Maheskumar, Y. Yea, G. Jagan, and C. M. Park, "Construction of Novel In_2S_3/Ti_3C_2 MXene Quantum Dots/$SmFeO_3$ Z-Scheme Heterojunctions for Efficient Photocatalytic Removal of Sulfamethoxazole and 4-Chlorophenol: Degradation Pathways and Mechanism Insights," *Chemical Engineering Journal* 451 (2023): 138933.

170. J. Y. Chin, A. L. Ahmad, and S. C. Low, "Evolution of Photocatalytic Membrane for Antibiotics Degradation: Perspectives and Insights for Sustainable Environmental Remediation," *Journal of Water Process Engineering* 51 (2023): 103342.

171. S. Rana, A. Kumar, P. Dhiman, G. T. Mola, G. Sharma, and C. W. Lai, "Recent Advances in Photocatalytic Removal of Sulfonamide Pollutants From Waste Water by Semiconductor Heterojunctions: A Review," *Materials Today Chemistry* 30 (2023): 101603.

172. M. Khatami, P. Iravani, G. Jamalipour Soufi, and S. Iravani, "MXenes for Antimicrobial and Antiviral Applications: Recent Advances," *Materials Technology* 37, no. 11 (2022): 1890–1905.

173. A. Shahzad, K. Rasool, M. Nawaz, et al., "Heterostructural $TiO_2/Ti_3C_2T_x$ (MXene) for Photocatalytic Degradation of Antiepileptic Drug Carbamazepine," *Chemical Engineering Journal* 349 (2018): 748–755.

174. A. Singh, S. Gupta, K. Kumari, et al., "MXene-Polymer Nanocomposites for Biomedical Applications," in *MXene Nanocomposites* (CRC Press, 2023), 197–226.

175. A. Lekshmi, R. Rejithamol, A. Santhy, et al., "Surface Terminations and Surface Functionalization Strategies of MXenes," in *MXene Reinforced Polymer Composites: Fabrication, Characterization and Applications*, ed. K. Deshmukh (Scrivener Publishing, 2024), 71–106.

176. S. Sukidpaneenid, C. Chawengkijwanich, C. Pokhum, T. Isobe, P. Opaprakasit, and P. Sreearunothai, "Multi-Function Adsorbent-Photocatalyst MXene-TiO_2 Composites for Removal of Enrofloxacin Antibiotic From Water," *Journal of Environmental Sciences* 124 (2023): 414–428.

177. F. Wang, Z. Bian, W. Zhang, L. Zheng, Y. Zhang, and H. Wang, "Fluorine-Free MXene Activate Peroxymonosulfate to Remove Tetracyclic Antibiotics," *Separation and Purification Technology* 314 (2023): 123549.

178. M. Faheem, A. Riaz, M. Alam, et al., "2D Nanostructured MXene-Based Silver Nanoparticles for Photocatalytic Degradation of Safranin Dye," *Catalysts* 14, no. 3 (2024): 201.

179. S. M. Albukhari, M. Abdel Salam, and A. M. M. Aldawsari, "Removal of Malachite Green Dye From Water Using MXene (Ti_3C_2) Nanosheets," *Sustainability* 14, no. 10 (2022): 5996.

180. H. Shi, H. Wang, E. Zhang, et al., "Boosted Photocatalytic Performance for Antibiotics Removal With $Ag/PW_{12}/TiO_2$ Composite: Degradation Pathways and Toxicity Assessment," *Molecules* 28, no. 19 (2023): 6831.

181. Z. Bo, Z. Huang, C. Xu, et al., "Anion-Kinetics-Selective Graphene Anode and Cation-Energy-Selective MXene Cathode for High-Performance Capacitive Deionization," *Energy Storage Materials* 50 (2022): 395–406.

182. T. Lv, F. Wu, Z. Zhang, et al., "$TiVCT_x$ MXene/Graphene Nanosheet-Based Aerogels for Removal of Organic Contaminants From Wastewater," *ACS Applied Nano Materials* 7, no. 7 (2024): 7312–7326.

183. C. Hao, G. Li, G. Wang, W. Chen, and S. Wang, "Preparation of Acrylic Acid Modified Alkalized MXene Adsorbent and Study on Its Dye Adsorption Performance," *Colloids and Surfaces, A: Physicochemical and Engineering Aspects* 632 (2022): 127730.

184. K. Ali, H. Raza, M. Malik, S. Shamsah, R. Amna, and A. Sarfraz, "To Study the Effect of $LiMn_2O_4$, Nanofibers of $LiMn_2O_4$, and Graphene/Polyaniline/Carbon Nanotube as Electrode Materials in the Fuel Cell," *Journal of New Materials for Electrochemical Systems* 23, no. 1 (2020): 1–6.

185. D. Park, S.-N. Nam, B. Jung, et al., "Removal of Selected Contaminants of Dyes and Pharmaceuticals Using MXene-Based

Nanoadsorbents: A Review," *Separation and Purification Technology* 341 (2024): 126864.

186. R. Amna and K. Ali, "Molecularly Imprinted Hydrogel Sensor for Proteins," *Journal of Dispersion Science and Technology* 45 (2023): 1086–1095.

187. N. Li, T.-J. Lou, W. Wang, et al., "MXene-PANI/PES Composite Ultrafiltration Membranes With Conductive Properties for Anti-Fouling and Dye Removal," *Journal of Membrane Science* 668 (2023): 121271.

188. A. M. M. Aldawsari, "Facile Preparation of Two-Dimensional MXenes Nanomaterials and their Application for Environmental Remediation" (Diss., King Abdulaziz University, 2022).

189. H. Shi, "Industrial Wastewater-Types, Amounts and Effects," *Point Sources of Pollution: Local Effects and It's Control* 1 (2009): 191–194, 203.

190. T. G. Ambaye, M. Vaccari, E. D. van Hullebusch, A. Amrane, and S. Rtimi, "Mechanisms and Adsorption Capacities of Biochar for the Removal of Organic and Inorganic Pollutants From Industrial Wastewater," *International Journal of Environmental Science and Technology* 18, no. 10 (2021): 3273–3294.

191. S. Garg, Z. Z. Chowdhury, A. N. M. Faisal, et al., "Impact of Industrial Wastewater on Environment and Human Health," in *Advanced Industrial Wastewater Treatment and Reclamation of Water: Comparative Study of Water Pollution Index During Pre-Industrial, Industrial Period and Prospect of Wastewater Treatment for Water Resource Conservation*, ed. S. Roy (Springer Nature, 2022), 197–209.

192. A. I. Adetunji and A. O. Olaniran, "Treatment of Industrial Oily Wastewater by Advanced Technologies: A Review," *Applied Water Science* 11, no. 6 (2021): 98.

193. G. Palani, A. Arputhalatha, K. Kannan, et al., "Current Trends in the Application of Nanomaterials for the Removal of Pollutants From Industrial Wastewater Treatment—A Review," *Molecules* 26, no. 9 (2021): 2799.

194. K. R. G. Lim, M. Shekhirev, B. C. Wyatt, B. Anasori, Y. Gogotsi, and Z. W. Seh, "Fundamentals of MXene Synthesis," *Nature Synthesis* 1, no. 8 (2022): 601–614.

195. X. Zhan, C. Si, J. Zhou, and Z. Sun, "MXene and MXene-Based Composites: Synthesis, Properties and Environment-Related Applications," *Nanoscale Horizons* 5, no. 2 (2020): 235–258.

196. X. Yang, Y. Liu, S. Hu, et al., "Construction of Fe_3O_4@MXene Composite Nanofiltration Membrane for Heavy Metal Ions Removal From Wastewater," *Polymers for Advanced Technologies* 32, no. 3 (2021): 1000–1010.

197. D. Gan, Q. Huang, J. Dou, et al., "Bioinspired Functionalization of MXenes ($Ti_3C_2T_x$) With Amino Acids for Efficient Removal of Heavy Metal Ions," *Applied Surface Science* 504 (2020): 144603.

198. Y. Sheth, S. Dharaskar, V. Chaudhary, M. Khalid, and R. Walvekar, "Prospects of Titanium Carbide-Based MXene in Heavy Metal Ion and Radionuclide Adsorption for Wastewater Remediation: A Review," *Chemosphere* 293 (2022): 133563.

199. P. Zhang, L. Wang, K. Du, et al., "Effective Removal of U(VI) and Eu(III) by Carboxyl Functionalized MXene Nanosheets," *Journal of Hazardous Materials* 396 (2020): 122731.

200. A. Shahzad, M. Nawaz, M. Moztahida, et al., "$Ti_3C_2T_x$ MXene Core-Shell Spheres for Ultrahigh Removal of Mercuric Ions," *Chemical Engineering Journal* 368 (2019): 400–408.

201. Y. Feng, H. Wang, J. Xu, et al., "Fabrication of MXene/PEI Functionalized Sodium Alginate Aerogel and Its Excellent Adsorption Behavior for Cr(VI) and Congo Red From Aqueous Solution," *Journal of Hazardous Materials* 416 (2021): 125777.

202. S. Wang, F. Wang, Y. Jin, et al., "Removal of Heavy Metal Cations and Co-Existing Anions in Simulated Wastewater by Two Separated Hydroxylated MXene Membranes Under an External Voltage," *Journal of Membrane Science* 638 (2021): 119697.

203. X. Long, G.-Q. Zhao, Y. Zheng, et al., "A Precise Pyromellitic Acid Grafting Prepared Multifunctional MXene Membranes for Efficient Oil-in-Water Emulsion Separation and Heavy Metal Ions Removal," *Chemical Engineering Journal* 472 (2023): 144904.

204. C. E. Ren, M. Q. Zhao, T. Makaryan, et al., "Porous Two-Dimensional Transition Metal Carbide (MXene) Flakes for High-Performance Li-Ion Storage," *ChemElectroChem* 3, no. 5 (2016): 689–693.

205. D. Wang, D. Zhang, P. Li, Z. Yang, Q. Mi, and L. Yu, "Electrospinning of Flexible Poly(Vinyl Alcohol)/MXene Nanofiber-Based Humidity Sensor Self-Powered by Monolayer Molybdenum Diselenide Piezoelectric Nanogenerator," *Nano-Micro Letters* 13 (2021): 57.

206. Y. Liu, D. Wang, C. Zhang, et al., "Compressible and Lightweight MXene/Carbon Nanofiber Aerogel With 'Layer-Strut' Bracing Microscopic Architecture for Efficient Energy Storage," *Advanced Fiber Materials* 4, no. 4 (2022): 820–831.

207. M. Ren, Z. Sun, M. Zhang, et al., "A High-Performance Wearable Pressure Sensor Based on an MXene/PVP Composite Nanofiber Membrane for Health Monitoring," *Nanoscale Advances* 4, no. 18 (2022): 3987–3995.

208. S. Cheng, S. Zhao, H. Guo, et al., "High-Efficiency Removal of Lead/Cadmium From Wastewater by MgO Modified Biochar Derived From Crofton Weed," *Bioresource Technology* 343 (2022): 126081.

209. I. Mahar, F. K. Mahar, N. Mahar, et al., "Fabrication and Characterization of MXene/Carbon Composite-Based Nanofibers (MXene/CNFs) Membrane: An Efficient Adsorbent Material for Removal of Pb^{+2} and As^{+3} Ions From Water," *Chemical Engineering Research and Design* 191 (2023): 462–471.

210. M. A. Islam, M. J. Angove, and D. W. Morton, "Recent Innovative Research on Chromium (VI) Adsorption Mechanism," *Environmental Nanotechnology, Monitoring & Management* 12 (2019): 100267.

211. U. A. Asif, K. Mahmood, S. R. Naqvi, M. T. Mehran, and T. Noor, "Development of High-Capacity Surface-Engineered MXene Composite for Heavy Metal Cr(VI) Removal From Industrial Wastewater," *Chemosphere* 326 (2023): 138448.

212. S. Fletcher, A. Miranda, J. Paiva, M. J. Benoliel, and C. M. M. Almeida, "Optimization and In-House Validation of the TDA-AAS Method for Mercury Control in Water and Wastewater Treatment Plant Sludges," *Analytical Methods* 12, no. 45 (2020): 5503–5513.

213. N. Ngatijo, D. I. Permatasari, F. Farid, et al., "Decontamination of Mercury From Mined Soil Using Magnetite Functionalized Quaternary Ammonium Silica (Fe_3O_4/SAK)," *Jurnal Presipitasi: Media Komunikasi dan Pengembangan Teknik Lingkungan* 18, no. 1 (2021): 88–98.

214. A. P. Isfahani, A. A. Shamsabadi, F. Alimohammadi, and M. Soroush, "Efficient Mercury Removal From Aqueous Solutions Using Carboxylated $Ti_3C_2T_x$ MXene," *Journal of Hazardous Materials* 434 (2022): 128780.